Design of a 300 mK–14 T scanning tunneling microscopy system and characterization of quantum Hall systems with respect to Rashba spin splitting, exchange enhancement and Coulomb gap.

Von der Fakultät für Mathematik, Informatik und Naturwissenschaften der RWTH Aachen University zur Erlangung des akademischen Grades eines Doktors der Naturwissenschaften genehmigte Dissertation

vorgelegt von

Dipl.-Phys. Stefan Becker

aus Bergisch Gladbach

Berichter: Univ.-Prof. Dr. Markus Morgenstern
apl. Prof. Dr. Thomas Schäpers

Tag der mündlichen Prüfung: 22.06.2011

Abstract

This thesis consists of two main parts. The first part describes the design of an ultra-high vacuum system (UHV) for measurements with a scanning tunneling microscope (STM) at a base temperature of about 300 mK and in magnetic fields of up to 14 T. The system consists of two main UHV chambers for sample and STM tip preparations and a large cryostat with an inner single-shot helium-3 cooling stage, holding the home-built STM. Besides commercially obtained ion source, LEED/Auger system, and mass spectrometer, the available instruments for preparation include different sample heaters especially designed for this system. These instruments are shown in detail as well as the STM, which main features are a tip-exchange mechanism and a coarse sample positioning stage. Extensive care has been taken to prevent external vibrations from interfering with the measurements by placing the whole system inside of an anechoic room onto an air damping feet supported stainless steel frame, which resonance modes have been analyzed by finite element simulations beforehand.

The second part of this thesis consists of the preparation and analysis of two-dimensional electron systems (2DESs) by scanning tunneling spectroscopy (STS). These 2DESs are prepared in UHV by cleavage of *p*-type InSb single crystals, producing clean (110) surfaces, and subsequent cesium adsorption onto theses surfaces inside of the pre-cooled STM. This surface doping induces an inversion layer 2DES at the surface that can be probed by STS, because only a coverage of about 1–2 % of a monolayer is necessary.

Using a highly-doped crystal ($N_\mathrm{A} = 1\text{–}2 \times 10^{24}\ \mathrm{m}^{-3}$) the induced band bending confining the 2DES is steep, leading to a strong internal electric field perpendicular to the sample surface. Besides the standing wave patterns of two-dimensional electrons and the quantum Hall transition that have been observed on similar sample systems before, this strong electric field allows an observation of the Rashba effect in the density of states.

The band bending of another 2DES prepared in a low-doped crystal ($N_\mathrm{A} = 1.1 \times 10^{21}\ \mathrm{m}^{-3}$) is more flat and the 2DES does not exhibit the Rashba effect, but in turn it is fully decoupled from the bulk states of the crystal. This requires the electrons in the STS experiment to move through the two-dimensional layer to a side contact, leading to a magnetic field and current dependent spreading resistance due to the localization of the electrons in Landau states. The decoupled 2DES enables the observation of electron–electron interaction effects. As such,

within the quantum Hall regime the 2DES shows a filling factor dependent exchange enhancement of the spin splitting and at the Fermi level a Coulomb gap can be observed within the spatially averaged and the local density of states.

Kurzfassung

Diese Arbeit ist in zwei Hauptteile gegliedert. Der erste Teil beschreibt den Entwurf einer Ultrahochvakuum-Anlage (UHV-Anlage) für Messungen mit einem Rastertunnelmikroskop (RTM) bei einer Basis-Temperatur von 300 mK und in Magnetfeldern von bis zu 14 T. Das UHV-System besteht aus zwei Hauptkammern für Proben- und RTM-Spitzen-Präparation sowie einem Kryostaten mit innerer single-shot Helium-3-Kühlungsstufe für das selbstgebaute RTM. Neben den kommerziell beschafften Komponenten (Ionenquelle, einer LEED/Auger-Einheit und einem Massenspektrometer) enthält die Anlage verschiedene Probenheizungen, die speziell für diese Anlage konzipiert worden sind. Diese Instrumente wie auch das RTM mit Spitzenwechselmechanismum und Probenpositionierung werden im Detail gezeigt. Um zu verhindern, dass externe Vibrationen in das empfindliche RTM einkoppeln und Messungen stören, befindet sich die gesamte UHV-Anlage in einem Schallschutzraum auf einem luftkissengelagerten Edelstahl-Gestell. Die Resonanzfrequenzen des Gestells konnten im Voraus mittels finiten Elementen simuliert und optimiert werden.

Der zweite Teil dieser Arbeit besteht aus der Präparation und Analyse von zweidimensionalen Elektronensystemen (2DESs) mittels Rastertunnelspektroskopie (RTS). Diese 2DESs werden in UHV präpariert, indem durch Spalten eines *p*-dotierten InSb-Einkristalls eine saubere (110) Oberfläche produziert und Cs aufgedampft wird. Die Probe befindet sich während des Aufdampfens bereits im vorgekühlten RTM. Diese Oberflächendotierung induziert ein 2DES in einer Inversionsschicht direkt an der Oberfläche. Ein solches 2DES kann mittels RTS ortsaufgelöst untersucht werden, da lediglich eine Bedeckung von etwa 1–2 % einer Monolage benötigt wird.

Für die erste beschriebene Probe wird ein hochdotierter Kristall verwendet ($N_\mathrm{A} = 1\text{–}2 \times 10^{24}\ \mathrm{m}^{-3}$). Das führt zu einer steilen induzierte Bandverbiegung, die das 2DES begrenzt, und somit zu einem starken inneren elektrischen Feld senkrecht zur Probenoberfläche. An diesem System können stehende zweidimensionale Elektronenwellen und die Perkolation von Drift-Zuständen des Quanten–Hall-Übergangs gezeigt werden, die beide schon an ähnlichen Systemen untersucht worden sind. Das in dieser Probe sehr starke elektrische Feld ermöglicht zusätzlich die Beobachtung des Rashba-Effekts in der zweidimensionalen Zustandsdichte.

Das zweite Probensystem basiert auf einem niedrig dotierten Kristall ($N_A = 1.1 \times 10^{21}$ m^{-3}). Hier ist die Bandverbiegung flacher und der Rashba-Effekt lässt sich nicht nachweisen. Die Elektronen dieses 2DES sind allerdings anders als bei vorherigen Proben vollständig entkoppelt von den dreidimensionalen Ladungsträgern im restlichen Kristall. Das erfordert von den Elektronen im RTS Experiment, dass sie durch die zweidimensionale Schicht zu einer elektrischen Kontaktierung an der Seite fließen. In einem senkrechten Magnetfeld führt das zu einem von Magnetfeldstärke und Strom abhängigen Widerstand durch die Lokalisierung der Elektronen in Landau-Zuständen. Das entkoppelte 2DES ermöglicht ferner die Beobachtung von Elektron–Elektron-Wechselwirkungseffekten. Als solche Effekte kann das füllfaktorabhängige *Exchange Enhancement* der Spinaufspaltung gemessen, sowie ein *Coulomb Gap* am Fermi-Niveau sowohl in der gemittelten als auch in der lokalen Zustandsdichte beobachtet werden.

Contents

1. Introduction

The scanning tunneling microscope (STM) was invented in the early 1980s [1] and scanning tunneling spectroscopy (STS) [2] quickly has become an established research tool. At the heart of all STMs is an electrically contacted sharp tip, that can be scanned in close proximity across sample surfaces with subatomic precision. By measurement of the tunneling current an STM is thus sensitive to electrical properties with a spatial resolution down to the size of a single atom. Reducing the temperature of the STM increases not only the stability of the measurements but it also increases the energy resolution. Thermal broadening can thus be minimized, which allows the study of effects that usually take place at smaller energy scales, e.g. superconductivity gaps, vibrational excitations, Landau levels or spin splittings. By imaging of the local electron density of states (LDOS), the wave patterns of electrons in a two-dimensional electron system (2DES) could be shown directly in real space [3]. Newer studies by STM include superconductivity [4], the Kondo effect [5], or quantum Hall systems [6]. For the latter, a strong external magnetic field is required in order to quantize electrons into Landau states. Using magnetic STM tips even allows measurements sensitive to the electron spins [7].

While the research applications for an STM are manifold, the common ground for all measurements are clean sample systems. These are best prepared and analyzed under ultra-high vacuum (UHV) conditions. Specialized experiments require different preparation instruments and so to keep up with current research topics, an extensible UHV chamber system connected to a cryostat holding and cooling the STM is needed. The first main part shown in this work is therefore the design of a UHV chamber system with an STM operating at 300 mK and in a magnetic field of up to 14 T. At this temperature, the possible energy resolution is below 0.1 meV. After a short introduction into the mathematical interpretation of STM data in Chapter 2, the concept and operation principles of the designed components are shown in Chapter 3.

The second main part of this work (Chapter 4) shows experimental STS results gained on a 2DES prepared near the *p*-doped InSb(110) surface by Cs adsorption. The direct inspiration for these measurements were the results by K. Hashimoto [8], showing the integer quantum Hall transition in real space on *n*-doped InSb(110). This was possible, because the small gap III-V semiconductor InSb has a very low effective electron mass and high electron g-factor so that the

Landau level and spin splitting is exceptionally high. By using a *p*-doped crystal the 2DES is not formed in an accumulation layer connected to the bulk at the Fermi level of the semiconductor, but in an inversion layer separated from the bulk by the band gap [9]. Therefore, the 2DES gets a distinct Fermi level, which is an important requirement for the observation of electron–electron interaction effects.

Different acceptor concentrations of *p*-InSb are used to tune the steepness of the confinement potential. A high concentration leads to a high internal electric field of the 2DES, exhibiting the Rashba effect [10, 11] in the density of states. The Rashba effect describes a spin splitting due to spin-orbit interaction. It may become a central handle in spintronics as it provides the opportunity to manipulate electron spins by electric fields. By STS it has so far only been detected on metal surfaces [12, 13], where it has also been probed by angular resolved photoelectron spectroscopy [14, 15, 16, 17]. In III-V semiconductors, which are much more suitable for electronic applications, it has been previously probed by the beating pattern of Shubnikov–de Haas oscillations [18, 19, 20] or by the analysis of weak antilocalization [21, 22].

A low acceptor concentration in an InSb sample leads to a flat band bending, which increases the separation of the 2DES from the bulk. In this system the bulk electrons are sufficiently far away to fully decouple from the 2DES and to not screen electron–electron interaction effects. The exchange enhancement of the electron g-factor [23, 24, 25, 26] and the Coulomb gap [27, 28] at the Fermi level has been measured as the first two electron–electron interaction effects.

2. Scanning Tunneling Microscopy

The basic operational principle of a scanning tunneling microscope (STM) as developed by Binning and Rohrer [1], Nobel Prize in 1986, is electron tunneling between a metallic tip and a conducting surface in close proximity to each other. Scanning the tip across the surface with precision in the pm range allows measurements of topographical and electrical properties with a spatial resolution below atomic length scales. This chapter only briefly discusses the basic physical principles of electron tunneling within these boundary conditions. These principles are common knowledge in STM research and already well discussed in textbooks (e.g. [2]) and previous PhD theses (e.g. [29, 30, 31]).

2.1. Tersoff-Hamann model

One-dimensional electron tunneling through a rectangular potential barrier is a standard textbook problem in quantum mechanics. An incident wave with wave vector k is partly reflected and partly transmitted through a barrier of height V_0. For electrons with an energy E and a highly attenuating barrier ($V_0 \gg E$) the ratio of transmitted and incident current densities is given by the transmission coefficient [2]

$$T \approx \frac{16k^2\kappa^2}{(k^2+\kappa^2)^2} \exp(-2\kappa z) \tag{2.1}$$

with decay rate $\kappa = \sqrt{2m^*(V_0 - E)}/\hbar$, effective electron mass m^* and barrier width z. $V_0 - E = \phi$ is the effective barrier height, which is of the order of a few electron volts in typical STM experiments. T depends exponentially on the barrier width, which already indicates the high spatial resolution of an atomically sharp STM tip in vertical direction.

A three dimensional and first quantitative description of the tunneling process in an STM experiment has been given by Tersoff and Hamann [32, 33]. They applied the mathematical solution of the time dependent Schrödinger equation for elastic tunneling between two metallic layers by Bardeen [34] to the model of a spherically shaped tip (s-shaped tip wave function) over a flat surface (see Figure 2.1). The tunneling current I is calculated by evaluating the tunneling

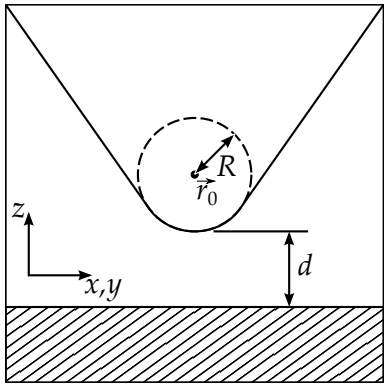

Figure 2.1.: Sketch illustrating the Tersoff-Hamann model of a spherical STM tip at a position $\vec{r}_0$ with radius R in distance d to a flat surface (after [32])

matrix elements for tip and surface wavefunctions. In the temperature limit $T \rightarrow 0$ K and for small applied voltages V with respect to ϕ, the following relation for I within this model can be derived [2]:

$$I(V, \vec{r}_0) \propto \int_0^{eV} \rho_\mathrm{t}(eV - E)\rho_\mathrm{s}(E, \vec{r}_0)dE \tag{2.2}$$

with the density of states of the tip $\rho_\mathrm{t}(E)$ and the density of states of the surface $\rho_\mathrm{s}(E, \vec{r}_0)$ at the position of the tip $\vec{r}_0$. The energy E is measured with respect to the corresponding Fermi level E_F.

In scanning tunneling spectroscopy (STS), one is usually interested in the density of states of the surface at the surface $\rho_\mathrm{s}(E, x, y)$, so Equation (2.2) can be written as

$$I(V, x, y, z) \propto \int_0^{eV} \rho_\mathrm{t}(eV - E)\rho_\mathrm{s}(E, x, y)T(E, eV, z)dE \tag{2.3}$$

with a transmission coefficient $T(E, eV, z)$. With the WKB[1] method the transmission coefficient can be estimated in first order to [2]

$$T(E, eV, z) = \exp\left\{-2z\left[\frac{2m^*}{\hbar^2}\left(\frac{\phi_\mathrm{t} + \phi_\mathrm{s}}{2} + \frac{eV}{2} - E\right)\right]^{1/2}\right\} \tag{2.4}$$

with the tip surface distance $z = d + R$ and tip (sample surface) work functions

[1] Wentzel-Kramers-Brillouin

ϕ_t (ϕ_s). The derivative of Equation (2.3) can be expressed as

$$\begin{aligned}\frac{dI}{dV}(V,x,y,z) \propto e\,\rho_t(0)\,\rho_s(eV,x,y)\,T(E=eV,eV,z) \\ + \int_0^{eV} \rho_t(eV-E)\,\rho_s(E,x,y)\,\frac{dT(E,eV,z)}{dV}\,dE \\ + \int_0^{eV} \frac{d\rho_t(eV-E)}{dV}\,\rho_s(E,x,y)\,T(E,eV,z)\,dE.\end{aligned} \tag{2.5}$$

Assuming only small variations of tunneling coefficient $T(E,eV,z)$ and tip density of states $\rho_t(E)$ this gives the desired relation of the differential conductivity dI/dV to the local density of states of the surface LDOS(x,y). The validity of theses assumptions have to be checked in the experiment. For $|V| < 200$ meV the error by neglecting the two last terms of Equation (2.5) at constant z can be estimated quantitatively to be below 10 % [35]. In the measurements presented in this work there has been no necessity to correct for the z dependence of the tunneling coefficient in the first term. Estimates for STM tips other than spherical (s-orbital) as in the Tersoff-Hamann model predict different observed atomic corrugations (e.g. [36]), which can be neglected for the larger length scales of the electron patterns evaluated in this work (a few nm). Moreover, it is shown that higher orbital tip states with orbital quantum number l lead to an l-fold derivative of the right-hand side of Equation (2.5), which for dominating z-type orbitals still maintains [37, 38]

$$\frac{dI}{dV}(V,x,y) \approx \rho_s(eV,x,y). \tag{2.6}$$

2.2. Energy resolution

As described above, the differential conductivity dI/dV can be regarded as being proportional to the local density of states (LDOS) of the sample surface at the applied voltage V. These dI/dV values may be measured by ramping V and differentiating the current $I(V)$, but using the lock-in technique gives usually a much better signal to noise ratio. In this case, the applied voltage V is modulated by a sinusoidal wave at a frequency of the order of 1 kHz with a modulation voltage V_{mod}. The output amplitude of the lock-in amplifier is proportional to dI/dV. The energy resolution ΔE, defined as the minimum distance of two δ-peaks causing two distinct maxima in dI/dV, is given due to V_{mod} measured in root mean square (RMS) values of Volts V_{rms} by [29]

$$\Delta E_{mod} = 2.5 \times eV_{mod}. \tag{2.7}$$

The limit of the energy resolution due to the finite temperature T is one of the main reasons of going to low temperatures in STS experiments. The temperature dependent ΔE in an STS measurement can be estimated to [31]

$$\Delta E_{\mathrm{T}} = 3 \times k_{\mathrm{B}} T \tag{2.8}$$

with Boltzmann constant k_{B}. At $T = 5$ K this limits the energy resolution to 1.3 meV while at 300 mK the limit is below 0.1 meV. The combined energy resolution is approximately given by

$$\Delta E \approx \sqrt{(2.5 \times eV_{\mathrm{mod}})^2 + (3 \times k_{\mathrm{B}} T)^2}. \tag{2.9}$$

At 5 Kelvin the modulation voltage can be as high as $V_{\mathrm{mod}} = 0.5$ $\mathrm{mV_{rms}}$ and ΔE is still below 2 meV. To take advantage of the increased energy resolution at 300 mK on the other hand, V_{mod} needs to be reduced accordingly. At such low voltages and low tunneling currents electrical noise due to voltage and current amplifiers as well as due to an oscillating tip–surface distance are often dominant, leading to long integration times. The expermental requirements usually decide wether to increase V_{mod} and worsen the energy resolution or increase the averaging lock-in integration time constant t_{c}, which may increase the total measurement time significantly.

2.3. STM and STS experiments

Topography STM images in this work were done using the *constant current mode*: At constant voltage the STM tip scans an image area in the (x, y) plane while adjusting the tip surface distance z in order to keep the current constant. According to Equations (2.3) and (2.4) at constant voltage, the z dependence of the current is given by

$$I(z) \propto \exp(-2\kappa z) \tag{2.10}$$

with a corresponding constant κ. The topography image is then given by a grayscale or false color plot of $z(x, y)$, which is usually corrected by a plane fit due to minimal misalignment of the sample surface and the scanned (x, y) plane.

In this work dI/dV data has been measured to gain dI/dV maps (spatially resolved images of the LDOS), dI/dV curves (LDOS curves) and DOS curves. A single dI/dV curve is gained by stabilizing the STM tip position at tunneling distance, usually by a defined stabilizing voltage V_{stab} and current I_{stab}. Then, the voltage V is ramped while the output of the lock-in amplifier is collected. This output can be interpreted as being proportional to the LDOS of the sample. The macroscopic density of states (DOS) of the surface can be measured

by statistically averaging many LDOS curves scattered over an area larger than the length scales of the local variations. For the samples prepared in this work, these are the length scales of the potential fluctuations (about 50 nm).

A single dI/dV image can be prepared by simply recording the lock-in output while taking a topography image as described above. This is the fastest method for a spatial image of the local density of states, but it can obviously not be used to take images at the Fermi level ($V = 0$). Stable imaging is also not easy near the band gap region of semiconductor samples, where the local density of states and therefore the tunneling current is too low. Therefore in this work dI/dV images were recorded as dI/dV maps, where the tip is stabilized at each grid point of a topography image taken at a stabilizing voltage V_{stab} and a dI/dV curve is measured.

In order to prevent artificial smoothing of the dI/dV curves the ramping of V either has to be done slowly enough or in steps with a delay time depending on the time constant t_c and filter settings of the lock-in amplifier. To converge at 99 % of its final value the lock-in used here[2] requires a delay time of up to $10 \times t_c$ at the highest filter settings, which gives the best signal to noise ratio. A single curve at high energy resolution can easily take up several seconds, a dI/dV map at high energy and spatial resolution hours or even days. This exemplifies the necessity of a stable low temperature STM system with a high continous operation time for such measurements.

[2]Lock-in model: Stanford Research Systems SR830

3. Design of a UHV system for STM experiments at 300 mK and 14 T

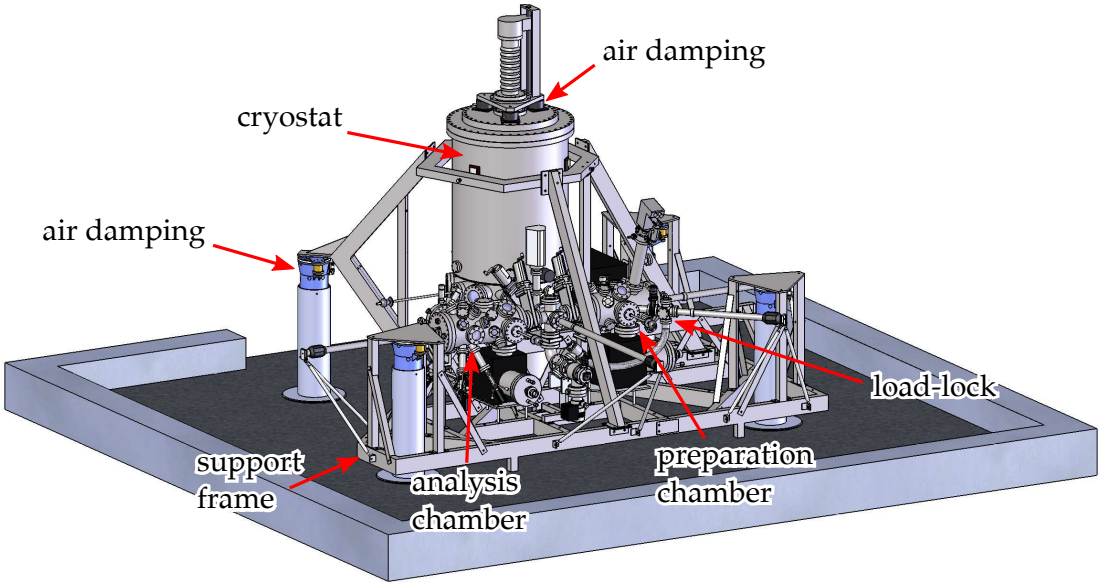

Figure 3.1.: 3D CAD view of the complete low-temperature UHV-STM chamber system as designed, mounted onto its support frame. The frame is supported by air damping feet placed on the floor of the anechoic room, which boundarys are shown.

3.1. Introduction

A scanning tunneling microscope (STM) can probe the local conductance of samples with a sub-nanometer spatial resolution. In scanning tunneling spectroscopy (STS) measurements, one gains access to the local density of states (LDOS) at a given bias voltage between tip and sample as described in Chapter 2. With this technique it is possible to create maps of electron distributions at

sample surfaces in real space. Local variations may be caused by potential disorder, atomic structures at the surface or even the atomic orbitals themselves. While the actual spatial resolution depends mostly on the stability of the STM and its mouting, the energy resolution in spectroscopy measurements is also limited by the finite temperature T of sample and tip. According to Equation (2.8) this limit is roughly 80 meV at room temperature (300 K). To increase the energy resolution, the STM needs to be cooled down. A standard helium-4 bath cryostat at a base temperature of 4.2 K gives a temperature limit for the energy resolution of about 1 meV. The system described in this work aims at a base temperature of 300 mK, giving an energy resolution below 0.1 meV. Combined with a 14 T solenoid magnet the system enables a variety of experiments only observable at high fields and low temperature like the quantum Hall effect (QHE) or electron–electron interaction effects. To perform such experiments, samples and STM tips need to be prepared in ultra-high vacuum (UHV) at pressures $p \lesssim 10^{-8}$ Pa. Therefore a UHV chamber system connected to the cryostat is designed that holds standard surface science preparation methods and is extensible for future experiments. After a short overview of existing STM systems with comparable specifications, the design concept will be discussed. The external requirements of the system will be outlined and the implementation presented. Selected components designed especially for this system will be shown in more detail.

3.2. Existing comparable STM systems

In the past few years, numerous low temperature STM systems have emerged. Comparable systems, offering the UHV sample and tip preparation methods in conjunction with stable measurements below 1 K and at high magnetic fields as the system designed in this work are still rare. All these instruments are individual designs and therefore have different specifications. Among the first was the STM system by Kugler *et. al* in Switzerland [39], operating with sorption pumped helium-3 at $T = 275$ mK with a magnetic field of up to $B = 14$ T. These types of cryostats usually operate in a single shot mode, which means that the helium-3 reservoir is cooled by the sorption pump. When the reservoir is depleted, it has to be refilled again by a regeneration process of the sorption pump, involving an increased temperature of the helium-3 reservoir. As this is the type of operation chosen for the cryostat of the system presented here, the operation principle is discussed in more detail in Section 3.7. The advantage of these cryostats are that they reach a low base temperature without any continous gas flow through capillars and expansion tubes near the STM, which may cause intrinsic vibrational noise in the experiment. The obvious dis-

advantage is the limited holding time at the base temperature, which can be an important factor for some STS experiments, so the helium-3 quantity has to be sufficient for the intended experiments. The holding time of the system in Reference [39] is about 40 hours. Other designs with similar cryostats are located in Ibaraki, Japan [40] (350 mK/11 T/8 hours) and Hamburg, Germany [41] (315 mK/14 T/30 hours). The cryostat described in this work is designed to achieve a holding time of 100 hours.

An alternative method of cooling below 1 K utilizes the Joule–Thomson effect, where a helium gas flow is achieved through an external pumping mechanism and adiabatic expansion reduces the temperature. Although the gas flow may be a source of vibrations, such cryostats have been built for STM applications showing very low noise. The reachable base temperature of these systems is generally higher than that of the sorption pumped crystats. Using helium-3, $T = 0.5$ K can be achieved in a system with a single shot mode of the adiabatic expansion [42]. Recently, a Joule–Thomson cryostat with continous operation has become available commercially.[1] This cryostat design has shown a continous operation at 0.9 K with stable STM measurements using helium-4 only [43], which is a major advantage for this temperature scale as helium-3 has become very expensive and hard to come by. Using this design with helium-3 in a closed cycle should allow temperatures of about 0.5 K as well.

Systems utilizing a dilution refrigerator cryostat reach even lower temperatures as the one in Tokyo, Japan [44], operating at $T = 30$ mK, $B = 6$ T, with a holding time of nearly 72 hours. The dilution process involves a successive mixing and separation of helium-3 and helium-4, starting from a temperature of about 1 K by externally pumped helium-4 or by a Joule–Thomson process. Naturally, these cryostats require even more efforts for a vibrational insulation. Probably the low temperature STM with the most extreme specifications to date is located at NIST[2] with a continous operation duration of 11 days at $T = 10$ mK and $B = 15$ T [45]. This STM is actually integrated into a UHV chamber system far exceeding the dimensions of the instrument designed here.

3.3. Design of the ultra-high vacuum system

The requirements for a low-temperature UHV-STM system with high magnetic field to reach low noise measurements are manifold: The STM itself (Section 3.8) has to be rigid, thermally conducting, non-magnetic, UHV compatible, and mounted inside the cryostat isolated from external or possible internal vibra-

[1] SPECS Surface Nano Analysis GmbH, Berlin, Germany
[2] Center for Nanoscale Science and Technology, Gaithersburg, Maryland, USA

tions. For experiments demanding sample and tip exchange mechanisms the STM has to be accessible by external manipulators inside the UHV. For sample and tip preparations, separate chambers are needed with different instruments like sample heaters, ion source, electron beam evaporators, or a LEED/Auger system.

Requirements for ultra-high vacuum at pressures $p \lesssim 10^{-8}$ Pa are not only the appropriate pumps like turbomolecular, ion getter, titanium sublimation or cold shield *cryo*-pumps. All materials inside the vacuum chambers have to have accordingly low vapor pressures and be stable up to temperatures of about 100–150 °C for a *bake-out* procedure, mainly needed to pump adsorbed water from the surfaces. These restrictions allow most commonly used metals and alloys such as stainless steel, from which the chamber walls and flanges are produced, and several ceramics like aluminum oxide, needed for insulations. Most polymers are not UHV compatible so the flange seals are made from metal, usually copper because it is relatively soft. This also limits the mechanical access into the vacuum system to devices with flexible welded bellows or magnetic force transmission. Such devices are usually commercially available and are integrated into the system.

A 3D view of the complete system is shown in Figure 3.1, a top view illustrating the outer dimensions is given in Figure 3.2. Like the design of similar STM systems, the UHV system including the cryostat is mounted on a rigid frame supported by air damping feet to isolate it from external vibrations above 1–2 Hz (Section 3.9). To avoid accoustic noise the whole experimental setup is placed inside an anechoic room. A notable difference from other systems is the cryostat itself, which was designed in cooperartion with CryoVac GmbH & Co. KG (Section 3.7). Connected to one side of the cryostat is the remaining UHV chamber system including the preparation chamber with a load lock (Section 3.4) and the analysis chamber (Section 3.5). The cryostat and both additional chambers are connected by a transfer cross with vacuum valves. A turbomolecular pump is also connected to the transfer cross. This setup allows an independent use or bake-out of any one or two chambers.

3.4. Preparation chamber with load lock

The preparation chamber with the load lock is shown in Figure 3.3. To be able to use new STM tips or samples in the STM they first have be introduced into the vacuum system via the load lock. This small chamber can be isolated by a vacuum valve from the remaining system and has a bypass to the turbomolecular pump, so that only this small section has to be baked out. The remaining preparation chamber is intended to cover preparation methods that tend to op-

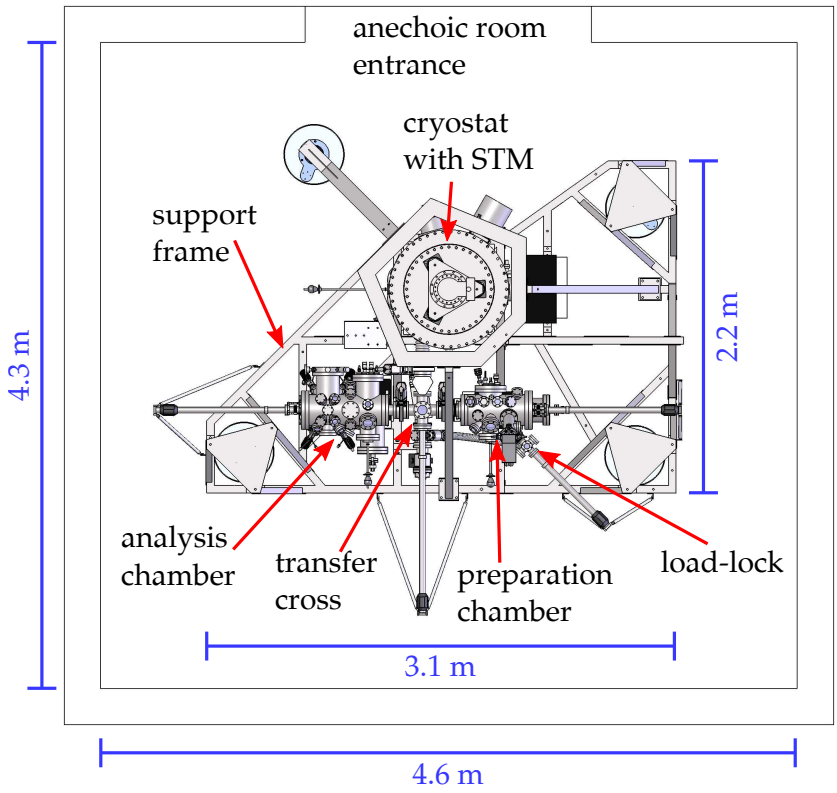

Figure 3.2.: CAD construction drawing: top view of the UHV system with support frame inside of the anechoic room.

erate at lower vacuum quality like an electron beam heater (Section 3.4.1) or an ion source, which are both needed to clean sample surfaces like gold or tungsten single crystals. In its current setup it also features a plasma source[3] that can, unlike the small standard ion source, accelerate atoms and ions onto samples with energies as low as 25 eV. The wobble stick manipulator[4] can move STM tips and samples between the transfer rods of the load lock and the chamber and it can place them into the electron beam heater or the resistive heater (Section 3.4.2) below the ion source.

3.4.1. Electron beam heater

The electron beam heater shown in Figure 3.4 is attached to a flange on the back side of the preparation chamber. It works by heating a filament in proximity

[3]Gen2 Plasma Source, tectra GmbH
[4]Dual Shaft Wobblestick, Ferrovac GmbH

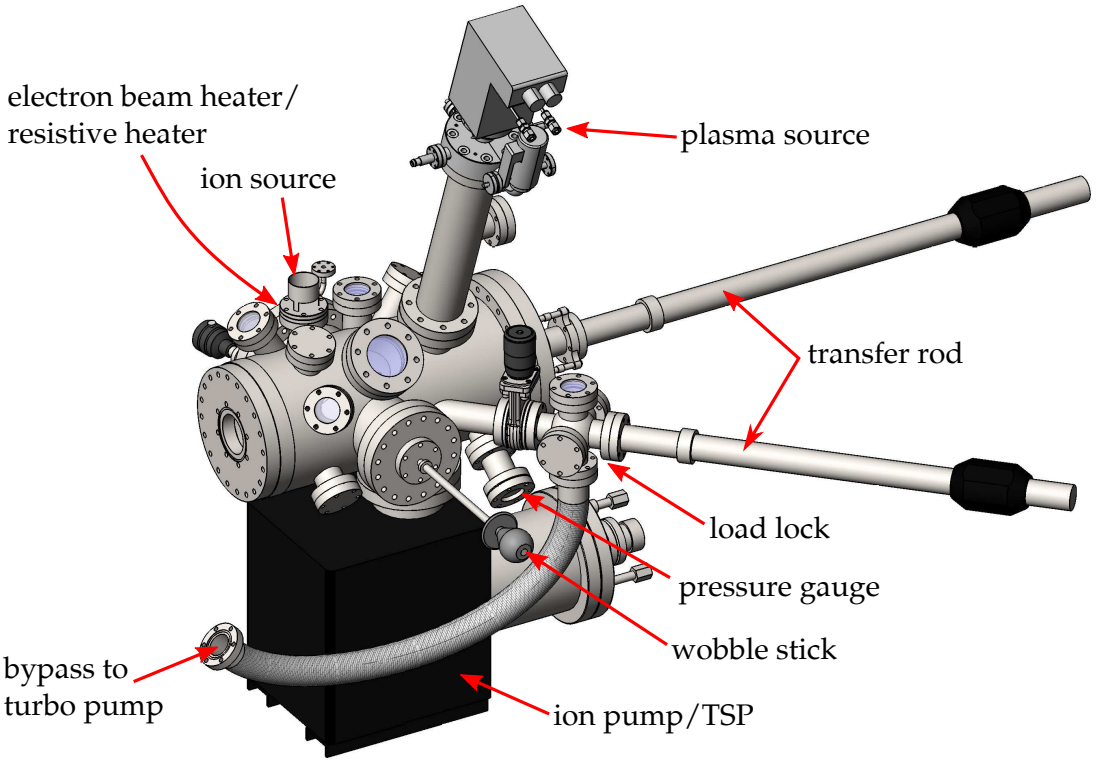

Figure 3.3.: 3D CAD view of the preparation chamber and the load lock.

to a sample holder or a tip shuttle. The sample (tip) is held at high positive voltage $\approx$ 1–2 kV and the electrons emitted from the filament directly heat the sample (tip). This type of heater can heat samples (tips) up to 2500 °C if needed, like for the cleaning process of tungsten single crystals. The main difficulty in the design of such a heater is thermal insulation, because every part getting hot degasses and increases the pressure, interfering with the cleaning process. In this design the sample receiver is made from tungsten sheets, point welded with thin tantalum sheets onto long tungsten rods. Tungsten and tantalum both have very high melting points (above 3000 °C) and low vapor pressures. On the back side the tungsten rods are fixed at a molybdenum block by molybdenum screws. The vapor pressure of molybdenum is not as low at high temperatures as that of tungsten but it is much better machinable. The molybdenum block is held in place and insulated electrically by aluminum oxide eyelets. This cascade of material transitions and especially the long tungsten rods are responsible for the thermal insulation. The filament used is a standard, cut open halogen lamp[5] that can be replaced easily. As temperature control a type C thermocouple is

[5] 12 Volts, 100 Watt, G6.35 BiPin Base

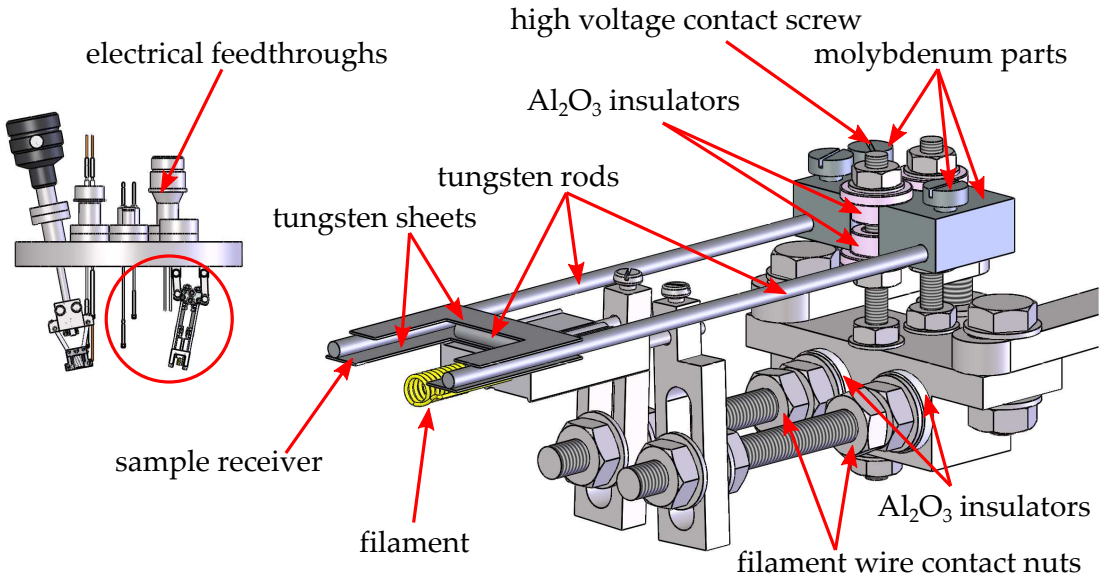

Figure 3.4.: Left: top view of the flange assembly for the sample heaters. Right: Enlarged 3D model view of the electron beam heater.

point welded at the sample receiver and an external pyrometer has direct visual access through a viewport above the heater.

3.4.2. Resistive heater

The purpose of the ion source in the preparation chamber is bombardment of sample surfaces with ions like Ar^+ for rough sample cleaning or other preparation methods. Some preparation methods require the samples to be under defined angles relative to the ion source or to be heated at moderate temperatures, like *grazing incidence ion erosion* [46, 47]. For that reason the sample receiver under the ion source was designed as a resistive heater mounted onto a rotary drive, shown in Figure 3.5. The heater body is made from molybdenum, as it has a high melting point, low vapor pressure and can be machined easily. The heating is done by tungsten wire in aluminum oxide double bore tubes, heating the whole molybdenum body. Thermal and electrical insulation is achieved by two aluminum oxide tubes that fit into the heater body under an arbitrary angle. This way they hold the body in place and are free of stress. To decouple the wiring mechanically from the rotary motion they can be attached to Macor insulated screws positioned under the heater back support. A type K thermocouple is fixed at the heater body for thermal control. The same wiring can be used for measuring the ion current. The manual rotary drive allows a

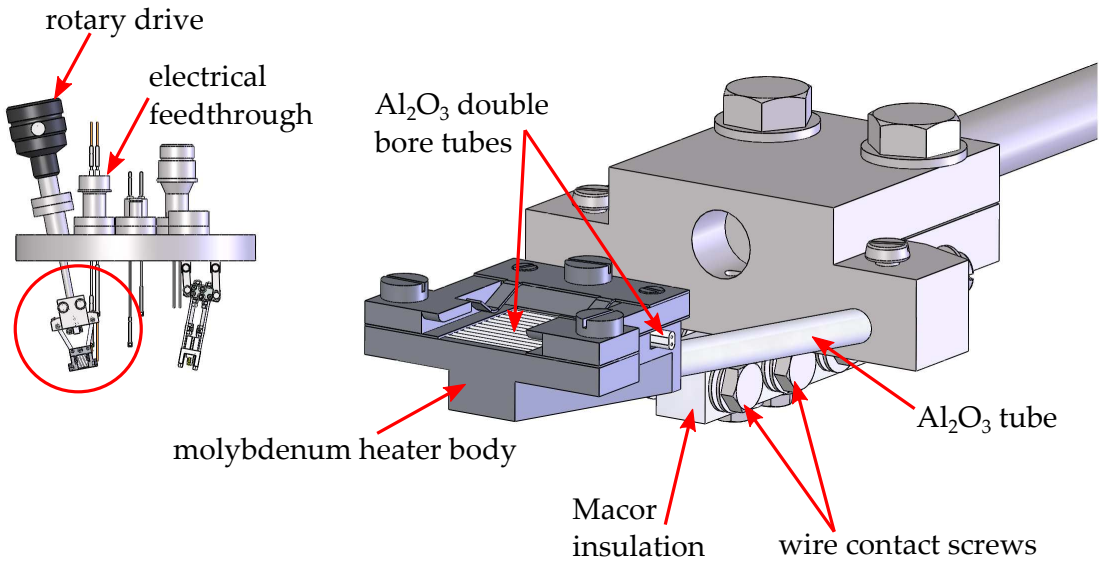

Figure 3.5.: Left: top view of the flange assembly for the sample heaters. Right: 3D model view of the resistive heater under the ion source.

precise external control of the angular motion of the heater. This heater is intended for the temperatures up to about 600 °C and has in this range a much better temperature control than the electron beam heater.

3.5. Analysis chamber

The analysis chamber holds those preparation methods that tend to require better vacuum conditions and do not regulary operate at lower pressures unlike the ion source with gas inlet in the preparation chamber for example. These methods include evaporators as sources for specific materials and a LEED/Auger system, which is a standard instrument in surface science to analyze the crystal structure and material composition of sample surfaces. Because some sample preparation procedures require moderate heating of samples during the evaporation process or LEED/Auger measurement, a rotatable resistive sample heater stage was designed for the focus point of these instruments (Section 3.5.1). Furthermore the analysis chamber was designed to be extendable by adding several free flanges for future instrument installations. In its current setup the flange facing the wobble stick manipulator holds a sample storage shelf and a home-built combined scanning tunneling and tuning fork atomic force microscope (RT-STM/AFM [48]), installed here for testing purposes. This microscope is also designed to be compatible with the cryostat to operate at

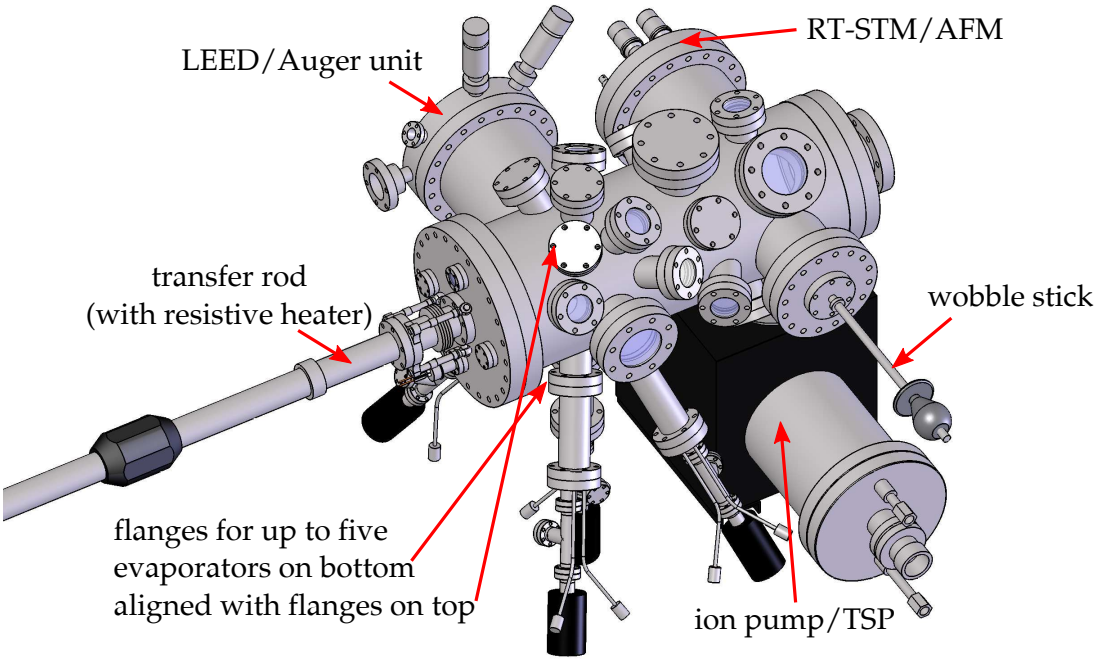

Figure 3.6.: 3D CAD view of the analysis chamber.

300 mK and 14 T as the STM described in Section 3.8. An additional microscope operating at room temperature has also the advantage of testing newly prepared samples quickly prior to insertion into the low temperature STM, because it can start imaging immediately while in the cryostat samples usually take up to several hours until they are thermally stable.

3.5.1. Resistive heater

The resistive heater in the analysis chamber shown in Figure 3.7 has to be rotatable to allow samples to face the LEED/Auger system and evaporators separately. The concept of sliding contacts has been adapted from previous designs [49], the remaining assembly has been redesigned to optimize the vapor pressure at elevated temperatures by using long aluminum oxide tubes as thermal insulation, similar to the resistive heater in the preparation chamber (Section 3.4). Here the aluminum oxide tubes are spring loaded with a molybdenum flat spring to prevent too much strain on the ceramics. The resistive heating itself is done again via tungsten wire in aluminum oxide double bore tubes, but here three layers of tubes are stacked on top of each other instead of one. This allows higher sample temperatures without a melting of the tungsten wires than just one layer, because the currents through each wire can be lower at the same

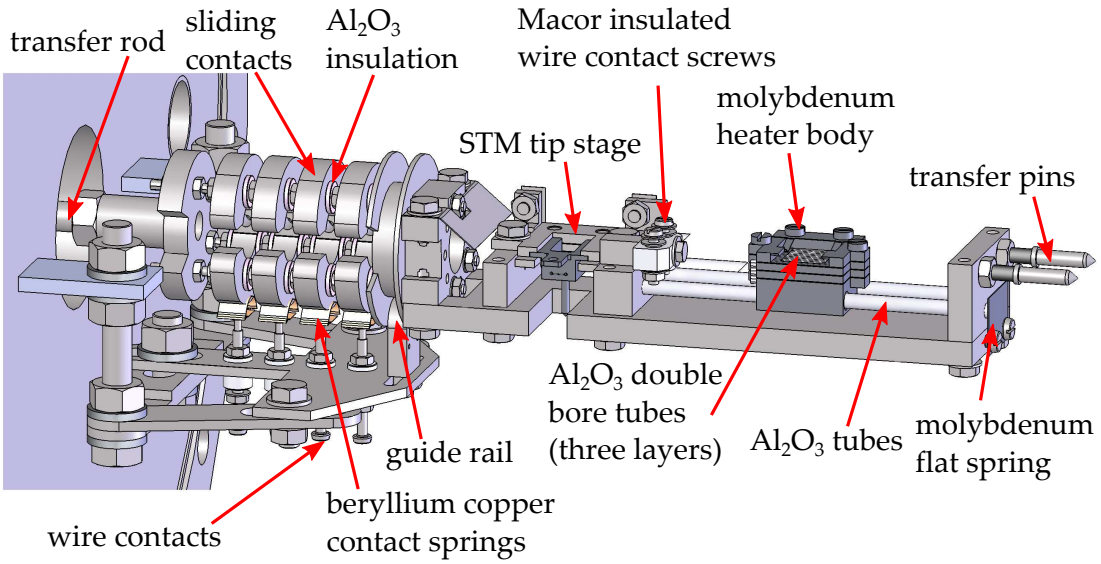

Figure 3.7.: 3D model view of the resistive heater in the analysis chamber. The contact springs are fixed onto the side flange of the chamber. The heater assembly itself is mounted onto the rotatable transfer rod.

heating power.

To allow STM tips to be coated they need an additional receiving stage because the tip shuttle exposes the tip on the opposite side of where the sample holders hold the samples (compare Figure 3.14). The transfer pins on the right end of the assembly fit into the transfer block used for the sample transfer between chambers as described in Section 3.6. The sliding contacts, originally made from copper, have been replaced by stainless steel, because the friction with the beryllium copper contact springs was too great. Power losses by using stainless steel are neglegible due to the thickness of the contacts. Care had to be taken that the wires can not be short-circuited by metals from the evaporator sources. This would especially lead to wrong values for the temperature control as the thermoelectric voltage of the type K thermocouples would drop. The prototype of this design has been used successfully in another UHV chamber system to heat up samples up to 1000 °C.

3.6. Transfer cross

The transfer cross shown in Figure 3.8 is positioned between the cryostat, the preparation chamber and the analysis chamber (not shown in this figure). It is also connected to the load lock and the turbomolecular pump, used for baking

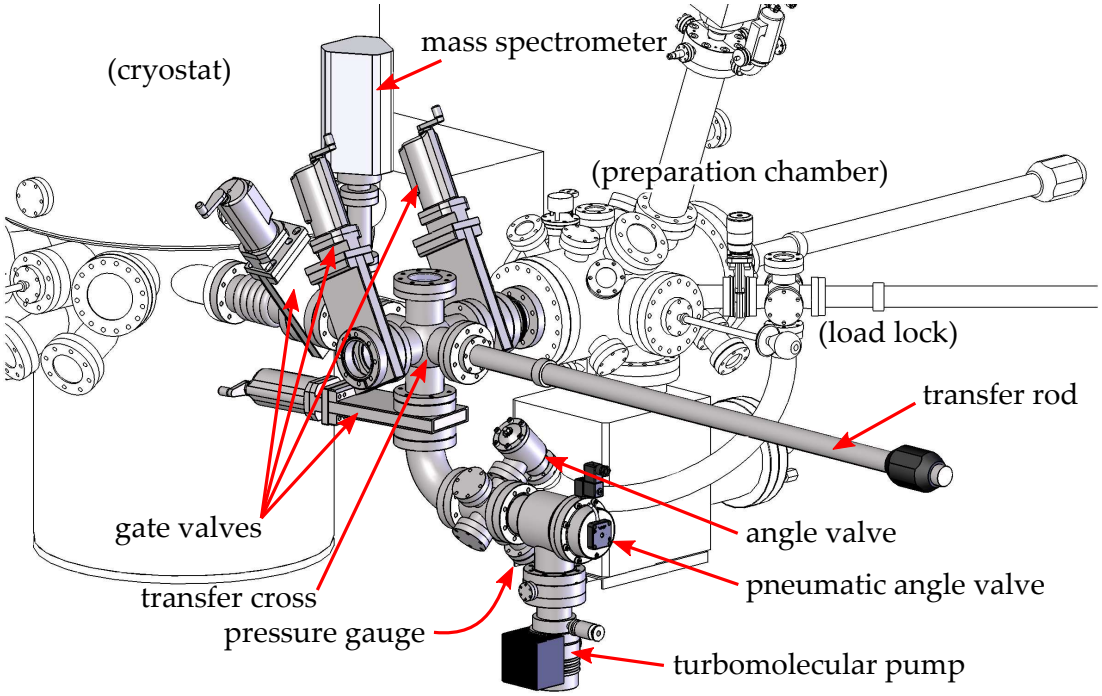

Figure 3.8.: 3D CAD view of the transfer cross. The connected cryostat, preparation chamber and load lock are outlined.

out and during preparation processes involving degassing or the gas inlet. It holds a mass spectrometer that is of use in all chambers before and after bake-out for leak testing and residual gas analysis, as well as for gas analysis during certain preparation methods. The UHV valves allow an independent use, venting and bake-out of any chamber.

In the transfer cross the samples are transferred between the transfer rods by sliding pins and a block with a rotatable sample receiver shown in Figure 3.9. The design for the transfer mechanism is adapted from the system described in Reference [41], where it works reliably for a transfer between two rods. To align all three transfer rods in this system they can be tilted by flexible bellows.

3.7. Cryostat

The cryostat intended for this UHV system was designed in cooperation with CryoVac GmbH & Co. KG as a second prototype of a sorption pumped helium-3 cryostat with solenoid magnet for STM research. Sadly the cryostat has not been finished by the time of this writing due to several delays and setbacks in the design and testings of the first prototype delivered to the University of

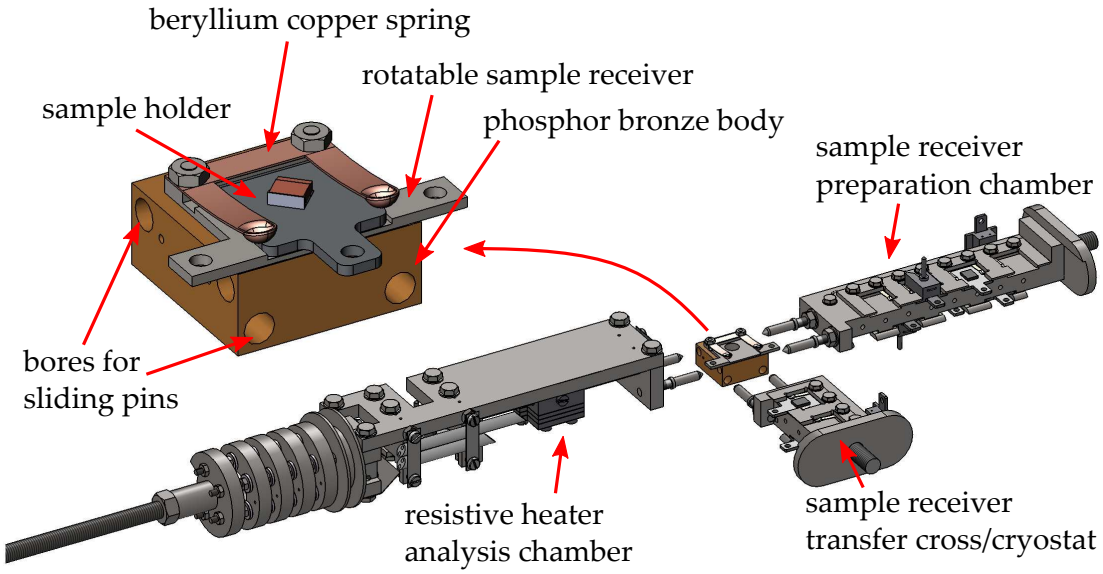

Figure 3.9.: 3D illustration of the sample transfer in the transfer cross. Each transfer rod has two stainless steel pins, sliding into the bores of the transfer block's bronze body.

Hamburg in 2010. The cryostat is finished in design and manufactured except for the last but essential helium-3 cooling stage. Nevertheless we are confident based on the data from the first prototype and from test measurements of the other cooling stages of the cryostat that the final instrument will achieve the required specifications including holding time and stability. In the following the design concept and functionality will be outlined. A detailed description with test measurements will be given in a future PhD thesis and publication.

The outer dimensions and access flanges of the cryostat are shown in Figure 3.10. In this design the whole cryostat is a large UHV chamber with its own turbomolecular, ion getter and titanium sublimation pump. These pumps are needed during the bake-out to get a good base pressure prior to the initial cooling. If cooled with liquid nitrogen and helium the large inner tanks and shields act as cryopumps in such cryostats, typically with a pressure at the microscope's location of below 10^{-10} Pa. This allows probing of sensitive surfaces for weeks without contamination. The baking process and low base pressure is needed nevertheless in order to introduce clean new samples, as this usually requires moving parts and a local warming up by thermal radiation. The pressure increase due to desorption can be reduced significantly if these parts are baked-out.

The basic working principle of this cryostat to reach its final temperature is the pumping of liquid helium-3 by a charcoal sorption pump. A sorption pump

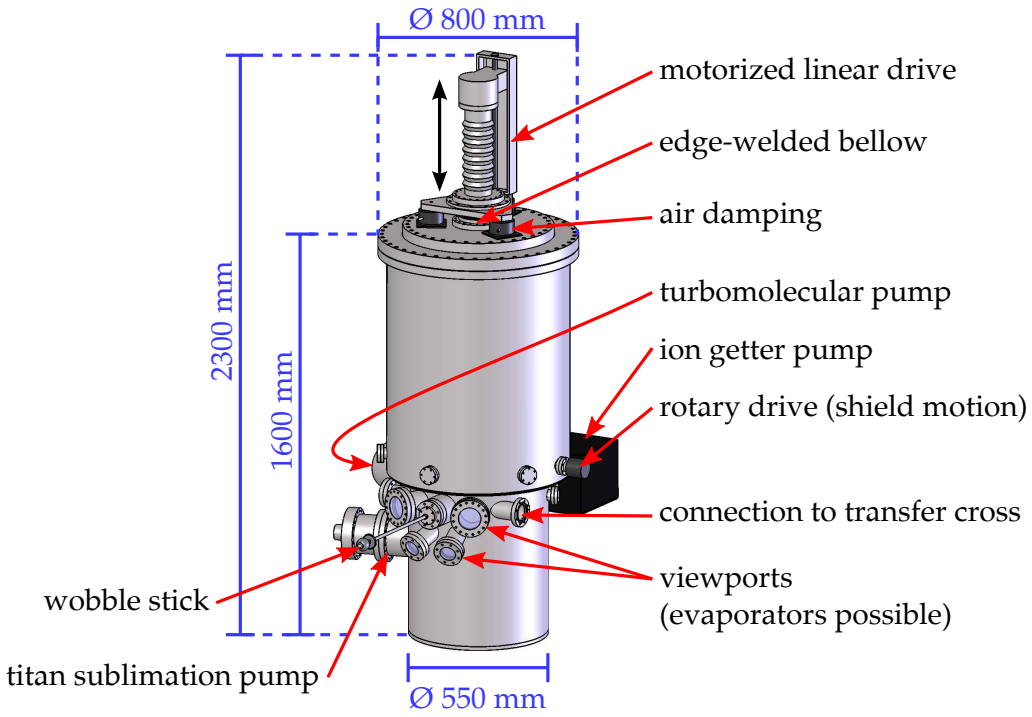

Figure 3.10.: 3D CAD drawing of outer view of the cryostat.

is basically just a porous material with a large inner surface, adsorbing and trapping atoms like a sponge when cooled by liquid helium-4. As helium-3 is very rare and expensive, this process can be reversed by heating the sorption pump and condensing the helium-3 in a vessel, the helium-3 pot, which is cooled by pumped helium-4 to nearly 1 K. The pumping of helium-4 can be done by a large rotary vane or scroll pump on the outside of the system because it is available in larger quantities. If the helium-3 is liquified and precooled by this process, the *condensing stage*, pumping of helium-3 can reach base temperatures of about 250 mK, depending on the heat introduction from the outside.

To shield the helium-3 stage from heat, the cryostat is build in layers as depicted in Figure 3.11(a). It holds an outer liquid nitrogen tank and shield at 77 K and an inner liquid helium-4 tank at 4.2 K. The 14 T superconducting solenoid magnet in the lower part needs also to be bathed in liquid helium-4 to operate. The so-called 1 K pot is filled with helium-4 as well, but it is pumped by an external scroll pump as described above. The central helium-3 unit, consisting of the helium-3 pot with connected STM and the sorption pump, is only attached mechanically at the very top to the motorized linear drive. The linear drive itself is decoupled mechanically from the remaining system by an edge-welded bellow and three air damping feet. This air damping intends to minimize an

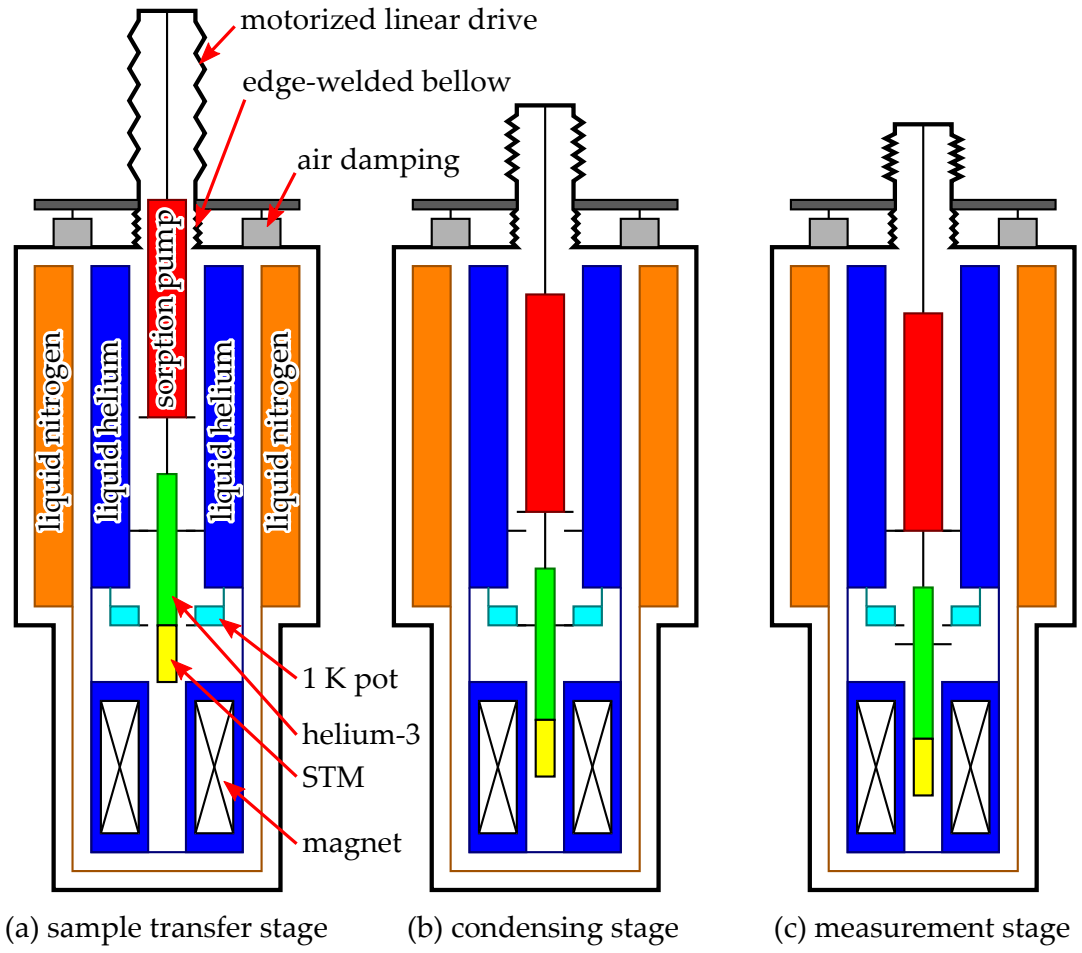

Figure 3.11.: Sketch of the cryostat operation stages.

interference of external vibrations with the measurement.

Figure 3.11(a-c) illustrate the stages of operation of the cryostat. During the sample transfer stage (a), the STM is in the sample transfer plane, where it can be accessed externally by a wobble stick. The viewports of Figure 3.10 oriented towards the STM at this position may also be replaced by an evaporator source to evaporate materials directly into the STM at the cold sample surface. This procedure is needed for experiments like Cs on InSb as described in Chapter 4. During this stage the helium-3 pot is thermally connected to the helium-4 for precooling. This connection can be lifted externally and the motorized linear drive can lower the helium-3 unit to the other stages.

During the condensing stage (b) the helium-3 pot is thermally connected to the pumped 1 K pot and the sorption pump is thermally isolated. An internal heating wire of the sorption pump heats it up to about 20–40 K for regenera-

tion, while the helium-3 is condensed in the helium-3 pot. Once all helium-3 is condensed, which can be measured by a pressure drop in the helium-3 system, the motorized linear drive can lower the helium-3 unit further into the lowest position.

At this measurement stage (c) the sorption pump is in thermal but not mechanical contact with the helium-4 tank by fine copper threads. The helium-3 is pumped and the STM reaches its base temperture. In this position, the sample in the STM is in the very center of the solenoid magnet with vertical field orientation. All tanks and the helium-3 quantity of 100 liters[6] are designed to allow an operation at the base temperature for 100 hours without a refill, allowing continous STM and STS measurements for that period. When the helium-3 reservoir is depleted the helium-3 may be recondensed or the STM can operate further at a temperature slightly above 4.2 K, the temperature of liquid helium-4.

The main presumed advantage of this design compared to bottom or top loading cryostats is the minimized length the STM has to move for a sample change, which is inevitably given by the height of the single bore solenoid magnet. Lesser movement usually means a cleaner sample introduction. The fact that the STM never leaves the cryostat and does not heat up at will, reduces the waiting time before it reaches its base temperature again.

3.8. Scanning tunneling microscope

There exist various designs for scanning tunneling microscopes and several instruments are available commercially. However, the requirements for the STM in this system are very specific and it has to be versatile, extensible or exchangable to accomodate for future experiments. Therefore an STM was designed for this system in particular, based on previous designs proven stable in similar systems at low temperature and in high magnetic fields [50, 41]. The main features of the STM (Figure 3.12) are a rigid compact design with non-magnetic components, an *in situ* tip exchange mechanism, a *Walker* type coarse approach (z movement) and a sample positioning stage (x, y movement). The assembly was done and a detailed description for this STM was given in a diploma thesis [51]. See also Reference [49] for detailed information about the STM, this design was based on directly. In the following just a short overview of the functionality is given.

Scanning tunneling microscopes make use of the piezoelectric effect. Applying a voltage to a piezoelectric ceramic induces strain in the material's crystal structure in a specific direction. This gives an easy access to a tip position-

[6] volume at atmospheric pressure and room temperature (21.1 °C for gas pricing)

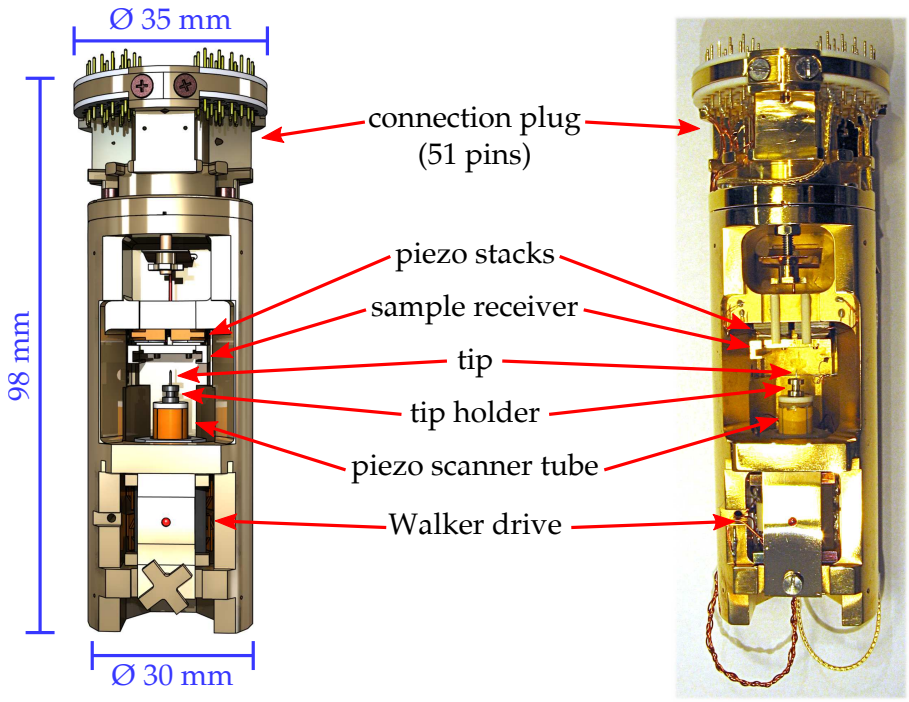

Figure 3.12.: The scanning tunneling microscope in a rendered 3D CAD image (left) and a photography of the assembled parts (right).

ing with subatomic precision. Most widely used for STM nowadays are tube shaped ceramics with multiple electrodes, that allow a surface scanning motion in all three dimensions. The range limit of such a scanner is in the µm range and temperature dependent, for the STM of this system it is about 1–2 µm. This makes a coarse approach necessary to move tip and sample in range in a controlled manner.

The chosen design for the coarse approach is based on the *Walker* motor [50], where six stacks of flat piezos hold a prism from three sides (Figure 3.13, right). In principle all six piezo stacks can move independently parallel to the main axes of the prism, sliding over it, and thus *walk*, pushing the prism forward and backward. In practice it proved easier and faster to just apply sawtooth pulses to all stacks simultaneously and move the prism in a slip stick fashion. Compared to other common designs like *Beetle* or *Inchworm*, the Walker has a large drive range and a high force. This makes the implemented tip exchange mechanism possible.

For certain STM experiments it is not only necessary to change the sample (Figure 3.14, left) within the vacuum system, which is easily done from the outside with a wobble stick manipulator and a spring loaded sample receiver, but

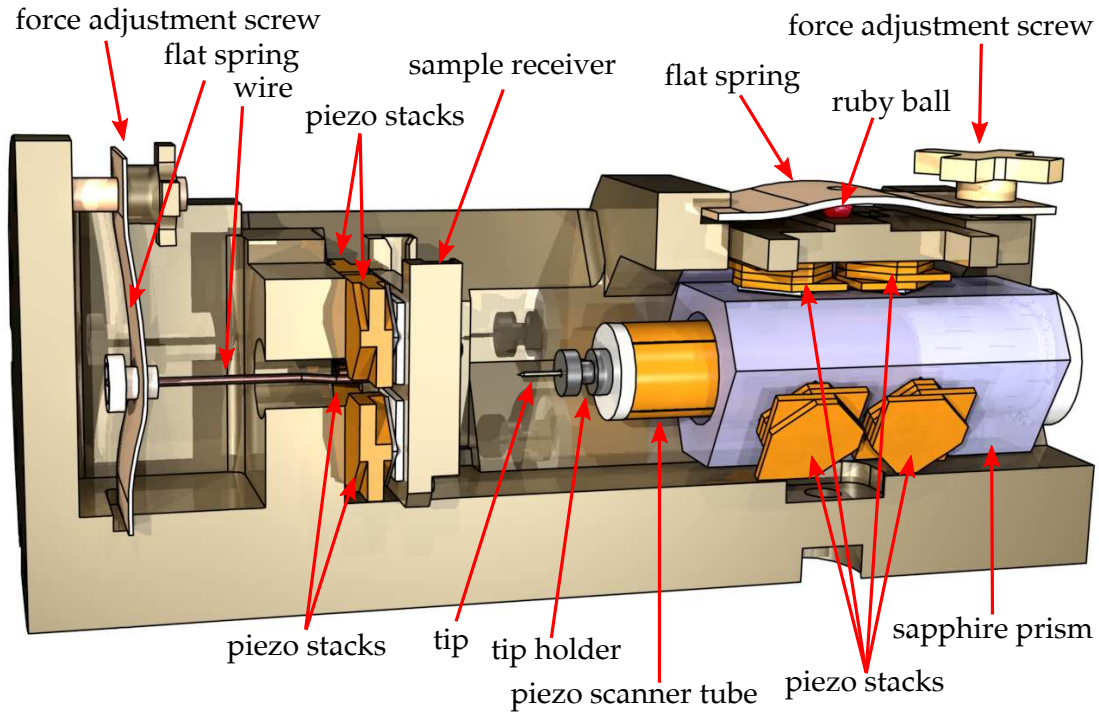

Figure 3.13.: 3D CAD rendering of a cut through the STM exhibiting the piezo drives. The xy sample positioning stage is shown on the left and the Walker coarse approach drive on the right.

also the STM tip. Some tips have to be prepared in separate vacuum chambers prior insertion into the STM, like being heated up, sharpend by argon sputtering or being coated with magnetic materials from an evaporator source. Also tip crashes are not uncommon and tips need to be replaced or prepared again from time to time. If the tip is mounted onto the tube scanner like in the design here, a tip holder and exchange mechansim should also be as light weight as possible in order to keep the resonance frequency of the scanner high. A lower resonance frequency makes the scanner more susceptible to outside excitation, producing noise in measurements. The implemented tip exchange mechanism [52] features a small metallic tip holder that fits inside the tube scanner and a bigger shuttle, that can receive the tip holder and be transported with the wobble stick manipulator (Figure 3.14, right). The Walker drive has proven to be strong enough to slide the tip holder in and out against the force of the spring fixating it, which in turn has to exert a high enough pressure onto the tip holder for stable measurements.

The newest feature implemented into this STM is the xy sample positioning stage, derived from an initial design by T. Mashoff in 2004 [53]. The sample

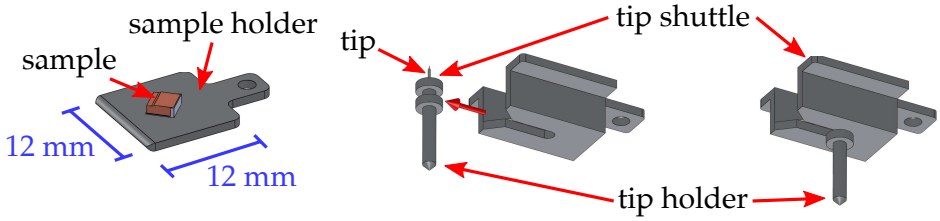

Figure 3.14.: 3D CAD drawing of a sample holder with sample (left) and an illustration of the tip shuttle and tip holder for the tip exchange mechanism (right).

receiver is pulled by a spring loaded wire onto stacks of piezo ceramics, which can move the sample receiver in a slip stick fashion (Figure 3.13, left). This stage extends the reachable scan area from 1–2 µm per direction to 1–2 mm. This enables changing the scan area if the position reachable with the scanner tube is not of much interest or contaminated by tip crash or tip preparation method residues. Fine positioning of the sample is also essential for experiments like measurements on small graphene flakes [54].

A further challenge is the material composition of the STM. It needs to be UHV compatible material, withstand bake-out temperatures of about 120 °C, and be thermally well conducting to reach a base temperature as low as 300 mK. The thermal expansion coefficients of the different materials have to be regarded so that no ceramics break due to stress and glued connections hold. The materials have to be nonmagnetic to be stable in the desired magnetic fields of up to 14 T, and they must not be superconducting at 300 mK to avoid possible measurement interference by conserved magnetic fields and a diamagnetic response to magnetic fields. The main body was therefore made from phosphor bronze (CuSn8P), which is not as good a thermal conductor as pure copper but much harder, giving the STM a higher resonance frequency and making it more stable. This material was already successfully used for a similar STM system achieving a stable base temperature of 315 mK [41]. The piezo stacks and scanner tube are PZT ceramics.[7] Touching planes for the slip stick motion are polished crystalline and polycrystalline aluminum oxide (including sapphire). As electrical insulating ceramic Macor was used and the springs and wire are made from beryllium copper. Several parts including the wiring were glued or soldered together with UHV compatible adhesives[8] and solder.[9]

[7] EBL#4, EBL Products Inc.
[8] Epotec E2101, Epotec H77
[9] Fontargen A 611 (Sn97Ag3), soft solder flux: Fontargen F 600

3.9. Support frame

In order to perform high resolution STM measurements the STM has to be isolated from external vibrations, coming from the floor the system rests on or through accoustic noise directly exciting vibrations of the UHV chamber walls. Common methods for this isolation used by room temperature or variable temperature STMs include a free hanging support of the STM by springs inside the vacuum system and a motion damping mechanism. This damping is done magnetically via eddy current or by use of UHV compatible fluoroelastomer (FKM), often called *Viton*[10]. The room temperature STM/AFM assembly in the analysis chamber actually utilizes a cascade of FKM damping stages very effectively.

For a low temperature STM with small diameter to fit into a high-field solenoid magnet these internal damping stages cannot be used so easily. Besides the size restrictions the cooled down elastomers would become stiff and permanent magnets would be subjected to the field of the large solenoid magnet. Therefore the whole UHV system is to be protected from external excitations by putting it on an air damped support frame inside of an anechoic room. A support frame made from stainless steel rectangular tubes filled with sand has been used successfully in comparable systems [41, 49]. Stainless steel is hard, weldable, and nonmagnetic as the superconducting magnet does not tolerate too much magnetic material in close proximity. The tube shape makes the frame rigid while the sand is very effective at damping any resonant vibrations of the frame.

Figure 3.15 shows the final design of the support frame for this system. The design concept of the frame is a large frame element in a plane below all parts of the chamber system, as this allows the best access while working with the system. It may also allow a removable bake-out tent to be designed around the UHV chambers. Because the cryostat as the largest and heaviest component has a high center of mass of approximately 1 m from its bottom, the air damping elements have to be elevated to ensure a stable damping. The damping feet should also be placed at even length from the estimated center of mass to even the load. For geometric reasons, requiring free access to the cryostat for operation as well as for refilling with cryogenic liquids, one of four air damping elements is connected to a V-shaped support arm. This is vibrationally worse than the other supports, since it is able to move freely in-plane.

The air damping elements[11] with a resonance frequency of about 1.5 Hz vertically and about 2.5 Hz horizontally are most effective at damping higher frequencies. The resonance frequency of the smaller air damping elements on top

[10] registered trademark of E. I. du Pont de Nemours and Company
[11] BiAir 1-ED/HE, Bilz Vibration Technology AG

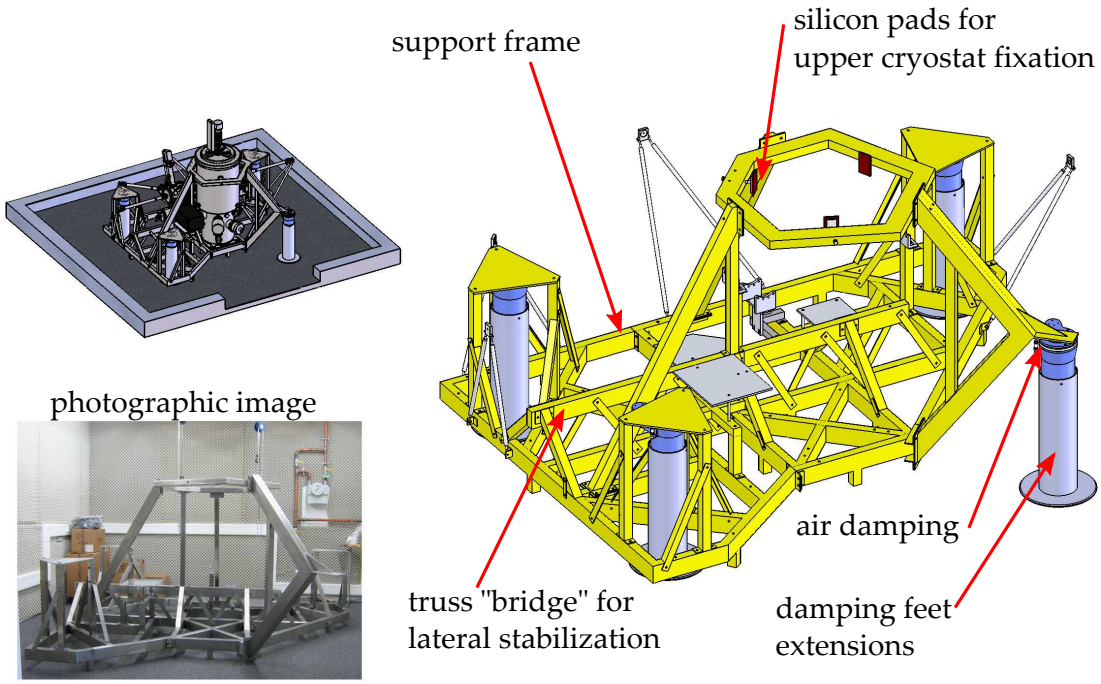

Figure 3.15.: 3D CAD drawing and a photographic image of the support frame for the complete UHV system.

of the cryostat is around 5 Hz. Therefore the lowest eigenfrequency of the support frame should be higher to not be excited or amplify a frequency of the air elements. An advantage of the 3D CAD software used for the development of the system[12] is the integrated finite element analysis software allowing to calculate eigenmodes of a draft and optimize the frame.

Figure 3.16(a–c) show the lowest three eigenmodes of a simple frame design with the cryostat mounted. The sand inside the steel tubes has been regarded by increasing the density of mass of the steel. (a) and (b) show two kind of nodding motions with the whole frame bending itself and in (c) the frame twists relative to the fixed support of the air damping elements. To counteract these modes the frame has been extended by several diagonals and an additional elevated horizontal bar for its final design. These features make the frame significantly more stiff as can be seen in (d–e) by the more homogenous coloring and less bending. All eigenmodes are now above 10 Hz and thus should not couple with the air damping feet resonantly.

[12]SolidWorks, SolidWorks Corp.

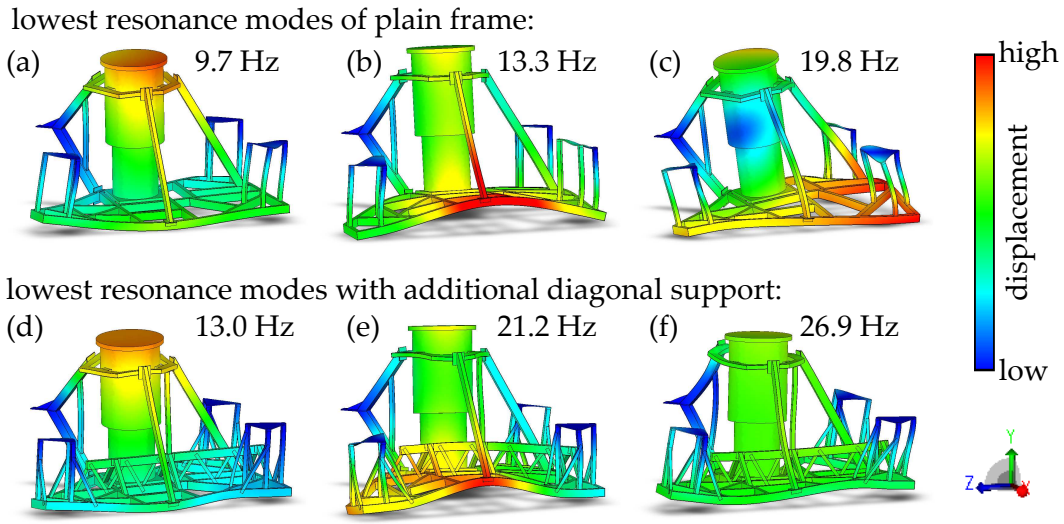

Figure 3.16.: Finite element analysis of the lowest resonance modes of the support frame with the cryostat. In (a–c) just a plain minimal frame to support the UHV system is analyzed, in (d–e) additional diagonal support has been added to the frame.

4. Two-dimensional electron systems in *p*-InSb(110)

4.1. Introduction

This chapter describes two-dimensional electron systems (2DESs) prepared at a semiconductor surface for analysis with scanning tunneling spectroscopy (STS). Previous STS experiments on such 2DESs were able to probe transitions from strong to weak localization [30] (InAs inversion layer), a spatially continuous wave pattern caused by multiple scattering [55] (InAs accumulation layer), drift states in magnetic field [6] (InAs accumulation layer), and the local density of states across quantum Hall transitions [8] (InSb accumulation layer). In this work, two different 2DESs at the (110) surface of germanium doped *p*-indium antimonide (*p*-InSb) single crystals have been analyzed in detail (InSb inversion layer). InSb has a as smaller effective electron mass in the conduction band than InAs and so the quantum Hall effect should be more prominent at comparable experimental conditions. An inversion layer has the advantage over an accumulation layer, that at the Fermi level the 2DES is separated from the bulk by the band gap as will be shown in Section 4.2.1. The first 2DES was prepared using a highly doped crystal. This 2DES has a high internal electric field exhibiting the Rashba effect in the density of states (DOS). The second 2DES, prepared using a low doped crystal, has a weaker internal electric field, but in turn here the surface 2DES states are fully decoupled from the bulk. It exhibits electron–electron interaction effects in the DOS as well as in the *local* DOS (LDOS).

After an introduction to the theoretical description of surface 2DESs (Section 4.2) the experimental procedures will be described (Section 4.3). Finally the results will be discussed for both sample systems.

4.2. Adsorbate induced two-dimensional electron systems (2DESs)

Two-dimensional electron systems can be induced in doped semiconductors by confining electrons in one dimension through an applied voltage. This is typ-

ically done in metal–oxide–semiconductor field-effect transistors (MOSFETs), where a metallic electrode is isolated from the semiconductor by an oxide layer. The applied voltage changes the charge distribution in the semiconductor, leading to a band bending which can be described by Poisson's equation. This band bending potential can lead to confined states in two dimensions as given by the time independent Schrödinger equation. Without an applied external voltage 2DESs can be created in semiconductor heterostructures by carefully matching band gaps and dopant concentrations of the layers. The charge diffusion potential can be tuned to confine electrons even in an undoped semiconductor layer, which increases the electron mobility drastically. These 2DESs cannot be probed by STS with high lateral resolution though, as they are burried below the surface.

For STS research a 2DES can be produced at a semiconductor surface by *surface doping*, which describes adsorbing a small quantity of donor atoms onto a clean semiconductor surface. The actual shape of the band bending potential here depends on the doping of the semiconductor and on the donor level of the adsorbate. The donor level for Cs atoms on InSb(110), given by the maximum band bending at the surface, has been determined by photoelectron spectroscopy to be $V_{\mathrm{bb}} = 290$ meV [56]. For a saturated coverage of Cs atoms, which is of the order of 1 % of a monolayer, this is the energy position of the Fermi level above the conduction band edge at the surface.

4.2.1. Band bending and subband calculation

An illustration of the band bending of a *p*-type semiconductor by surface doping is given in Figure 4.1. The electrons from the adsorbates charge the acceptors near the surface (*depletion* of charge carriers) and donate electrons to the inversion layer. The distance from the surface at which the acceptors are charged is the *depletion depth* z_{depl}. Two two-dimensional subbands E_i, $i \in \mathbb{N}_0$, in the conduction band are also shown in the image, the lower one is occupied as it is below the Fermi level E_{F}.

The actual curvature of the band bending is given by Poisson's equation in one dimension:

$$\frac{d^2\phi(z)}{dz^2} = -\frac{\rho(z)}{\varepsilon_0 \varepsilon_{\mathrm{r}}} \tag{4.1}$$

with electric potential $\phi(z)$, three-dimensional electron charge density distribution $\rho(z)$, electric constant ε_0 and dielectric constant ε_{r}. $\rho(z)$ consists of the density of charged acceptors, which is simply given by the bulk acceptor density

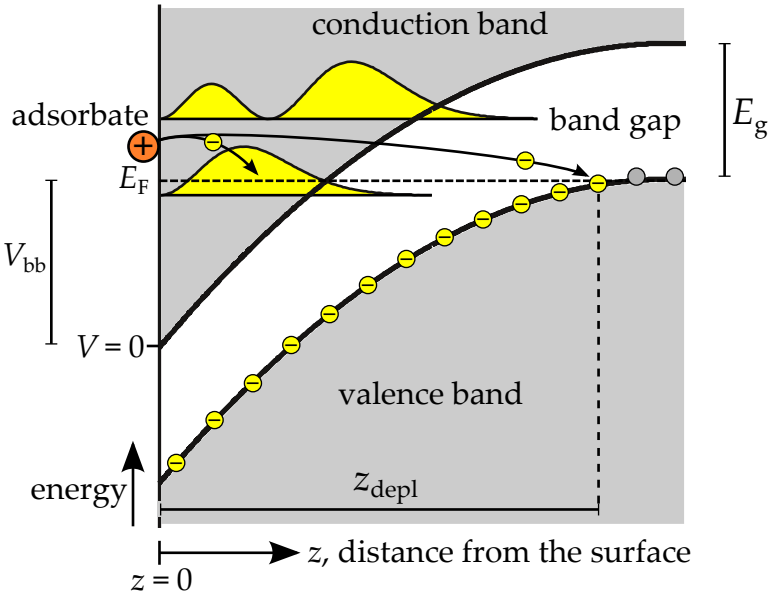

Figure 4.1.: Sketch of the surface band bending in a p-type semiconductor by surface doping. Adsorbates on the surface are ionized, donating their electrons to charge the acceptors and to fill the inversion layer consisting of electron states in the conduction band below the Fermi level E_F, confined by the vacuum barrier and the band gap. z_{depl} denotes the depth of the depletion region. V_{bb} shows the donor level of the adsorbates and $V = 0$ marks the zero of the energy scale for the subband calculations.

N_A, and the electron distribution of all (occupied) subbands:

$$\rho(z) = -e\left(N_A + \sum_i N_i \left|\psi_i(z)\right|^2\right),\ z < z_{depl}. \tag{4.2}$$

Here, e is the elementary charge, N_i the two-dimensional electron density, and $|\psi_i(z)|^2$ the one-dimensional normalized probability density function of the electrons in subband i. For $T = 0$ K, if the subband energies E_i are known and a constant effective electron mass m^* can be assumed, N_i is given by

$$N_i = \int_{E_i}^{E_F} D(E)dE \tag{4.3}$$

with the two-dimensional density of states (including spin degeneracy):

$$D(E) = \begin{cases} \dfrac{m^*}{\pi\hbar^2} & E < E_F, \\ 0 & E \geq E_F. \end{cases} \tag{4.4}$$

$\hbar$ is the reduced Planck constant. The sum over all N_i is the total inversion layer density N_s.

The subband energies E_i and the electron wavefunctions $\psi_i(z)$ are given by the time-independent Schrödinger equation in one dimension:

$$\left[-\frac{\hbar^2}{2m^*}\frac{d^2}{dz^2} + V(z)\right]\psi(z) = E_i\psi(z). \tag{4.5}$$

The confinement potential energy $V(z)$ for the band bending potential described above is given by

$$V(z) = V_\mathrm{bb} + E_\mathrm{g} - e\phi(z) \tag{4.6}$$

with the gap energy E_g. The scaling here is set for $V(0) = 0$ (compare Figure 4.1), so values for E_i are measured relative to the conduction band at the surface. As the Schrödinger equation contains the electric potential $\phi(z)$, the problem has to be solved iteratively and self-consistently. This is commonly called a *Schrödinger-Poisson* calculation.

As a starting point of the iterative calculations and as a fairly good estimate of the band bending potential without knowing any subband energies, a solution can be given straightforwardly by solving the Poisson equation with a more simplified charge distribution

$$\rho(z) = -e\left(N_\mathrm{A} + \int_0^{V_\mathrm{bb}-V(z)} D_\mathrm{3D}(E)dE\right), \tag{4.7}$$

using the 3D bulk density of states:

$$D_\mathrm{3D}(E) = \begin{cases} \dfrac{(2m^*)^{3/2}}{2\pi^2\hbar^3}\sqrt{E} & E < E_\mathrm{F}, \\ 0 & E \geq E_\mathrm{F}. \end{cases} \tag{4.8}$$

The solution of the Poisson equation only has to agree with the known boundary conditons, which can be expressed in terms of $V(z)$ of Equation (4.6) as

$$V(0) = 0, \tag{4.9}$$

$$\lim_{z\to\infty}\frac{dV(z)}{dz} = 0. \tag{4.10}$$

Triangular well approximation

A good approximation to the numerical solution of the Schrödinger equation can usually be given by approximating the potential as a triangular well where

the solutions for a given average electric field value $|\vec{E}|$ is [57, 9]:

$$\psi_i(z) = \mathrm{Ai}\left[\left(\frac{2m^* e|\vec{E}|}{\hbar^2}\right)^{1/3}\left(z - \frac{E_i}{e|\vec{E}|}\right)\right], \tag{4.11}$$

$$E_i \approx \left(\frac{\hbar^2}{2m^*}\right)^{1/3}\left[\frac{3\pi e|\vec{E}|}{2}\left(i + \frac{3}{4}\right)\right]^{2/3}. \tag{4.12}$$

Here, $\mathrm{Ai}(x)$ denotes the Airy function of the first kind. The exact solutions for E_i and the first three subbands $i = 0, 1, 2$ are given by replacing $(i + 3/4)$ with 0.7587, 1.7540, and 2.7525 respectively.

The first two solutions for $|\psi_i(z)|^2$ from the triangular well approximation are also sketched in Figure 4.1. As in this model the surface represents a potential barrier of infinite height, the wavefunctions do not penetrate the surface. For real surfaces with a finite work function this is of course not the case, which makes a probing of these 2DESs with a scanning tunneling microscope possible. Nevertheless the model results show that higher subbands have a higher mean depth. For STS this means that the STM is most sensitive to the lowest subband, giving less dI/dV signal to higher subbands. This is consistently observed for different 2DESs [55, 30, 8].

4.2.2. Nonparabolic approximation

The above calculations assume a constant effective electron mass m^*. However, the conduction band of small gap III-V semiconductors, and especially of InSb with a gap energy as low as $E_g = 0.235$ eV at $T = 0$ K [58], is highly nonparabolic. Due to the smallness of the gap the valence bands and conduction band of InSb strongly interact with each other. On the one hand this leads at the conduction band edge to the unusually small effective mass $m_0^*/m_0 = 0.0135$ ($T = 0$ K, m_0: free electron mass) [58] and large effective Landé g-factor $g_0^* = -51$ ($T \approx 1$ K) [59], making InSb a very good system to study quantum Hall physics. On the other hand the nonparabolicity of the conduction band's energy dispersion $E(k)$ (with wave number k) makes the effective mass m^* and effective Landé g-factor g^* energy dependent. For exact numerical calculations this nonparabolicity requires adjustments to the Hamiltonian of the Schrödinger equation as in $\mathbf{k} \cdot \mathbf{p}$ theory. Evan O. Kane applied this to InSb describing the interaction of one conduction band with three valence bands, also referred to as *Kane model* [60]. The nonparabolic dispersion of the Kane model is shown in Figure 4.2(a) in comparision with a parabolic dispersion. The nonparabolicity makes calculations much more complex, especially when including electric and magnetic fields. However, to gain theoretical estimates for the

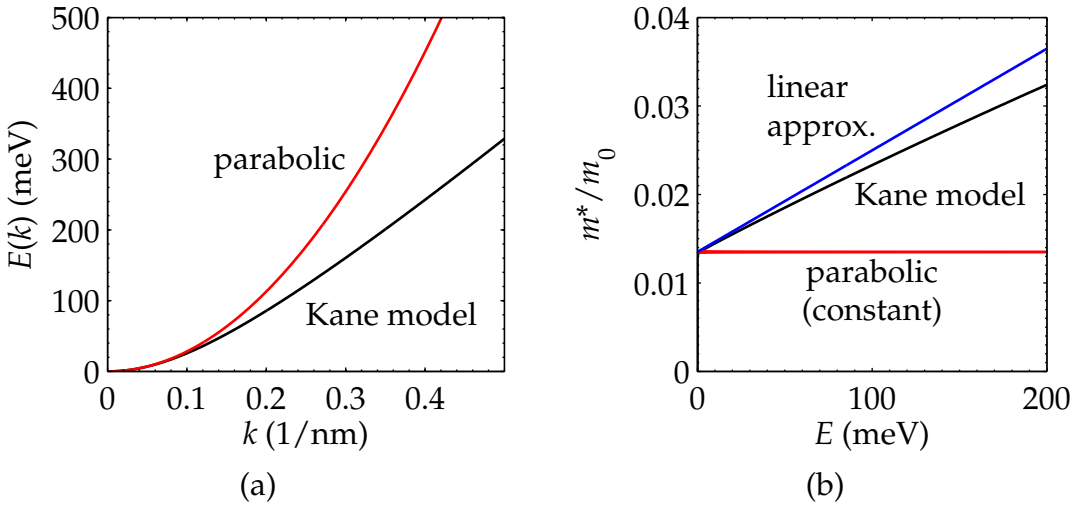

Figure 4.2.: (a) Energy dispersion of the conduction band calculated with the Kane model ($\mathbf{k} \cdot \mathbf{p}$ theory) and a parabolic dispersion with the effective mass at the conduction band minimum $m^* = 0.0135 m_0$. (b) Energy dependence of the relative effective mass m^*/m_0 (m_0: free electron mass) as gained from the Kane model and the linear approximation of Equation (4.14).

experimental data of this work it is sufficient to employ an approximation of energy dependence of m^* and g^*. The relevant effective mass here is the so-called momentum effective mass or density of states effective mass defined as [61, 62]

$$m^* = \hbar^2 k \left(\frac{dE}{dk} \right)^{-1} . \tag{4.13}$$

Figure 4.2(b) shows the effective mass as gained from the Kane model and an often employed linear approximation:

$$m^*(E) = m_0^* \left(1 + 2 \frac{E}{E_g} \right) . \tag{4.14}$$

For a 2DES the effective mass can be estimated including the triangular well approximation and a first order series expansion by [63]

$$m^*(E) = m_0^* \left(1 + 2 \frac{\frac{1}{3} E_i + E_\parallel}{E_g} \right) . \tag{4.15}$$

Here, $E = E_\parallel + E_i$ splits up into the in-plane energy $E_\parallel$ and the energy offset of the subband E_i with respect to the conduction band minimum (CBM) at the

surface E_{CBM}. $g^*(E)$ can then be given by the relation [64]:

$$\frac{g^*(E)}{g_0^*} = \frac{m_0^*}{m^*(E)}. \tag{4.16}$$

Strictly speaking this approximation is only valid for energies E small compared to the gap energy, which is not the case for the InSb inversion layer 2DESs studied here. Nevertheless the substitution of the conduction band edge values by these functions gives much better results than a plain effective mass approximation and the functions remain transparent unlike full-blown numerical treatments of the problems.

4.2.3. Landau levels and the quantum Hall effect

In a perpendicular magnetic field B the electron energies in 2D are quantized within in Landau levels. The allowed energy levels in the effective mass approximation including Zeeman splitting are given by

$$E_{i,\sigma}^n = E_i + \hbar\omega_{\mathrm{c}}(n + \frac{1}{2}) + \sigma\frac{g^*\mu_{\mathrm{B}}}{2}B \tag{4.17}$$

with subband index i, Landau level index $n \in \mathbb{N}_0$, spin index $\sigma = \pm 1$, Bohr magneton $\mu_{\mathrm{B}} = e\hbar/2m_0$ and cyclotron frequency

$$\omega_{\mathrm{c}} = \frac{eB}{m^*}. \tag{4.18}$$

This changes the constant DOS for a 2DES (Equation (4.4)) to peaks at these Landau energies, which at $T = 0$ K can be broadened by the potential disorder of the 2DES. Each spin split Landau level is degenerate by $eB/(2\pi\hbar)$. The filling factor ν, describing the number of occupied spin levels, is therefore independent of m^* and g^* and only depends upon the total number of electrons in a subband N_i and the magnetic field:

$$\nu = N_i\frac{2\pi\hbar}{eB} \tag{4.19}$$

Locally the lateral extension l_n of individual quantized electron states are given in terms of the magnetic length

$$l_{\mathrm{B}} = \sqrt{\frac{\hbar}{eB}} \simeq 9.7\ \mathrm{nm}\ (B = 7\ \mathrm{T}) \tag{4.20}$$

by

$$l_n = l_{\mathrm{B}}\sqrt{2n+1}. \tag{4.21}$$

Depending on their energy, these states can drift around on equipotential paths within an electrostatic potential landscape exhibiting larger spatial corrugation length scales than l_n [65, 66]. These paths can either be closed around potential minima or around potential maxima or they can be extended at intermediate energy throughout the whole 2DES. This transition with energy from a localized, insulating system, through an extended, conducting and back to an insulating system is called the *quantum Hall transition* since it coincides with a jump in Hall conductivity by e^2/h. Recent STS measurements on n-InSb have verified this behavior for the lowest Landau level by imaging the transition in real space [8].

4.2.4. Rashba effect in a magnetic field

The Rashba effect describes the splitting of the energy dispersion $E(k)$ for electrons in a 2DES into two branches due to spin–orbit interaction and a coupling of a perpendicular electric field $\vec{E}$ with the electron's spin [10, 11]:

$$E^{\sigma}(k) = \frac{\hbar^2 k^2}{2m^*} + \sigma \alpha k. \tag{4.22}$$

The strength of the splitting is given by the Rashba spin–orbit coupling parameter α. Figure 4.3(a) illustrates the Rashba spin splitting calculated with Equation (4.22). This is an interesting effect for spintronic applications as this gives access to spin manipulation by a macroscopic electric field that can easily be applied externally. A net electric field for a 2DES implies an asymmetric confinement potential.

Without an externally applied voltage an asymmetry of the potential is already given for a 2DES generated by surface doping, approximated in Section 4.2.1 by a triangular well. The value of the Rashba parameter α for III-V semiconductor quantum wells can be estimated using an eight band Kane model with the confining potential $V(z)$ [67]. The eight band model includes spin splitting of the four bands in the standard Kane model [60] as shown in Figure 4.3(b), describing the nonparabolicity as the interaction of the conduction band with the nearest three spin split valence bands, of which one is separated by the spin–orbit splitting energy $\Delta = 0.8$ eV ($T = 4$ K) [59]. This results in an energy E and z dependent Rashba parameter [67]:

$$\alpha(z, E) = \frac{P^2}{2} \frac{d}{dz} \left(\frac{1}{E - V(z) + E_g} - \frac{1}{E - V(z) + E_g + \Delta} \right), \tag{4.23}$$

$$P^2 = \frac{\hbar^2}{m_0^*} \frac{E_g \left(E_g + \Delta \right)}{3E_g + 2\Delta}. \tag{4.24}$$

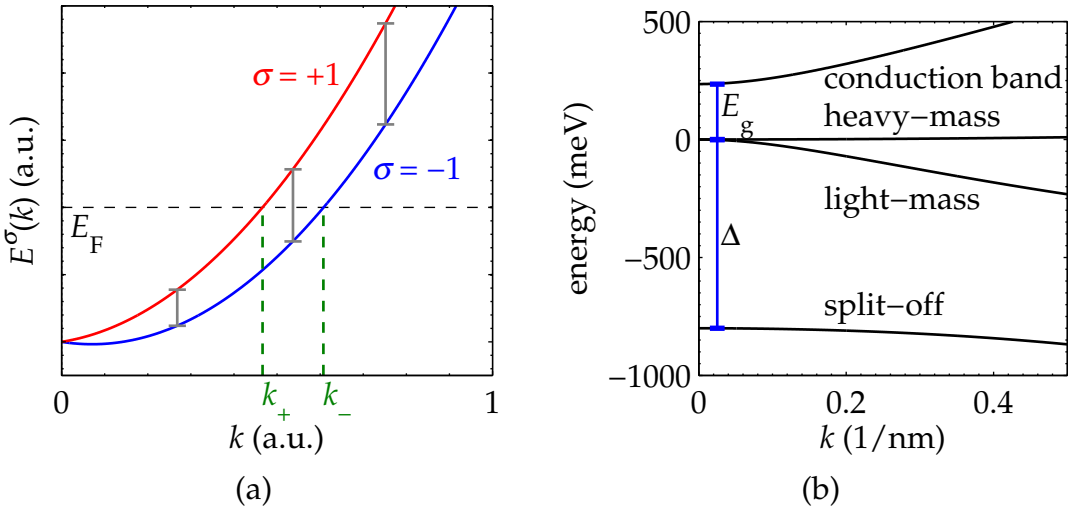

Figure 4.3.: (a) Sketch of a Rashba spin split parabolic energy dispersion. The spin splitting increases with k as indicated by the vertical bars. At the Fermi level the splitting leads to two different wave numbers k_+ and k_- as marked. (b) Calculated InSb band structure with the four band Kane model [60]. The conduction band is separated from the heavy-mass and light-mass valence bands by the gap energy E_g and the split-off valence band is separated by the spin–orbit splitting energy Δ.

An averaged value can be estimated for subband i by folding $\alpha(z, E_i)$ with the subband's wavefunction:

$$\alpha = \langle \psi_i(z) | \alpha(z, E_i) | \psi_i(z) \rangle_z. \tag{4.25}$$

As an alternative to the numerical evaluation above, an approximation of α can be given for a constant electric field $|\vec{E}| = d\phi(z)/dz$ within a subband [67]:

$$\alpha(\vec{E}) = \frac{\hbar^2}{2m_0^*} \frac{\Delta}{E_g} \frac{2E_g + \Delta}{(E_g + \Delta)(3E_g + 2\Delta)} e|\vec{E}|. \tag{4.26}$$

This shows, that in a first order approximation α is directly proportional to the strength of the electric field in these systems, and α is large for a system with large valence band spin–orbit splitting Δ compared to its band gap energy E_g. The approximation is justified for subband energies E_i that are small compared to the gap energy E_g. With the low temperature parameters of InSb this gives

$$\alpha(\vec{E}) = 5.11 \times 10^{-18} \frac{\text{eV m}}{\text{V m}^{-1}} \times |\vec{E}|. \tag{4.27}$$

In a perpendicular magnetic field with inclusion of the Rashba effect into the effective mass Hamiltonian results in Landau levels given by [10, 11]

$$E_i^{n',\sigma'} = E_i + \hbar\omega_c \left(n' + \sigma' \left(\delta^2 + \gamma^2 n' \right)^{1/2} \right), \tag{4.28}$$

$$\gamma = \alpha \left(2m^*/\hbar^3\omega_c \right)^{1/2}, \tag{4.29}$$

$$\delta = \frac{1}{2}\left(1 - \frac{m^* g^*}{2m_0} \right), \tag{4.30}$$

with level index $n' \in \mathbb{N}_0$ and spin index σ' slightly deviating from the numbering in Equation (4.17):

$$\sigma' = \begin{cases} 1, & n' = 0 \\ \pm 1, & n' \in \mathbb{N}\,. \end{cases} \tag{4.31}$$

One can easily verify that in absence of the Rashba effect ($\alpha = 0$) Equation (4.28) leads to the same levels as the well known equidistant levels of Equation (4.17).

4.3. Experimental procedure

Since the delievery of the cryostat of the 300 mK system described in Chapter 3 has been delayed by three years, the experiments were performed utilizing another low temperature STM integrated into a UHV chamber system (Figure 4.4) with similar specifications. This STM operates inside a UHV tube within a helium-4 bath cryostat with rotatable magnetic field. The base operational temperature of the STM is 5 K and the maximum magnetic field is 7 T perpendicular to the sample surface. The STM can be lifted up out of the bath cryostat into a UHV chamber for sample and tip transfer. More details regarding this system are discussed in [68, 49]. For the experiments of this work a cesium evaporator was designed (Section 4.3.1) and integrated into this UHV chamber. After a description of the evaporator the sample and tip preparation will be discussed in Sections 4.3.2 and 4.3.3.

4.3.1. Cesium evaporator

The cesium dispenser itself[1] is basically a small resistive metal foil, bent to enclose a small amount of cesium chromate while leaving a small slit opening. The dispenser with a cross section of about 1 mm^2 and a length of 12 mm has a

[1] Cs/NF/3.9/12 FT10+10, SAES Getters S.p.A.

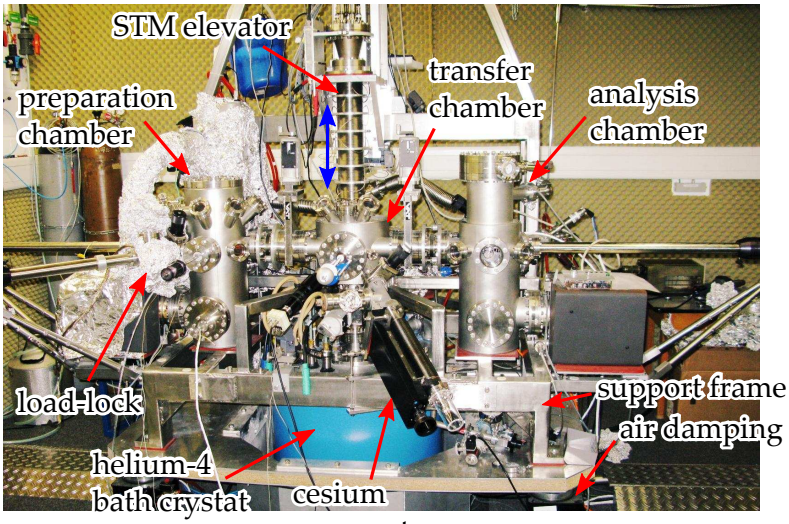

Figure 4.4.: Image of the UHV system used for the experimental measurements. The UHV chamber system above the top loading bath cryostat as described in References [68, 49] is shown here extended by an cesium (Cs) evaporator (Section 4.3.1).

total dispensable content of about 5.2 mg of cesium. When applying a high current through the dispenser unit of about 6 to 7.5 A it heats up and pure cesium is evaporated from the dispenser.

As the evaporation is not focussed, the dispenser should be close to the target for a high yield, typically a few centimeters, and it has to be easily replacable as it may become empty within a few cycles. The dispenser was therefore mounted onto a linear drive as shown in Figure 4.5 with valves for an independent venting and bake-out. It is contacted and held in place by molybdenum clamps, electrically insulated from the main body by aluminum oxide. An additional slit opening in front of the dispenser is designed to allow an evaporation directly at a sample surface inside the STM while shielding the remaining STM body and wiring. Additionally a type K thermocouple wire has been spot welded to the dispenser body for temperature control.

In preparation of each evaporation process the dispenser is heated with a low current to about 300 K to 400 K for several hours. At this temperature, no cesium is released, but the surrounding parts get hotter than during an actual evaporation process. This is necessary for a clean, water-free evaporation. After a cooling down to ambient temperature, the dispenser is heated up fast by applying a high current to a temperature above 500 to 600 °C, at which the cesium evaporation starts. The evaporation process takes roughly 2 minutes.

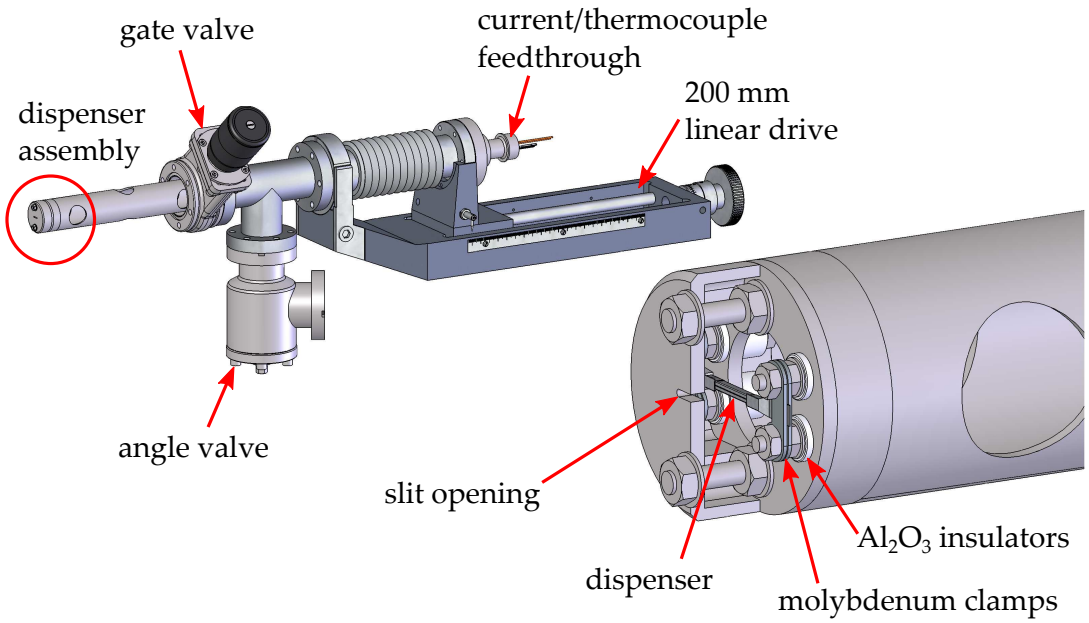

Figure 4.5.: 3D CAD view of the Cs evaporator. The Cs dispenser unit is mounted and electrically contacted by molybdenum clamps behind a slit opening at the end of a stainless steel tube inside of an linear drive.

The actual amount of evaporated cesium can be checked by STM topography measurements.

4.3.2. InSb sample preparation

The STS analysis of the semiconductor samples in this work requires atomically flat and clean surfaces. For this, the sample surfaces have to be prepared in UHV. This is done through mechanically cleaving single crystal samples in the load lock chamber after a bake-out. The structure of an InSb single crystal allows a smooth cleaving along the (110) surface.

As bulk sample material, two different InSb single crystals with different dopant concentrations are used. The crystals with a length of 1–2 cm and base dimensions of 3 mm $\times$ 3 mm are glued using conductive silver epoxy onto a molybdenum sample holder (Figure 4.6). The (110) surface is pointing upwards. For a predetermined cleavage position a small slit has been cut about 1 mm deep, 1–2 mm above the sample holder, into the crystal as shown in Figures 4.6(a) and (c). For elongation a stainless steel screw has been glued additionally on top of the crystal. By transfering the sample in this configuration

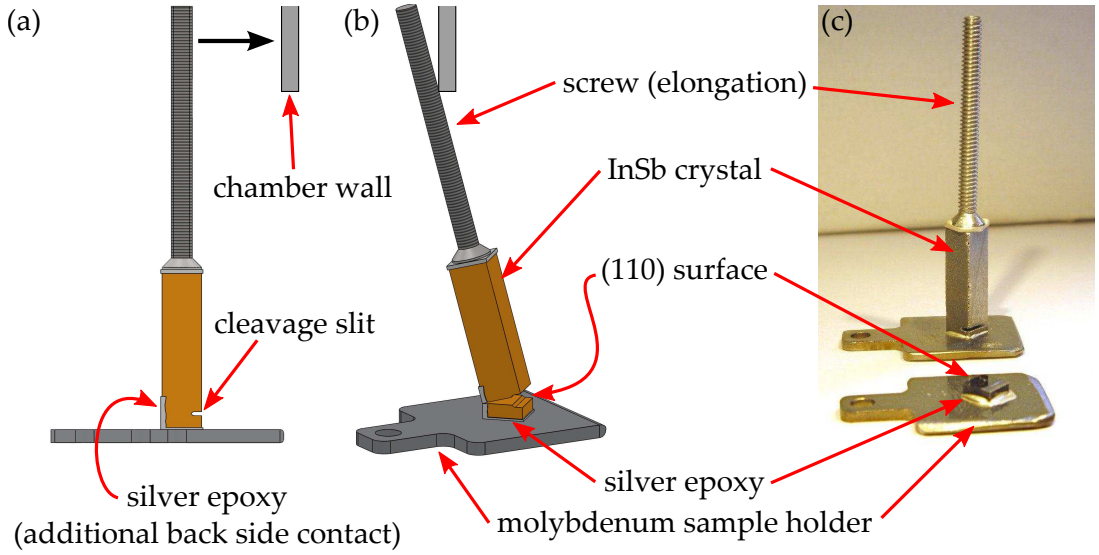

Figure 4.6.: Illustration of the InSb(110) sample preparation: (a) Drawing of a InSb single crystal before cleavage, glued to a molybdenum sample holder with silver conductive epoxy. (b) Cleaving process of the crystal. (c) Image of a prepared InSb sample and a cleaved crystal.

from the load lock to the remaining chamber system the crystal is cleaved by the chamber wall as sketched in Figure 4.6(b).

In Figures 4.6(a) and (b) the crystal's back side is also made conductive with silver epoxy. This serves as electrical contact to the surface, if the induced depletion region (Section 4.2.1) beneath the surface is too large to allow direct tunneling. This proved neccessary for experiments with the low-doped *p*-InSb crystal (Section 4.5.1), the highly doped crystals shown in (c) do not need this additional electrode.

To prevent an unwanted contamination of the clean (110) surface, the sample is quickly transfered into the STM, that has been lifted into the transfer chamber beforehand. Cesium is then evaporated onto the crystal surface as described in Section 4.3.1. After that the STM is lowered immediately back into the crystat, where the sample is protected from contamination by the helium cooled surroundings. The vacuum quality inside the cryostat allows a probing of each sample for weeks without any noticable change in adsorbate density.

The temperature of the STM stays below 50 K during the whole preparation procedure, thus the sample is cooled as it is first introduced into the STM. This is important as otherwise the cesium atoms would diffuse at the surface and gather in chain structures [69]. This would break the desired homogenious distribution of surface donor atoms. Figure 4.7 shows an STM topography image

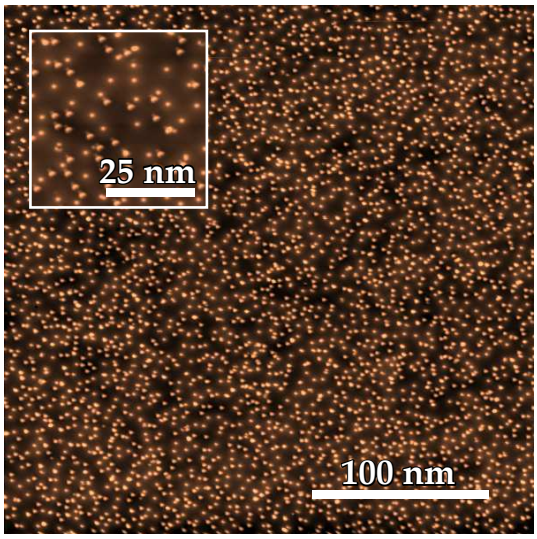

Figure 4.7.: STM topography image of InSb(110) with 1.1 % Cs coverage (sample II); $V = 300$ mV, $I = 30$ pA, 300 nm $\times$ 300 nm. The inset shows an area of 50 nm $\times$ 50 nm from a separate measurement with $V = 300$ mV, $I = 50$ pA.

of a produced sample surface. The image area is atomically flat and each bright dot corresponds to a charged single cesium atom or, partly, to a cesium dimer which both act as donors. 3300 adsorbates are visible which corresponds to a coverage of 1.1 % per InSb(110) surface unit cell. Table 4.1 lists the properties of the two samples prepared and discussed in this work.

Description	**Sample I**	**Sample II**	**Unit**
Dopant concentration (N_A)	1–2 $\times 10^{24}$	1.1 $\times 10^{21}$	m^{-3}
Cs coverage (N_{Cs})	5.1 $\times 10^{16}$	3.7 $\times 10^{16}$	m^{-2}
Cs per surface unit cell	1.5 %	1.1 %	

Table 4.1.: prepared InSb samples

4.3.3. STM tip preparation

The STM tip itself was prepared *ex-situ* by chemical etching from a tungsten wire with 0.2 nm diameter. Inside the STM it was further prepared by field emission and consecutive voltage pulses on a W(110) surface prior the first InSb sample preparation. Voltage pulses on the InSb(110) surface were further applied to prepare the microtip, the end of the tip with the actual atoms responsi-

ble for tunneling. This is needed after small tip crashes, to increase stability, or to change the tip's work function not to induce a quantum dot below the tip [70]. Usually after voltage pulses on InSb, the sample area had to be changed with the xy sample positioning stage, as the surface became rough or contaminated with additonal adsorbates. These methods allowed the usage of a single STM tip for all measurements without having to use of the tip exchange mechanism. This would have required preparing a new sample.

4.4. 2DES in highly doped p-InSb(110)

This section discusses the 2DES prepared on the highly doped p-InSb(110) sample (sample I of Table 4.1). After a description of the band bending profile and estimates of the subband properties (Section 4.4.1), the standing electron wave pattern of the 2DES is shown and discussed with the energy dispersion relation $E(k)$ (Section 4.4.2). The electric disorder potential affecting the Landau states in a perpendicular magnetic field is discussed in Section 4.4.3 and, finally, Section 4.4.4 shows that the measured spectrum can be associated with the Rashba effect and is in good agreement with a theoretical estimate.

4.4.1. Band bending profile

The calculated band bending profile and two-dimensional subband energies $E_{0,\text{theo}} = 270$ meV and $E_{1,\text{theo}} = 410$ meV for the first sample are shown in Figure 4.8. As described in Section 4.2.1 the band bending profile below the surface depends on the charge concentration of the occupied two-dimensional subbands and the acceptor density N_A. A higher N_A steepens the triangular confinement potential which in turn increases the energy level of all subbands E_i and also their separation $E_{i+1} - E_i$. N_A of this sample is so high, that the influence of N_s on the band bending profile can be neglected. This reduces the self-consistent Schrödinger-Poisson calculation to a straightforward solution of the Poisson equation and an inverted parabolic potential. The high acceptor density also causes a large estimated energy range of $E_{1,\text{theo}} - E_{0,\text{theo}} = 140$ meV at which the first subband can be probed without interference from higher subbands. The steep band bending itself describes a high electric field, which is the basic requirement for the Rashba effect. The average electric field of subband i is defined as

$$|\vec{E}_i| = \langle \psi_i(z) || \vec{E}(z) || \psi_i(z) \rangle_z, \tag{4.32}$$

$$\vec{E}(z) = \frac{d\phi(z)}{dz} \hat{e}_z, \tag{4.33}$$

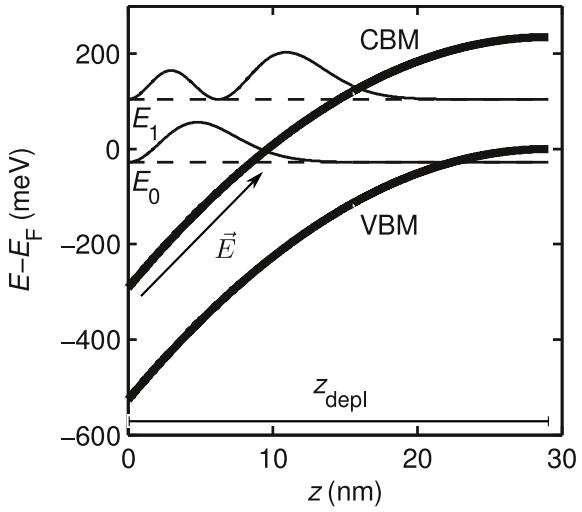

Figure 4.8.: Calculated band bending for the 2DES: conduction band minimum (CBM), valence band maximum (VBM) and subband energies E_0, E_1 are plotted as a function of distance z from the surface. The assumed acceptor concentration and electron concentration of the 2DES are $N_{\mathrm{A}} = 1 \times 10^{24}$ m^{-3} and $N_{\mathrm{s}} = 6.5 \times 10^{15}$ m^{-2}, respectively, in accordance with experimental data. The electron distribution curves $|\psi_i(z)|^2$ resulting from a triangular well approximation are drawn for each subband. The depletion length $z_{\mathrm{depl}} = 29$ nm and the electric field visible within the first subband $|\vec{E}_0| = 3.1 \times 10^7$ V/m are additionally marked.

with unit vector in z direction $\hat{e}_z$. The strength of the field for the first subband can thus be estimated to $|\vec{E}_0| = 3.1 \times 10^7$ V/m.

A spatially averaged STS measurement reveals the positions of the first two subbands as steps in the density of states (DOS) as can be seen in the lower curve of Figure 4.9. These steps are not discrete due to the potential disorder of the 2DES [55]. The marked experimental values relative to the Fermi level (sample voltage $V = 0$) nicely agree with the calculated values. Assuming the full band bending energy at the surface of $V_{\mathrm{bb}} = 290$ meV their absolute values are $E_0 = 230$ mV and $E_1 = 400$ mV. These values are slightly lower than the theoretical estimates which is not surprising as the model neglects penetration of the electrons into the vacuum and into the valence band, which both lowers their energies.

The experimental data and the theoretical calculation both clearly state that this sample has a single occupied subband and the second subband is well above the Fermi level. Spatially resolved STS images of first subband can there-

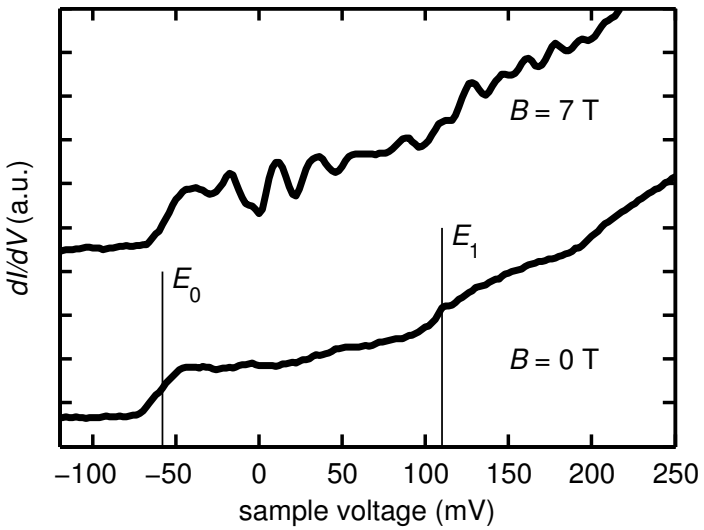

Figure 4.9.: Spatially averaged dI/dV curves measured at $B = 0$ T and $B = 7$ T as indicated, $V_{\text{stab}} = 300$ mV, $I_{\text{stab}} = 200$ pA, $V_{\text{mod}} = 1$ mV_{rms}. 12×12 spectra were taken over an area of 300 nm $\times$ 300 nm. The subbands E_0 and E_1 are marked at -60 mV and 110 mV, respectively.

fore be taken for a large energy scale of the two-dimensional electrons and even at the Fermi level as discussed in Section 4.4.2.

In strong perpendicular magnetic fields Landau quantization is expected with discrete energy levels in the density of states (Section 4.2.3), broadened by the potential disorder. This behavivor is shown spatially resolved in Section 4.4.3. The spatially averaged measurement at $B = 7$ T in Figure 4.9 (upper curve) shows a more complex pattern of the DOS. This pattern is attributed to the Rashba effect and discussed in detail in Section 4.4.4.

4.4.2. Electron wave patterns and energy dispersion

Spatially resolved $dI/dV(x,y)$ (LDOS) measurements without magnetic field are shown in Figure 4.10(b)–(j). One observes the evolution of standing wave patterns exhibiting decreasing wave length with increasing energy. These patterns are very similar to the ones observed within a 2DES induced by Fe on n-type InAs(110) [55]. The small black dots appearing in all dI/dV images at the same position are the Cs atoms, which appear dark due to the larger distance of the tip with respect to the InSb surface. The insets show the Fast Fourier

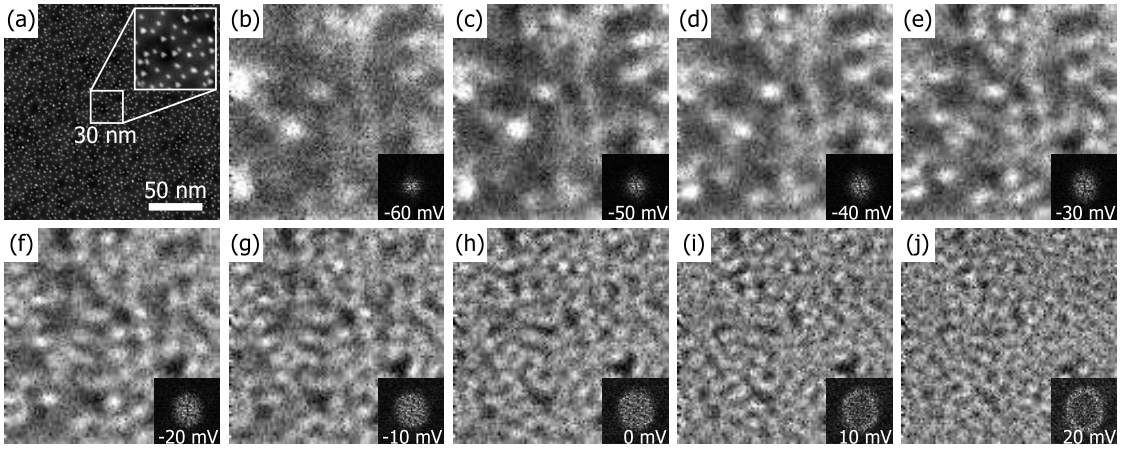

Figure 4.10.: (a) STM constant-current image of InSb(110) covered with 1.5 % of a monolayer Cs; Cs adsorbates appear as white dots; the size of the inset is indicated by the white rectangle; 200 nm $\times$ 200 nm, $V = 300$ mV, $I = 100$ pA; (b)–(j) $dI/dV(x,y)$ images of the same surface area as shown in (a) recorded at $V = -60$ mV to $V = 20$ mV as marked in the insets; $V_{\mathrm{stab}} = 300\,\mathrm{mV}$, $I_{\mathrm{stab}} = 100\,\mathrm{pA}$, $V_{\mathrm{mod}} = 1\,\mathrm{mV_{rms}}$, pixel resolution: 2 nm; insets show Fourier transformations of the real-space images displaying the electron wave vectors contributing to the LDOS(x,y).

Transformations (FFTs) of the real-space images displaying the electron wave vectors $\vec{k}$ contributing to the real-space pattern of the LDOS with $\vec{k} = \vec{0}/\mathrm{nm}$ being in the center. In the ideal case of a 2DES with negligible potential disorder and at $T = 0$ K, the FFT would show a ring, growing in diameter with the nonparabolic energy dispersion relation $E(k)$. The contribution of larger k values with increasing energy can indeed be deduced from the growing disc in the FFTs at low energy, which develops into a ring structure at about $V = 0$ mV still increasing in diameter with energy.

The contrast of the ring can be improved by recording larger images with a higher spatial resolution as shown in Figure 4.11(a) for the wave pattern at E_{F}. A clear ring structure appears in the FFT image, which is difficult to observe in Figure 4.10(h). The transition from a disk-like appearance towards a ring-structure with remaining intensity in the center of the ring has been observed previously for a disordered 2DES [55]. There, it has been reproduced by Hartree calculations taking into account the potential disorder of the 2DES, produced by the charged dopants. For strongly disordered systems, one observes only the disk increasing in diameter with energy [30]. Thus, the FFTs, not being perfect ring structures, indicate the wave function mixing by the spatially fluctuating

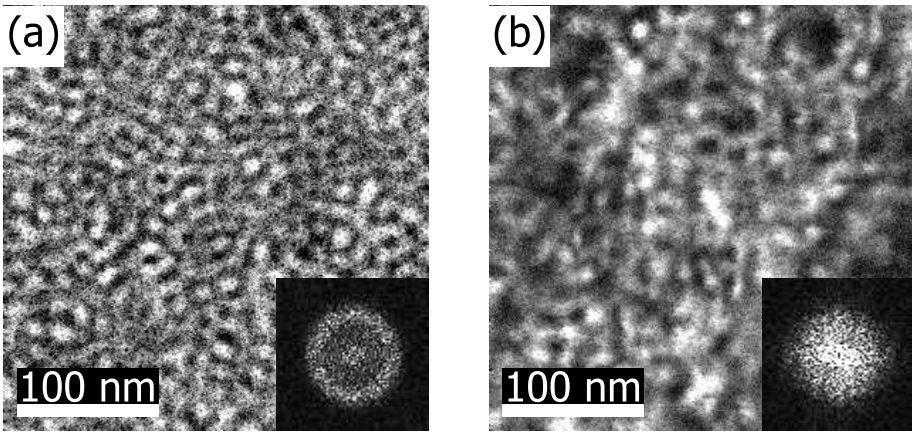

Figure 4.11.: (a), (b) $dI/dV(x,y)$ images recorded at the Fermi energy ($V = 0$ mV) at $B = 0$ T (a) and $B = 7$ T (b); 300 nm $\times$ 300 nm, $V_{\text{stab}} = 300$ mV, $I_{\text{stab}} = 200$ pA, $V_{\text{mod}} = 1$ mV$_{\text{rms}}$, pixel resolution: 1 nm; insets show Fourier transformations of real space data.

electric potential due to charged dopants. In accordance with expectations, the wave function mixing gets reduced with increasing energy.

The electron wave number k can be extracted from the FFTs as shown in Figures 4.12(a) and (b). Both plots show a radial average of the corresponding FFTs at $V = 0$ V. While in (a) the amplitude of the FFT shows a clear maximum of the ring due to the better resolution in this measurement, this k value in (b) marks the edge of the disk. Note that the dI/dV images show a pattern of standing electron waves, so the electron wave vector k is just half of the extracted values k_{image}. Correspondingly, the gained k values for energies below E_{F}, showing only disks, have larger errors of 0.5 nm^{-1} than the k values extracted from FFT images showning ring structures with a clear maximum, that can be determined to about ± 0.1 nm^{-1}.

Figure 4.13 shows the dominant k values extracted from the FFT images in Figures 4.10 and 4.11. They are displayed as dots in comparison with a theoretical upper and lower limit of the expected InSb dispersion. The upper limit is a parabolic dispersion resulting from the effective mass $m^* = 0.022 \times m_0$ at the onset of the 2DES E_0. It neglects the nonparabolicity within the 2DES. The lower curve is obtained by solving Equations (4.13) and (4.15) numerically, which overestimates the nonparabolicity at the high energies of the 2D electrons by neglecting higher order terms of $\mathbf{k} \cdot \mathbf{p}$ theory [63, 67]. A full numerical treatment of the $\mathbf{k} \cdot \mathbf{p}$ Kane model [62] would require extensive additional calculations. Nevertheless, the experimental data points are found in between the two limits evidencing that the wave patterns of Figure 4.10 are indeed caused by the

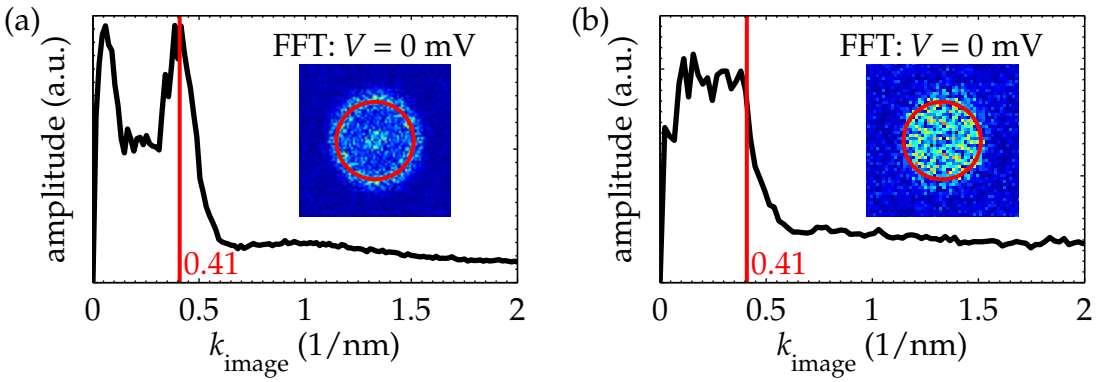

Figure 4.12.: Extraction of k from the fast Fourier transforms (FFTs) shown for Figure 4.11(a) in (a) and for Figure 4.10(h) in (b). The plots show the radial average of the corresponding FFTs. The extracted wave number k_{image} belongs to standing electron waves, so it relates to k of the electrons as $k = k_{\text{image}}/2$.

electrons of the 2DES, although the reason why the k values are so much closer to the parabolic dispersion than to the approximation is not clear. A possible explanation is the interaction of the electrons with the strong potential disorder, leading to mixing of the wave functions [55, 71].

Interestingly, the wave pattern intensity is rather continuously distributed over the area of Figures 4.10 and 4.11(a). This can be most clearly seen in Figure 4.11(a) and is in contradiction to expectations from single point scattering, where a reduction of intensity I with distance r from the scatterer according to $I(r) \propto r^{-1}$ is expected [72]. One reason might be that this discrepancy is influenced by multiple scattering paths to the standing wave pattern, which are known to be considerably more important in 2D than in 3D [73]. Another reason might be the large number of scatterers within the image area of Figure 4.10. This number can be estimated with the help of the depth of the 2DES as displayed in Figure 4.8 (9 nm), the acceptor concentration (10^{24} m^{-3}) and the image size ((200 nm)^2). This results in 360 acceptors scattering the electron waves within Figure 4.10. The number of scatterers are visualized in a simulation of the electric potential in Figure 4.15 discussed in Section 4.4.3.

The corrugation K of the wave patterns, which is caused by the strength of the scattering and the phase coherence length, is displayed in Figure 4.14(a). It is calculated by two different methods using the histograms of dI/dV values within an image as shown in Figure 4.14(b). The first method determines the difference between the mean value C_{mean} and the minimum value C_{min} and divides it by C_{mean}: $K = (C_{\text{mean}} - C_{\text{min}})/C_{\text{mean}}$. The second method instead

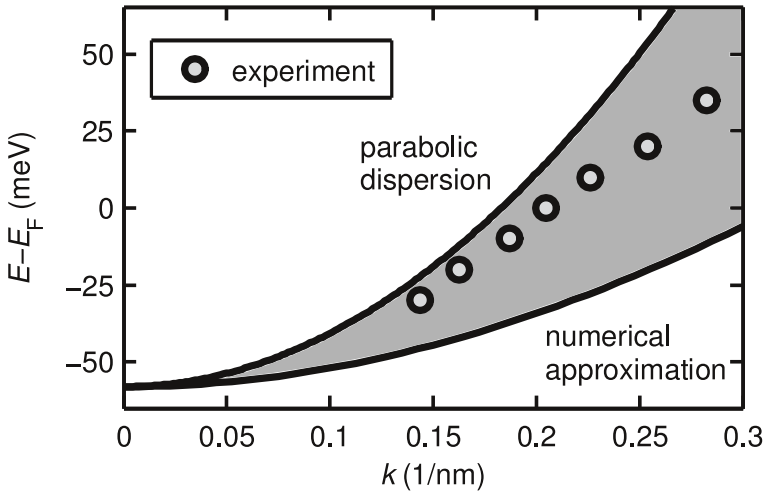

Figure 4.13.: The electron energy E relative to the Fermi energy E_F is plotted against the k value parallel to the 2DES layer. The dots represent the dominant k values extracted from Figure 4.10 (e)–(j). The upper line shows a parabolic dispersion with the estimated effective mass of $m^* = 0.022 \times m_0$ at the subband edge. The lower curve is a numerical solution of Equation (4.13) and Equation (4.15). The deviation from the parabolic dispersion marks the nonparabolicity of the 2D conduction band dispersion of InSb, the deviation from the numerical approximation might be caused by the influence of higher order terms in $\mathbf{k} \cdot \mathbf{p}$ theory.

uses twice the standard deviation of the histogram C_{std} and divides it by C_{mean}: $K = 2 \times C_{std}/C_{mean}$. Both approaches give similar results except at low energy as visible in Figure 4.14(a). In previous STS studies, the first method has been used revealing that a 2DES ($K = 60$ %) is prone to a much larger K value than a three-dimensional system ($K = 3$ %), even if the potential disorder is quite similar [74]. Moreover, a drop of K from 90 % to 50 % has been found in a strongly disordered 2D system at the percolation transition of strongly localized states [30]. The K values for this sample are compatible with the previous values obtained on 2DESs, but, other than in the previous publications, K becomes continuously smaller with increasing energy. The decrease of K with energy can be explained straightforwardly by the increase of the scattering length with energy. However, the difference with respect to the previous data is not completely clear.

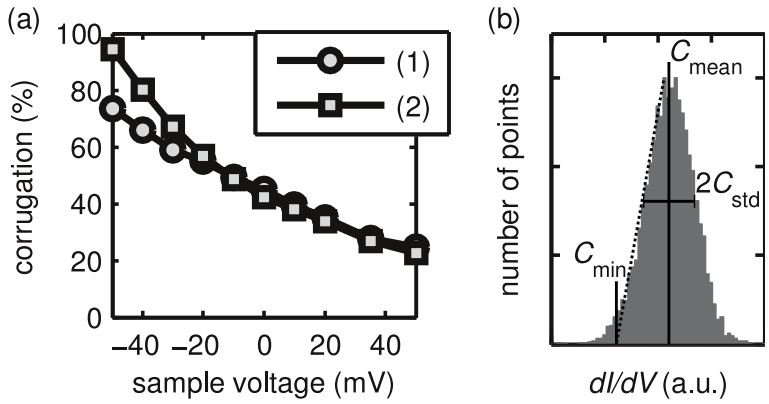

Figure 4.14.: (a) Corrugations K of the electron wave patterns within the first subband; (1) $K = (C_{mean} - C_{min})/C_{mean}$, (2) $K = (2 \times C_{std})/C_{mean}$ with C_{std}, C_{mean} and C_{min} being standard deviation, mean and minimum in the intensity distribution of the dI/dV images. (b) Histogram of Figure 4.10(h) indicating the derived values. C_{min} marks the dI/dV offset from a linear fit of the left slope (dotted line) of the histogram which amounts to cutting off the lowest 2 % of dI/dV values. C_{mean} and C_{std} are calculated numerically.

4.4.3. Percolation and potential disorder

In a perpendicular magnetic field of $B = 7$ T the dI/dV image recorded at the same sample position as Figure 4.11(a) using exactly the same tunneling parameters is shown in Figure 4.11(b). The pattern looks much more disordered and a dominant wave length is not visible anymore as evidenced by the FFT in the inset. The magnetic field leads to Landau quantization and spin splitting of the 2D electrons as stated in Section 4.2.3. The pattern in Figure 4.11(b) is so complex because it represents electrons in multiple Landau orbital and spin states within the electrical potential landscape.

Within an electric potential landscape, the Landau states experience an additional electric field perpendicular to the B field, which leads to drift states, i.e. states covering closed equipotential lines of the disorder [65, 66]. At the lowest possible energy, the first Landau level starts with states at potential pits representing localized electrons. With increasing energy, the equipotential lines representing the states encompass an increasing area until they percolate at the critical energy close to the center of the Landau level. There, the extended critical state of the quantum Hall transition appears. At even higher energy, the states localize again by covering equipotential lines circulating around potential maxima. This behavior, taking place in each Landau and spin level, has

been observed directly by STS at $T = 0.3$ K [8]. A similar percolation of states in B field has also been observed on graphite surfaces [75] and graphene [76, 77].

If the amplitude of the electric potential disorder is larger than the Landau level and spin splitting energies, higher Landau levels are present in potential pits at the same energies as lower levels around the potental maxima. The electric potential disorder is mainly caused by the charged acceptors randomly located within the inversion layer. The Cs atoms, which are only partly ionized [78], have a minor effect [55]. A simulation of the effective electric potential is shown in Figure 4.15. For this simulation, charged acceptors with a density of

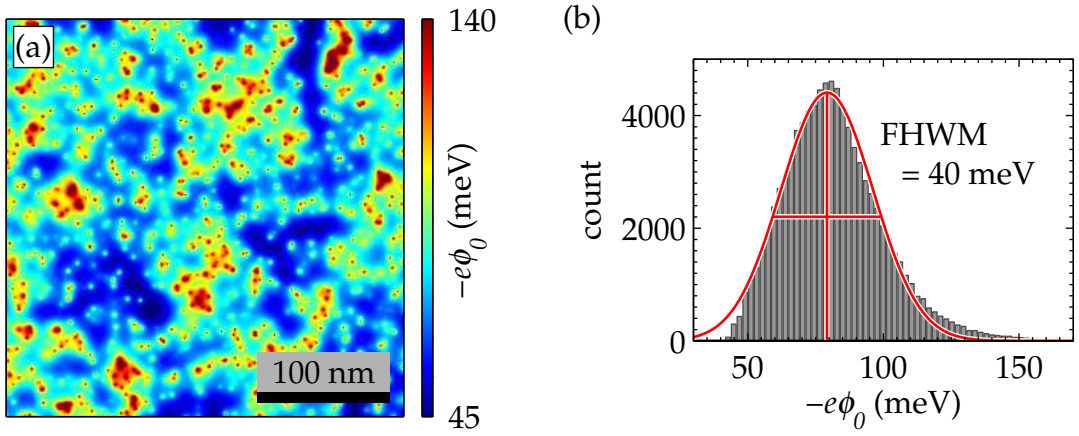

Figure 4.15.: Simulation of the effective electric potential landscape for the first subband of sample I; 300 nm × 300 nm, 300 px × 300 px

$N_A = 10^{24}$ m^{-3} have been placed randomly in an x, y area nine times the image area and in z direction down to the depletion depth $z_{depl} = 29$ nm. The screened Coulomb potentials $\phi^j(x, y, z)$ of all acceptors j has then been calculated for all x, y positions of the image area and for 50 slices in z direction from $z = 0$ down to $z = 20$ nm.

Within the depletion region only the two-dimensional electrons are free to screen the internal potential. As a first approximation of the screening the three dimensional solution for the Thomas–Fermi screening potential has been taken [79]:

$$\phi(x, y, z) = \sum_j \phi^j(x, y, z), \tag{4.34}$$

$$\phi^j(x, y, z) = \frac{-e}{4\pi\varepsilon_0\varepsilon_r r_j} \exp\left(-\frac{r_j}{r_{TF}}\right) \tag{4.35}$$

with Thomas–Fermi screening length r_{TF} and r_j being the distance of each acceptor j to the current position given by (x, y, z). Using as charge density n_c

the inversion layer electron concentration distributed over the depth of the first subband:

$$n_c = \frac{N_s}{(9\text{ nm})} = 7.2 \times 10^{23}\text{ m}^{-3} \tag{4.36}$$

and with an effective mass of $m^* = 0.022m_0$ the screening length has thus been estimated to [79]:

$$r_{TF} = \sqrt{\frac{\varepsilon_0\varepsilon_r\hbar^2\pi^{4/3}}{m^*e^2(3n_c)^{1/3}}} \approx 11\text{ nm}. \tag{4.37}$$

Finally to gain the effective potential, the electric field has been folded with the wave function of the first subband:

$$\phi_0(x,y) = \langle\psi_0(z)|\phi(x,y,z)|\psi_0(z)\rangle_z. \tag{4.38}$$

Because here the interest is only in the lateral distribution of the potential, the $\phi_0(x,y)$ of this simulation does not include the band bending of $\phi(z)$ used in the calculations of Section 4.2.1.

The histogram in (b) shows a distribution of the potential with a full width at half maximum (FWHM) of 40 mV gained by a Gaussian fit. This is larger than the expected Landau level and spin splitting at $B = 7$ T in InSb when taking the estimated values for $m^*/m_0 = 0.022$ and $g^* = -29$ at the onset of the first subband:

$$\Delta_{LL,\,theo} = \hbar\omega_c = \frac{\hbar e}{m^*}B \qquad \approx 37\text{ meV} \qquad (B = 7\text{ T}), \tag{4.39}$$

$$\Delta_{spin,\,theo} = |g^*|\mu_B B \qquad \approx 12\text{ meV} \qquad (B = 7\text{ T}). \tag{4.40}$$

The effective potential for the two-dimensional electrons in a magnetic field is smoother than the one shown in Figure 4.15(a) though, because the Landau states have finite extensions (Equation (4.21)) and do not necessarily cover the full x,y area equally. Smoothing the potential by averaging with 10 nm circles throughout the image still gives a disorder FWHM of about 38 mV as shown in Figure 4.16. This means that for this sample it can not be expected to resolve individual Landau and spin levels in spatially averaged measurements, i.e. the DOS, at $B = 7$ T, as the measurement in Figure 4.9 (upper curve) has already shown. Although the lateral extensions of higher Landau levels are larger and so the effective potential more smooth, the nonparabolicity of InSb leads to a decrease of the splitting and overcompensates this effect.

In local STS measurements on the other hand different electron states can be resolved at least for the first Landau level. Figures 4.17(a)–(f) display dI/dV images at $B = 7$ T at increasing sample voltage. The circle drawn in each image

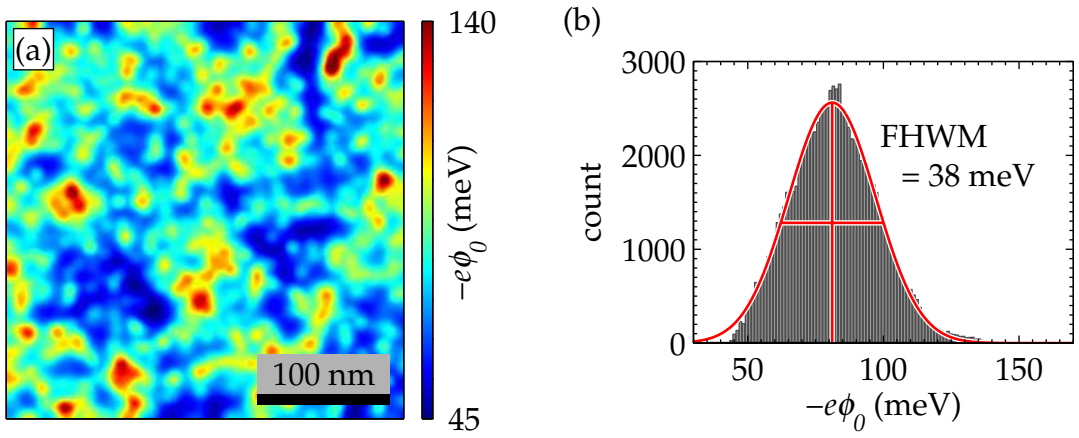

Figure 4.16.: (a) Potential landscape as shown in Figure 4.15(a), smoothed by a 10 nm circle to account for the finite extensions of Landau states at $B = 7$ T.

marks a potential pit, since it shows dI/dV intensity already at the lowest energies. The square, in contrast, marks an area, where the potential is relatively high, i.e. the dI/dV intensity appears only at rather high energy. The curves taken at these positions are shown in Figures 4.17(g) and indeed exhibit a pair of peaks shifted by approximately 20 meV with respect to each other. One can identify the doublet as the first spin split Landau level, which would result in $|g^*| = 32$ for the spin splitting and $m^* = 0.020 \times m_0$ for the distance to the next Landau level observed within the pit. This is in excellent agreement with the values $|g^*| = 31$ and $m^* = 0.022 \times m_0$ calculated for the subband edge E_0 from first-order $\mathbf{k} \cdot \mathbf{p}$ theory (Equations (4.15) and (4.16)).

By comparing the two curves of Figures 4.17(g), an effective disorder potential with a potential fluctuation of about $\Delta_{\mathrm{dis}} \simeq 20$ meV can be deduced. This is smaller than expected from the simulations above, maybe because of screening properties of the Cs layer at the surface that are not included in the model. The disorder is still larger than in a previously analyzed 2DES prepared by Cs coverage on n-InSb(110), showing a disorder of $\Delta_{\mathrm{dis}} \simeq 10$–$15$ meV, deduced from the broadening of the lowest spin level at $T = 300$ mK and $B = 12$ T [8]. By regarding the distance of square and circle in Figure 4.17(a)–(e), a spatial length scale of the potential corrugation of about 30 nm can be deduced.

Since the potential fluctuation is still larger than the spin splitting, it is difficult to observe the appearance and disappearance of extended states. However, a first extended state is visible in Figures 4.17(c), where the states developing from the potential pits touch and form connecting paths from one side of the image to the other. An upward movement of a drift state onto a potential hill

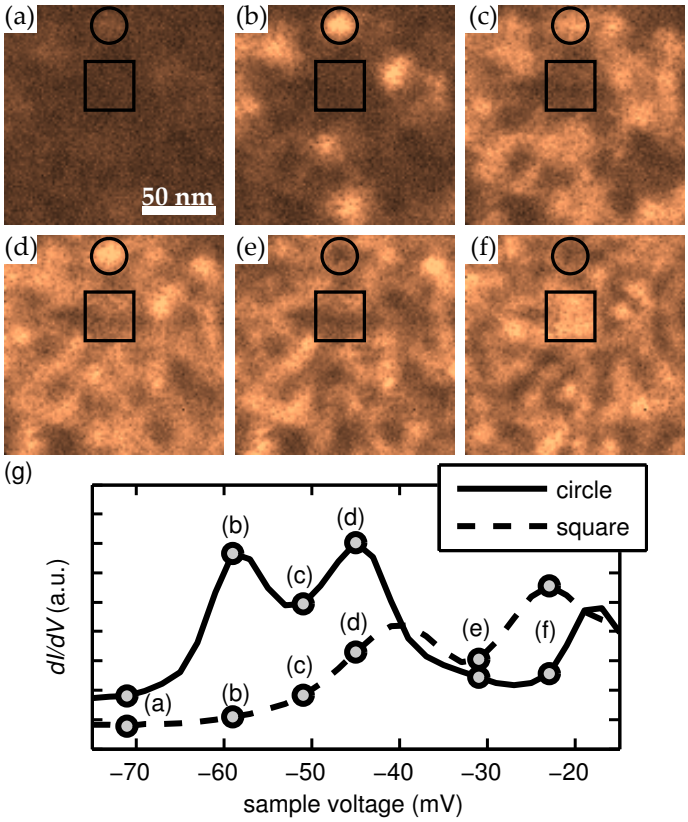

Figure 4.17.: (a)–(f) dI/dV images with 1.5 nm resolution at $B = 7$ T, 150 nm $\times$ 150 nm, $V_{\text{stab}} = 300$ mV, $I_{\text{stab}} = 200$ pA, $V_{\text{mod}} = 1$ mV$_{\text{rms}}$; the corresponding sample voltages are marked in the local dI/dV curves shown in (g); (g) local dI/dV curves spatially averaged over the two small areas marked in the images (a)–(f).

is highlighted in Figure 4.18. The black lines roughly mark the dI/dV intensity of a closed structure, which at low energy surrounds an area of about $(80\text{ nm})^2$. With increasing energy, the dark inner area shrinks continuously condensing towards a small spot in (f). The visibility is disturbed by the overlap with states from other levels. Therefore, as can be seen by the calculated spin levels in Figure 4.18(g), Figure 4.18(a) belongs to about the maximum of the lower spin level ($\uparrow$), while Figures 4.18(b)–(f) belong to the upper part of the higher spin level ($\downarrow$). This leads to reduced overlap with other states in both cases. Indeed, the energetic overlap of states from different Landau and spin levels at different potential energy completely removes the spin splitting from the spatially averaged dI/dV curve, i.e. the DOS, and weakens the visibility of the Landau level splitting significantly, as shown by the upper curve in Figure 4.18(g). The effec-

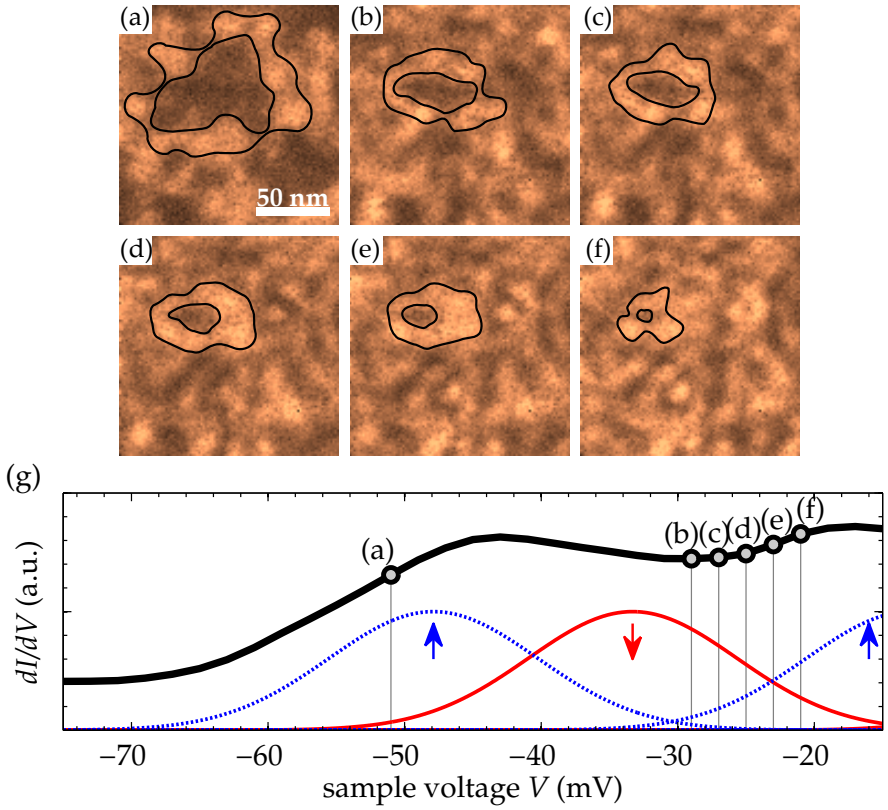

Figure 4.18.: (a)–(f) dI/dV images recorded at $B = 7$ T, $V_{\text{stab}} = 300$ mV, $I_{\text{stab}} = 200$ pA, $V_{\text{mod}} = 1\ \text{mV}_{\text{rms}}$, with different sample voltages as marked in (g), 150 nm × 150 nm; the intensity marked by black lines highlights a drift state moving uphill with increasing energy; (g) Spatially averaged dI/dV spectrum (thick black line) originating from the 10^4 curves covering the whole image area of (a)–(f). The lower peaks are calculated spin levels as indicated by the arrows, using Equation (4.28) with $m^* = 0.022 \times m_0$, $g^* = -31$, and $\alpha = 7 \times 10^{-11}$ eV m, broadened by a Gaussian with full width at half maximum (FWHM) of 18 meV.

tive mass $m^* = 0.022 \times m_0$ effective g-factor $g^* = -31$ used in the calculation of the spin levels in Equation (4.28) correspond to the calculated values at the subband onset. The origin of the chosen Rashba parameter $\alpha = 7 \times 10^{-11}$ eV m is explained in the following section. As mentioned above, a much clearer development of drift states with energy across a single spin split Landau level has been shown in Reference [8].

4.4.4. Rashba effect in the DOS

As described in Section 4.2.3, constant values of m^* and g^* would lead to equally spaced Landau and spin levels at constant B field. Each level is broadened by the disorder potential, which is relatively large in this system because of the high acceptor concentration prohibiting the observation of spin splitting in the spatially averaged density of states. For nonparabolic conduction bands, the Landau level splitting $\hbar\omega_c(E) = \hbar eB/m^*(E)$ and the spin splitting $|g^*(E)|\mu_B B$ both decrease with energy (Section 4.2.2). This fact, however, cannot explain the spatially averaged spectrum shown in Figure 4.9 (upper curve), page 47, which exhibits a beating pattern of the Landau level intensity within the first subband. The proposed explanation for the beating is Rashba spin splitting (Section 4.2.4), which gives a k dependent spin splitting for confined 2D electrons moving perpendicular to an electric field even at $B = 0$ T. The Rashba spin splitting increases with the wave number $|k|$ (Figure 4.3(a), page 39), leading to two dispersion curves with different effective masses. Including this effect into the effective mass Hamiltonian results in Landau levels $E_i^{n',\sigma'}$ given by Equation (4.28):

$$E_i^{n',\sigma'} = E_i + \hbar\omega_c \left(n' + \sigma' \left(\delta^2 + \gamma^2 n' \right)^{1/2} \right), \tag{4.41}$$

$$\gamma = \alpha \left(2m^*/\hbar^3\omega_c \right)^{1/2}, \tag{4.42}$$

$$\delta = \frac{1}{2}\left(1 - \frac{m^* g^*}{2m_0} \right), \tag{4.43}$$

with

$$\sigma' = \begin{cases} 1, & n' = 0 \\ \pm 1, & n' \in \mathbb{N}\,. \end{cases} \tag{4.44}$$

From this it is obvious, that the g-factor induced spin splitting given by δ is the same for all n', while the Rashba parameter α dependent splitting encoded in γ increases with the level index n'. If the value of γ is large enough so that $\delta^2 + \gamma^2 n'$ reaches values larger than 1, this eventually leads to an overlap of spin

states from different n' in the density of states inducing a beating of the DOS as shown in Figure 4.19 with $\gamma = 0.44$.

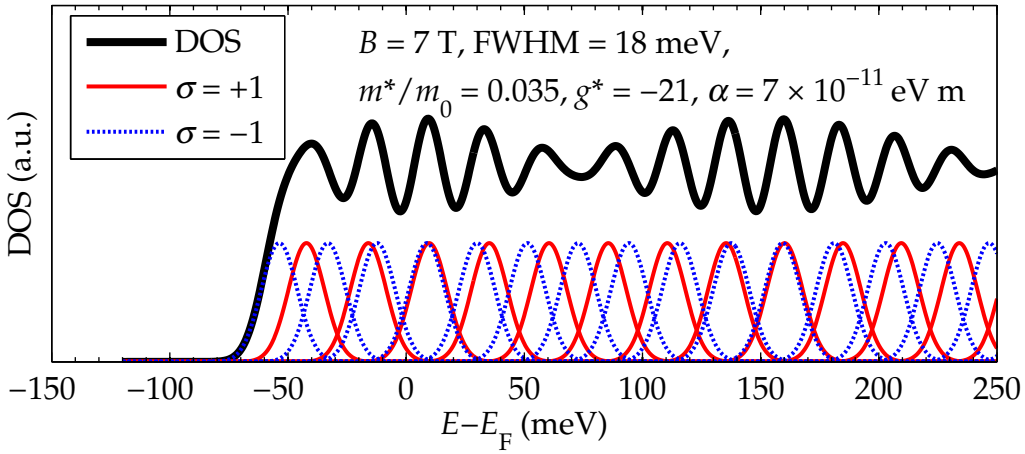

Figure 4.19.: Calculated Landau levels including the Rashba effect according to Equation (4.41) with the indicated parameters for a two-dimensional subband starting 60 meV below E_F. The broadening of each Landau level of the different spin branches $\sigma = \pm 1$ is modelled by a Gaussian with the shown full width at half maximum (FWHM). The DOS curve, being the sum of all Landau levels, shows a beating pattern.

Using Equation (4.27) with the strength of the electric field $|\vec{E}| = 3.1 \times 10^7$ V m^{-1} displayed in Figure 4.8 gives a Rashba parameter of $\alpha = 1.6 \times 10^{-10}$ eV m, which is very large for a semiconductor. Because Equation (4.27) is only a first order approximation in a series expansion for subband energies small compared to the gap energy, which is not the case in this sample, a better result can be estimated numerically using Equations (4.23) and (4.25) with the calculated band bending and the subband wave function. This gives $\alpha = 9$–11×10^{-11} eV m within the uncertainty range of $N_A = 1$–2×10^{24} m^{-3} for this sample, causing slight variations of the confinement potential $V(z)$ and subband wavefunction $\psi_0(z)$ as calculated in Section 4.4.1. The value of α is even higher than observed in InAs inversion layers or heterostructures by transport measurements (3–4 $\times 10^{-11}$ eV m) [80]. It should be noted that the calculated Rashba parameter is an upper estimate, since the ignored effect of barrier penetration of the electronic waves decreases the mean electric field within the electron subband distributions and therefore decreases the effective Rashba parameter. Furthermore, α is only the lowest order of an inversion asymmetry induced spin splitting and it is known that higher orders lead to a reduced ef-

fect [62]. Indeed, the observed beating patterns displayed for different B fields in Figure 4.20 can be reproduced nicely by using Equation (4.41) with a slightly reduced Rashba parameter of $\alpha = 7 \times 10^{-11}$ eV m. For the sake of simplicity, constant effective mass and g-factor were taken as the average value within the first subband ($m^* = 0.035 \times m_0$, $g^* = -21$) and an n' and σ' independent Gaussian broadening was fit to the spin and Landau levels accounting for the potential disorder in order to obtain the calculated curves in Figure 4.20. However, different Gaussian broadenings are used for different B fields to account for the reduced l_B with B according to Equation (4.20). Note that the fit parameter FWHM = 13–18 meV given in Figure 4.20 nicely agrees with the potential disorder that is visible in Figure 4.17.

Although not all details of the measured spectra can be reproduced this way probably in part due to the neglected gradual decrease of m^* and $|g^*|$ due to nonparabolicity, the minima of the beating (nodes), marked by arrows in Figure 4.20, are in excellent agreement with the experiment. The calculation also reproduces the increase of beat frequency with decreasing B field. The decreased FWHM found for lower B reflects the fact that the lateral extension l_n of the drift states scales according to $l_n \propto 1/\sqrt{B}$ [65, 66, 6] (Equation (4.21)). Thus, drift states become more insensitive to the steepest parts of the fluctuating disorder potential at lower B. The chosen FWHMs, however, do not influence the positions of the beating nodes.

The node positions of the Rashba beating vary in the calculation, of course, with the chosen effective mass and effective g-factor. The calculated relative effective mass of the first subband increases from $m^*/m_0 = 0.022$ at the subband edge (E_0, $V = -60$ mV), 0.029 at the Fermi level (E_F, $V = 0$ mV), towards 0.042 at the onset of the second subband (E_1, $V = 110$ mV). The absolute value of the effective g-factor decreases respectively according to Equation (4.16) with $g^* = -31$ at E_0, -24 at E_F, and -16 at E_1.

Figure 4.21 shows different calculated DOSs and their first beating nodes are marked, except for the lowest spectrum with parameters of the subband edge, which does not show a node within this energy range. From this it is evident, that the beating pattern is highly sensitive on these values. A higher effective mass and a lower g-factor reduces the beat interval, so it could be argued that the Rashba parameter may be even lower while still showing a beating within the first subband. However, the chosen parameters seem reasonable, as the values chosen for Figure 4.20 (0.035 and -21) are close to the calculated values for the energy position of the first node, measured at $V = 70$ mV at $B = 7$ T: $m^*/m_0 = 0.037$ and $g^* = -19$. Figure 4.22 compares these values to the other values within the first subband, with a Rashba parameter α fitted to match the beat position at 70 meV. This gives a range for the possible α of

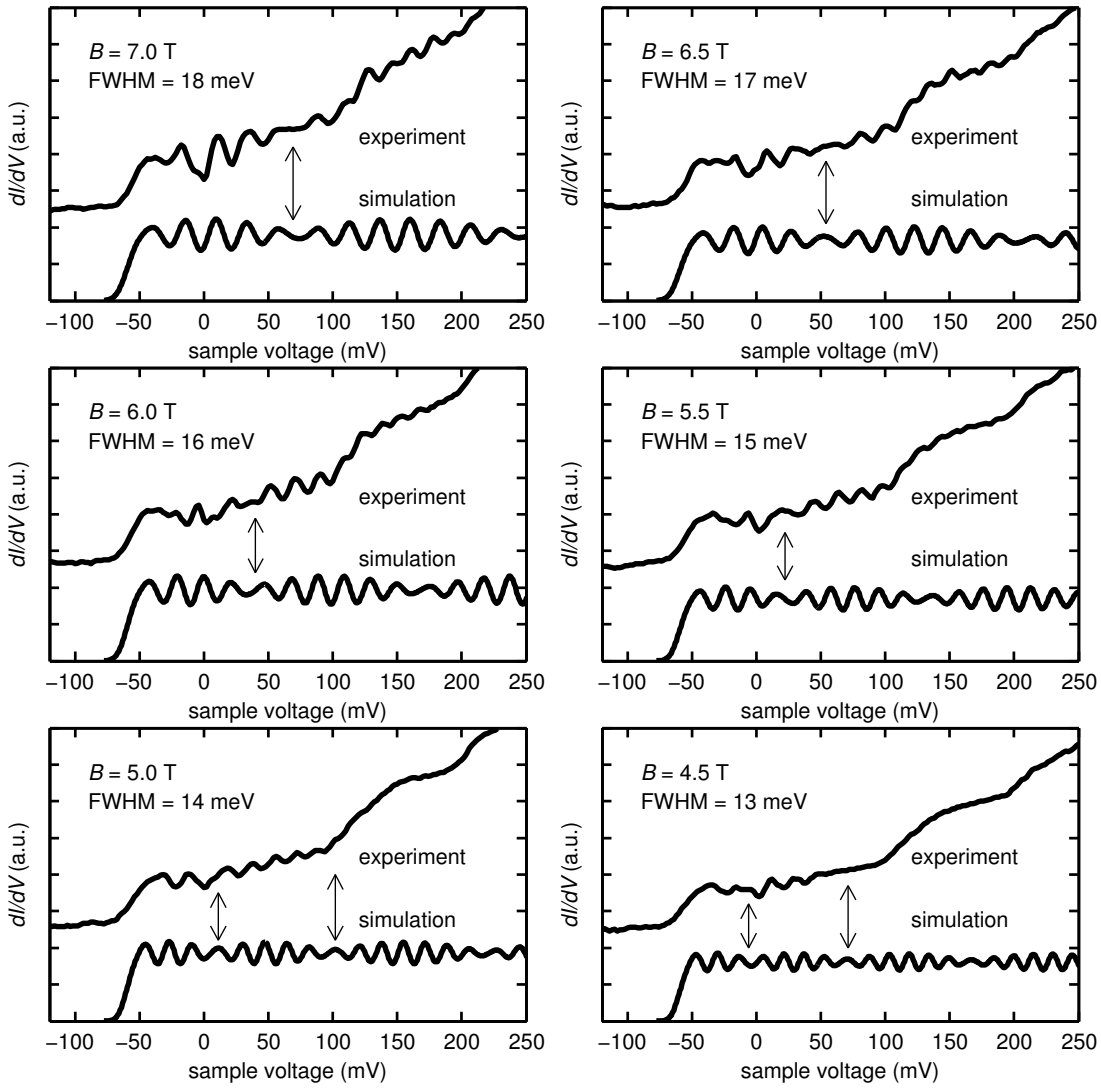

Figure 4.20.: Landau level beating due to the Rashba effect in the density of states. Spatially averaged dI/dV (DOS) spectra at different B fields as marked (experiment) in comparison with simulations using Landau and spin energies from Equation (4.41) with $m^* = 0.035 \times m_0$, $\alpha = 7 \times 10^{-11}$ eV m, $g^* = -21$ and a Gaussian broadening with full width at half maximum (FWHM) as indicated for each B field. The beating minima are marked by arrows.

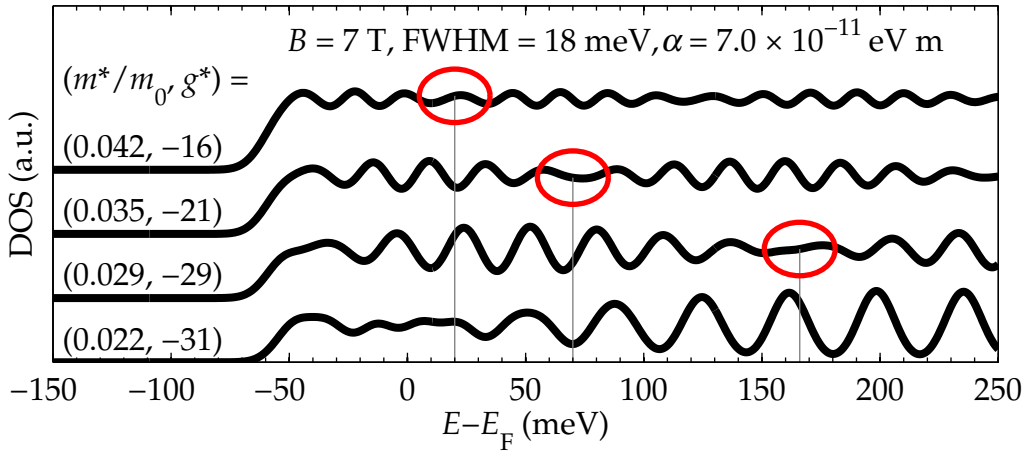

Figure 4.21.: Different calculated DOSs with parameters as indicated (compare Figure 4.19), shifted vertically for visibilty. The circles mark the first beating node of each curve.

5.4–9.0 $\times 10^{-11}$ eV m. Because the linear approximation of the nonparabolicity in Equation (4.15) tends to overestimate the effective mass as discussed above, a value of $\alpha = 7 \times 10^{-11}$ eV m is most reasonable.

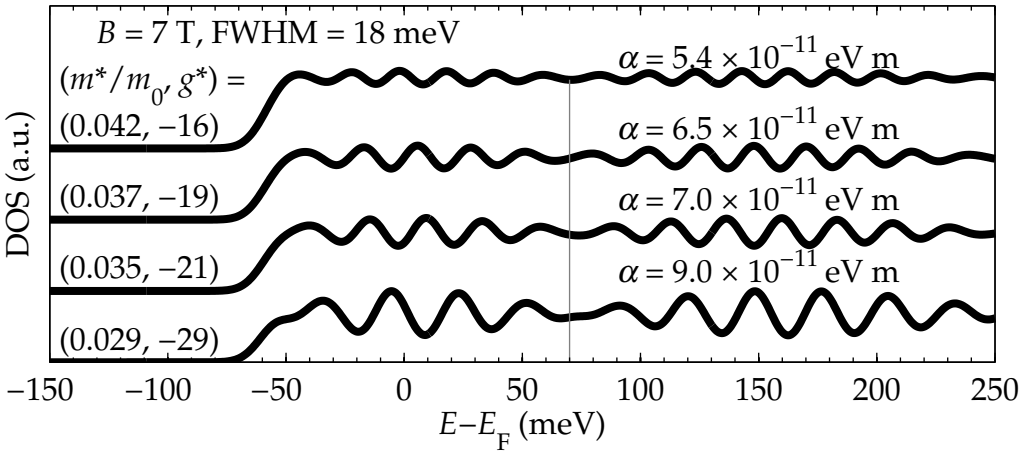

Figure 4.22.: Different calculated DOSs with parameters to match the first beating note at 70 meV as extracted from the experiment for $B = 7$ T.

4.4.5. Rashba spin splitting in the LDOS

The above discussion of the Rashba spin splitting regards the DOS at high magnetic fields. The Rashba spin splitting is, of course, also present at $B = 0$ T and would split an approximated parabolic energy dispersion $E(k)$ into two branches separated by $\pm\alpha k$ [11] if higher order spin splitting terms are neglected. This leads to a spin splitting of about 30 meV around E_F and two k_F values of about $k_- = 2.7 \times 10^8$ m^{-1} and $k_+ = 2.1 \times 10^8$ m^{-1} (compare Figure 4.3(a) on page 39). However, these two k_F values are not visible in the FFT of Figure 4.11 in accordance with theory, because the observed standing wave pattern is generated by interference of backscattered electrons from the same spin branch only [81]. Slight changes within the complex LDOS pattern might appear, if multiple scattering is involved [82], but these changes could only be pinpointed by detailed comparison with LDOS calculations including the details of the disorder potential [74]. Notice that the width of the ring in the FFT of Figure 4.11(a) is as large as the difference of k_+ and k_- at E_F showing that the Rashba effect and the disorder within this sample are of the same strength.

The experimental DOS is gained by spatially averaging many local dI/dV curves. An influence of Rashba spin splitting visible in the DOS at high magnetic fields should therefore also be visible in local spectra. Figure 4.23(a) shows an image of the LDOS at $B = 7$ T and a sample voltage $V = -57$ mV. Bright areas in the image reveal the lowest spin split Landau states in potential minima. Local spectra at the marked positions are shown in (b). Spectra 1, 2 and 3 are all in comparable potential pits and their spectrum is very similar, showing the lowest spin split Landau level around -50 mV and part of the second Landau

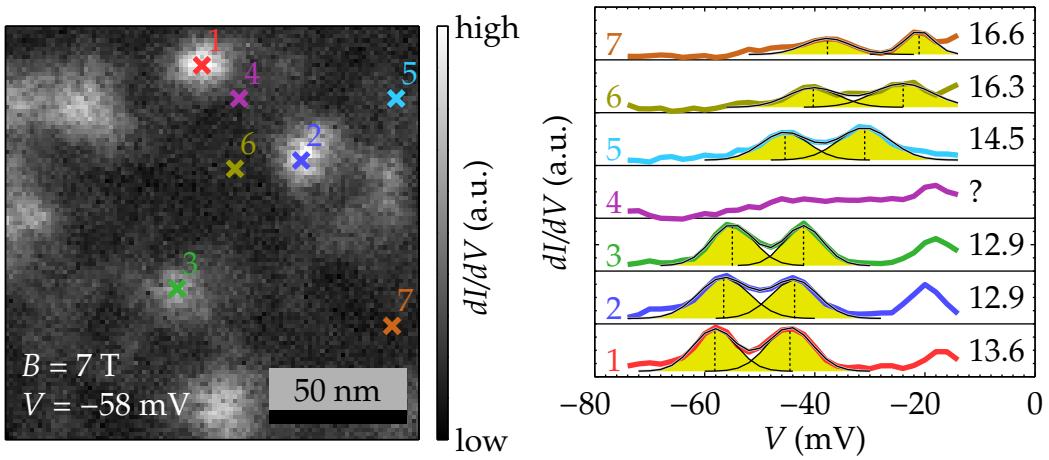

(a) (b)

Figure 4.23.: (a) $dI/dV(x,y)$ image taken at $V = -57$ mV (compare Figure 4.17(b)), $B = 7$ T, 150 nm × 150 nm, $V_{\text{stab}} = 300$ mV, $I_{\text{stab}} = 200$ pA, $V_{\text{mod}} = 1\ \text{mV}_{\text{rms}}$. (b) Local dI/dV measurements at the positions marked in (a), shifted vertically for visibility. Two Gaussians are fit to the first Landau level of each spectrum except for number 4. The values on the right are the corresponding peak separations, representing the spin splitting energies in meV with an error due to the fitting of about 0.2 meV for spectra 1–3 and 0.4 meV for spectra 5–7.

level at −20 mV. The shown spin splitting energies extracted from the peak positions is approximately $E_{ss} = 13$ meV, corresponding to $|g^*| = 32$, which is very close to the calculated value $|g^*| = 31$ without a Rashba effect (Equations (4.15)–(4.17)) as already stated in Section 4.4.3. Due to the narrow energy range of this data showing only the spin splitting of one Landau level, these spectra cannot exhibit a Rashba effect by showing a beating pattern. However, theoretical calculations of Rashba spin–orbit coupling suggest local fluctuations of the Rashba parameter for systems with high potential disorder [83, 84]. The z component of the local electric field fluctuates due to the high acceptor concentration of this sample and therefor the local spin–orbit coupling varies. This should lead to local variations of the observed spin splitting.

Spectra 5–7 of Figure 4.23(b) are taken at dark areas of (a), indicating elevated areas in the potential landscape. The extracted spin splitting energies E_{ss} of these spectra are larger. This is opposite to the expected behavior due to the nonparabolicity of InSb. At increased energy, the effective g-factor should be smaller and thus the spin splitting should be reduced. The extracted E_{ss} of more single spectra are shown in Figure 4.24, plotted against the peak position of the first spin level. The mean spin splitting of the evaluated spectra in the bright

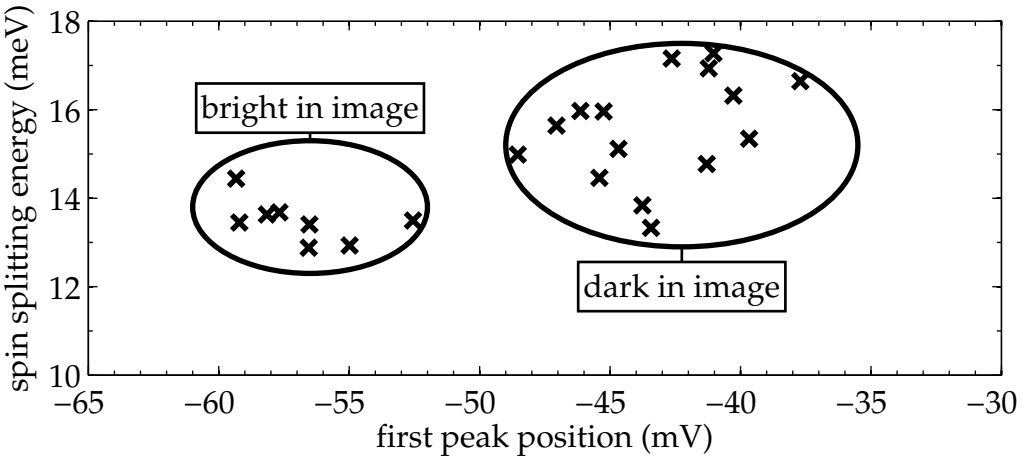

Figure 4.24.: 23 extracted local spin splitting energies of the first Landau level as shown in Figure 4.23 against the position of the first spin level. Low first peak positions appear bright in Figure 4.23(a), indicating potential pits.

potential pits of Figure 4.23(a) is (13.5 ± 0.5) meV while the spin splitting in the darker areas is higher and has a higher standard deviation with (15.6 ± 1.2) meV. Moreover, in the bright areas the spin splitting varies by 1.5 meV in an interval of 2.7 mV (12.9 meV at −56.6 mV and 14.4 meV at −59.3 mV), while

in the dark areas the measured extrema vary by 4.0 meV in an interval of only 2.4 mV (13.3 meV at −43.4 mV and 17.3 meV at −41.0 mV). The fit errors of generally less than 0.5 meV cannot explain these differences. Equation (4.28) can be used to relate these variations to the Rashba parameter α, encoded in γ:

$$\begin{aligned} E_{\mathrm{ss}} &= \left| E_0^{1,-1} - E_0^{0,+1} \right| \\ &= \hbar\omega_{\mathrm{c}} \left| 1 - \left(\delta^2 + \gamma^2 \right)^{1/2} - |\delta| \right| \\ &= \hbar\omega_{\mathrm{c}} \left| 1 - \left(\delta^2 + \alpha^2 \frac{2m^*}{\hbar^3 \omega_{\mathrm{c}}} \right)^{1/2} - |\delta| \right| \end{aligned} \tag{4.45}$$

Using fixed values for $m^* = 0.022 \times m_0$ and $g^* = -31$, corresponding to the calculated values at the subband onset, $E_{\mathrm{ss}}(\alpha)$ is shown in Figure 4.25. The measured variations of E_{ss} translate to variations of α between 3 and

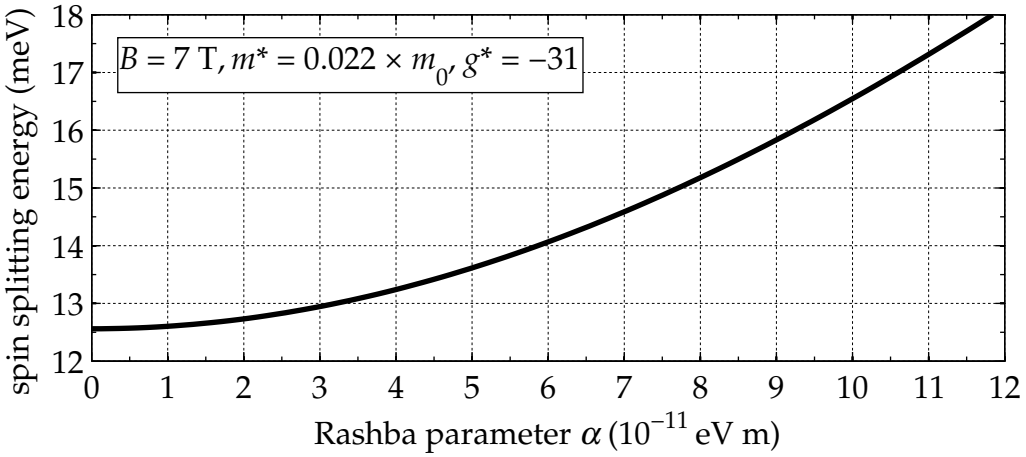

Figure 4.25.: Estimated Rashba parameter α dependent spin splitting energy E_{ss} of the first Landau level by using Equation (4.28) with the calculated values $m^* = 0.022 \times m_0$ and $g^* = -31$.

11×10^{-11} eV m. The latter is exactly the theoretically estimated maximum value for the Rashba parameter in Section 4.4.4. The larger spin splitting around potential maxima might be related to the larger acceptor concentration within these areas leading to a steeper potential gradient in z and a higher potential in (x, y) at the same time. Indeed, variations of the spin splitting on the meV scale are expected due to fluctuations of the electric field by a simple model calculation. These variations are gained by assuming a random distribution of the charged acceptors, similar to the simulations of the potential disorder in

Figures 4.15 and 4.16, although the exact values do not yet agree with the observation.

For the model calculations, the bulk acceptor concentration $N_A = 1 \times 10^{24}$ m^{-3} is used to distribute acceptors randomly over a large area, meaning a multiple of the observed area, and down to the depth of the depletion length. This leads to local fluctuations of the acceptor concentration. Taking an area of $(30\text{ nm})^2$, corresponding to the observed length scale of the potential disorder, these fluctions are between 0.4×10^{24} m^{-3} and 1.9×10^{24} m^{-3}. Using these values in the band bending calculation discussed above results in a Rashba parameter of $\alpha = 7\text{–}11 \times 10^{-11}$ eV m. According to Equation (4.45) and Figure 4.25, this translates to a spin splitting of the first subband between 14.6 meV and 17.3 meV. While the maximum is in nice agreement with the experiment, the total range of the spin splitting in the experiment 70 % larger. However, the performed calculations overestimate the Rashba parameter as discussed in Section 4.4.4, and the uncertainty range of the bulk acceptor concentration $N_A = 1\text{–}2 \times 10^{24}$ m^{-3} is quite large as well. Although this calculation cannot reproduce the exact range of spin splittings yet, it is likely that the observed spin splitting variations can quantitatively be explained by random Rashba fields [84] caused by random dopant distribution. To achieve this, the contributing parameters have to be controlled more exactly.

However, in the experiment the spin splitting could not be resolved at all positions of the sample surface. Especially at intermediate potential, Gaussian fits cannot be applied as can be seen for example in spectrum 4 of Figure 4.23. Also it is not clear why the spectra at higher potential areas (5–7) show peaks with notable differences in height and width. Usually two spin states of the same Landau level at the same local positions have the same shape, as the peaks in 1–3 or those of the second sample discussed in the following sections. In order to explain these unknowns, future measurements are necessary with higher energy resolution and dI/dV spectra over the whole energy range of the first subband. Local variations of a beating pattern similar to Section 4.4.4 are expected. The existing experimental data strongly suggests these large local fluctuations of the Rashba parameter.

4.5. 2DES in low doped *p*-InSb(110)

In this section the 2DES on a low doped sample is discussed (sample II of Table 4.1), that has a more flat band bending at the same surface doping conditions as the highly doped sample. The sample has been prepared by adsorption of 1.1 % of cesium per surface unit cell onto the clean *p*-InSb(110) surface.

4.5.1. Band bending profile and potential disorder

The acceptor concentration $N_A = 1.1 \times 10^{21}$ m^{-3} of this sample is orders of magnitude lower than the typical electron concentration of an inversion layer. Therefore unlike for the previous sample the inversion layer electrons cannot be neglected in a band bending calculation and the solution is no simple inverted parabola. The Poisson equation is solved using the 3D bulk density of states according to Equation (4.7) (Section 4.2.1) with an energy dependent effective mass to account for the nonparabolicity of the InSb conduction band (Section 4.2.2). This results in the band bending shown in Figure 4.26(a) with an inversion layer electron concentration of $N_s = 2.7 \times 10^{16}$ m^{-2}.

The subband positions E_i, $i \in \mathbb{N}_0$, as marked in Figure 4.26(a) by horizontal lines are calculated within the triangular well approximation (Section 4.2.1). The density of subbands above the Fermi level is relatively large because of the flat band bending at a depth z beyond the inversion layer, where only the acceptor density can screen the electric field.

The band bending reaches deep into the bulk leading to a decoupling of the confined states of the 2DES from the partly empty bulk valence band. E.g., the valence band crosses E_F only 600 nm below the surface prohibiting tunneling from the occupied 2DES states reaching down to 100 nm below the surface to empty valence band states. In fact, the spatially averaged dI/dV curve (I) of Figure 4.26(b), measured without contacting the 2DES directly, does not exhibit any signature of the 2DES, but only an increase in dI/dV close to the onset of the bulk conduction band (+200 mV) and the surface valence band (−400 mV). The tunneling current from the 2DES to the bulk valence band is blocked. This is in contrast to the measurements shown in Section 4.4 on highly doped p-InSb and previously performed measurements using highly doped p-InAs [30] or n-type samples [55, 8, 72], always exhibiting a step like increase in spatially averaged dI/dV curves close to the calculated E_i. If the 2DES is additionally contacted by an Ag stripe running perpendicular to the cleavage plane ([85], Section 4.3.2), it exhibits two steps at about $E_0 = -130$ meV and $E_1 = -50$ meV, which is to the calculated values, as visible in curve (II) of Figure 4.26(b).

The 2D electron concentrations of the first two subbands are $N_0 = 1.3 \times 10^{16}$ m^{-2} and $N_1 = 0.7 \times 10^{16}$ m^{-2}. Their electron distributions along z are plotted enlarged in Figure 4.27. From these distributions, the mean depth of the subband electrons below the surface is deduced to be 7.9 nm for the first subband and 15.2 nm for the second subband.

In a magnetic field $B = 7$ T perpendicular to the 2DES the measured DOS in curve (III) of Figure 4.26(b) shows peaks corresponding to the Landau and spin levels of the 2DES. This already shows that the disorder of this sample is significantly lower than that of the first sample. Also the pattern is fairly

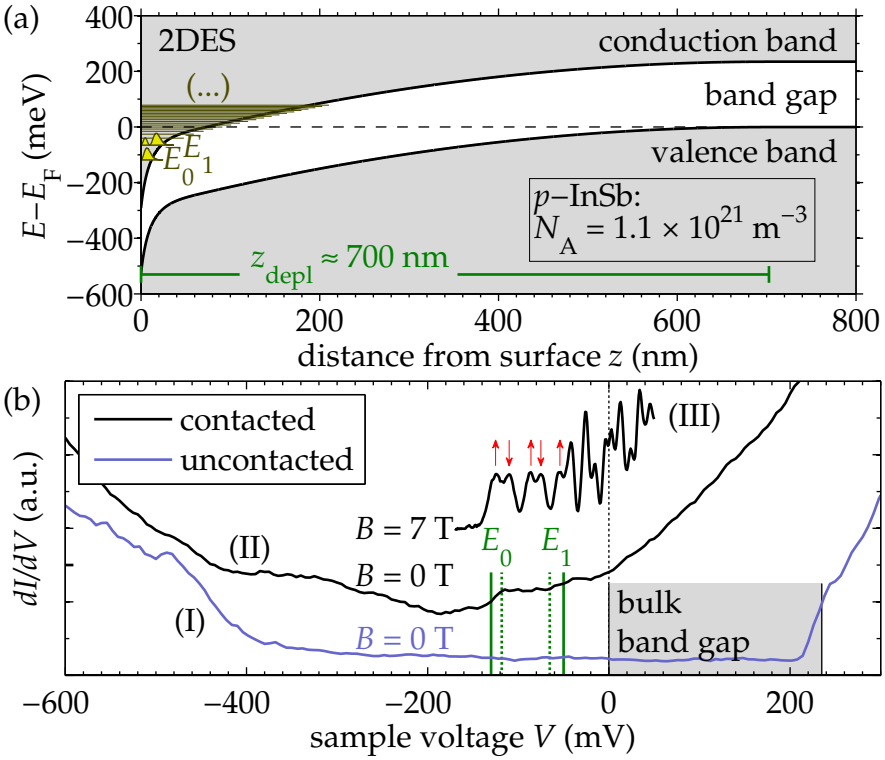

Figure 4.26.: (a) Calculated band bending due to cesium adsorption; first two 2D subband energies $E_0 = -118$ meV, $E_1 = -65$ meV as calculated using the triangular well approximation are marked and the corresponding electron distributions $|\psi_i(z)|^2$ are drawn, shown enlarged in Figure 4.27; other subbands are only indicated by horizontal lines at the subband energies. (b) Spatially averaged dI/dV curves across an area A_{Av}: (I): without contacted 2DES, (II), (III): with contacted 2DES at $B = 0$ T, 7 T as marked; gray area: bulk band gap of p-InSb [58]; E_0, E_1: subband energies from experiment (solid) and calculation (broken lines); arrows in (III) mark spin split Landau levels. (I) $V_{stab} = 400$ mV, $I_{stab} = 100$ pA, $V_{mod} = 1$ mV$_{rms}$, $A_{Av} = 200 \times 160$ nm^2; (II) $V_{stab} = 300$ mV, $I_{stab} = 50$ pA, $V_{mod} = 3$ mV$_{rms}$, $A_{Av} = 100 \times 100$ nm^2; (III) $V_{stab} = 300$ mV, $I_{stab} = 200$ pA, $V_{mod} = 0.4$ mV$_{rms}$, $A_{Av} = 300 \times 300$ nm^2.

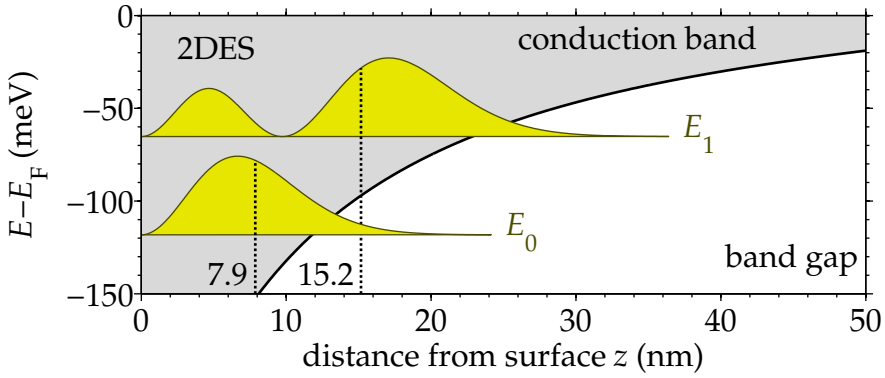

Figure 4.27.: Zoom of Figure 4.26(a): Calculated band bending (black line) and the first two 2D subbands with their electron distribution curves $|\psi_i(z)|^2$ (yellow areas). The mean depths $\langle z \rangle$ of each distribution is indicated by the dotted lines and marked in nm.

regular within the energy range below the second subband, which implies no major additional spin splitting due to the Rashba effect here. The mean electric field for the first subband can be estimated to $|\vec{E_0}| = 1.2 \times 10^7$ V/m, almost a third of the field in the first sample. The calculation of the Rashba parameter gives just $\alpha = 4.1 \times 10^{-11}$ eV m. Notice that the calculated values are higher than the real ones due to the extension of the states into the vacuum (compare Section 4.4.4). An observable beating of the DOS intensity due to the Rashba effect as discussed in Section 4.4.4 is not expected with the parameters of this sample as is shown in Figure 4.28.

The Landau peaks in the spatially averaged dI/dV measurement at $B = 7$ T can be fit with Gaussians. Because the level degeneracy is known (Section 4.2.3) this allows a rescaling of the data to an approximate absolute scale for the DOS as shown in Figure 4.29. The spin splitting for the first Landau level can be extracted from the fits to 16.7 meV $= |g^*|\mu_B B$, giving an effective Landé g-factor of $|g^*| = 41$. The mean difference of the first two Landau levels give an effective mass of $m^* = (\hbar e B)/(37 \text{ meV}) = 0.022 \times m_0$ (m_0: free electron mass). These values (sample II) are shown in Table 4.2 in comparison with the known low temperature values for InSb at the conduction band minimum, values from the first sample and from previous STS measurements on n-InSb [8]. The increase of m^* and decrease of $|g^*|$ compared to the values at the band edge can be explained by the nonparabolicity of InSb. The experimental g-factor in this sample is larger than expected from Equation (4.16) in relation with the experimental effective mass. The measured effective mass of sample II is also about the same as that of sample I, although the calculation expects a smaller effective mass

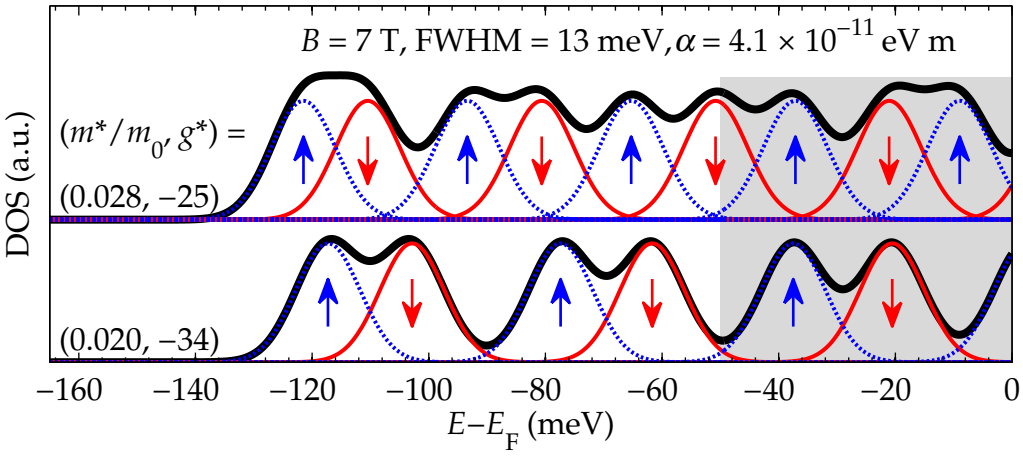

Figure 4.28.: Different calculated DOSs with parameters as indicated, (compare Figure 4.19), shifted vertically for visibilty. The different spin levels are indicated by arrows. The parameters of the lower DOS corresponds to the calculated values at the onset of the first subband. The upper curve uses m^* and g^* corresponding to values at the onset of the second subband. The shaded area marks the energy range of the second subband, where a beating in the first subband cannot be distinguished from a superposition of Landau levels from different subbands.

for sample II, because here the subband is closer to the conduction band edge. However, the values of sample I do not represent averaged values for the whole sample surface. They could only be extracted locally in potential minima due to the large potential disorder and the corresponding overlap of different Landau levels. The values for n-InSb are also extracted from a local measurements only, but here the potential disorder is much smaller and so not much variation due to different subband positions relative to the conduction band edge is expected. The values for sample II and for the n-InSb measurement are in good agreement.

The full width at half maximum (FWHM) of the fits in Figure 4.29 decreases with Landau level index n, being 16.0 mV for $n = 0$, 12.7 mV for $n = 1$ and 12.1 mV for the first spin level of $n = 2$. This effect is due to the decreased sensitivity of the Landau level drift states to the potential landscape, which can only probe potential fluctuations down to the length scales of their different lateral extentions (Equation (4.21)). Single spot dI/dV spectra only show a width of about 11 mV for $n = 0$. From this, the width of the potential disorder can be estimated to $\Delta_{\mathrm{dis}} \simeq \sqrt{16^2 - 11^2}$ meV $= 12$ meV. This is lower than the disorder

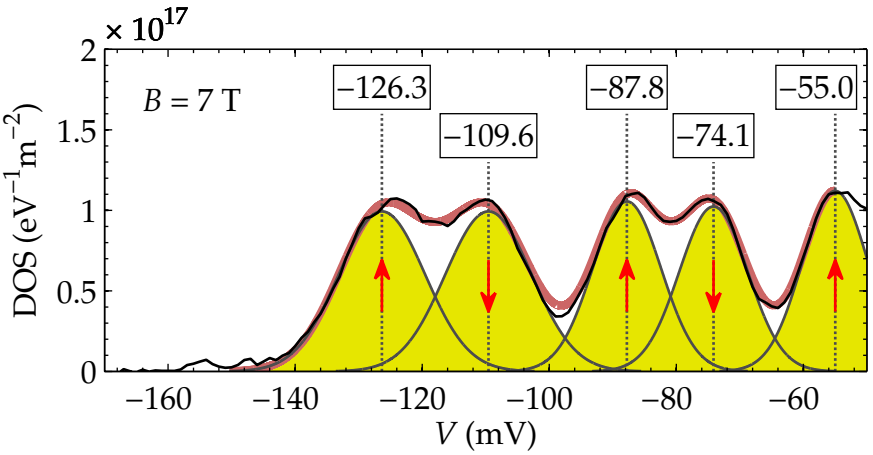

Figure 4.29.: Spatially averaged dI/dV curve (black line) at $B = 7$ T, $V_{\mathrm{stab}} = 300$ mV, $I_{\mathrm{stab}} = 200$ pA, $V_{\mathrm{mod}} = 0.4$ mV$_{\mathrm{rms}}$, $A_{\mathrm{Av}} = 300$ nm $\times$ 300 nm, 20×20 spectra; yellow areas show the individual Gaussian fit curves of the spin split Landau levels marked by arrows each; red line marks the resulting fit of the dI/dV curve gained by adding up the Gaussians; peak energies of the Gaussians are labeled above each peak in meV.

of about 20 meV of the first sample and comparable to a previously analyzed 2DES prepared by Cs coverage on n-InSb(110) with $\Delta_{\mathrm{dis}} \simeq 10$–$15$ meV [8].

Taking a spatially resolved dI/dV image at a voltage corresponding to the onset of the first Landau level highlights the lateral distribution of the potential disorder in Figure 4.30. As at the onset of a Landau level the electron states form at potential pits, high dI/dV intensity exhibits the potential minima. There are roughly 40 local potential minima within the imaged area, giving an average distance d of $\sqrt{(300\,\mathrm{nm})^2/40} \simeq 50$ nm in accordance with visual inspection.

The experimental disorder potential is more complex than would be expected by an estimate of the involved acceptors. Taking an extension of the first subband of $\simeq 15$ nm into the bulk from Figure 4.29 and $N_{\mathrm{A}} = 1.1 \times 10^{21}$ m^{-3} this gives only 1.5 acceptors within the image area. There are obviously more point charges present (about 50). N_{A} has been determined by Hall measurements giving only the surplus of acceptors over compensating, unwanted donor atoms, so it may actually be replaced with $(N_{\mathrm{A}} - N_{\mathrm{D}})$. As the performed band bending calculations and the following discussions are not changed by this fact, the distinction is not made in this work.

	Experimental		Calculated	
	m^*/m_0	$\lvert g^*\rvert$	m^*/m_0	$\lvert g^*\rvert$
band edge [58, 59]	0.0135 ± 0.0015	51 ± 1	–	–
Sample I	0.020 ± 0.001	32 ± 2	0.022	31
Sample II	0.022 ± 0.001	41 ± 2	0.020	34
***n*-InSb** [8]	0.019 ± 0.001	39 ± 2	0.020	34

Table 4.2.: Low temperature values for the effective electron mass and effective g-factor in InSb. The theoretical values for *n*-InSb, being identical to those of Sample II, have been calculated using Equations (4.15) and (4.16) with the subband position given in Reference [8].

4.5.2. Spreading resistance

The electrical decoupling of the 2DES from the bulk valence band requires the tunneling electrons to move through the 2DES layer between the tunneling entry point and the side electrode of the crystal in an STM experiment. Under normal tunneling conditions and without magnetic field, this change of the electron path has no effect on the measurement. The Landau quantization in a strong perpendicular magnetic field on the other hand leads to localization of the electrons and a reduced in-plane conductivity of the 2DES [65]. This leads to a peculiar dependence of the Landau level dI/dV spectra on the initial stabilizing tunneling parameters.

Figure 4.31(a) shows single point dI/dV spectra as intensity plots measured at exactly the same lateral position, with different magnetic fields B as marked, and with different stabilizing current I_{stab}. For $B = 0$ T, increasing I_{stab} does not change the dI/dV spectra. With increasing magnetic field Landau levels appear as pairs of lines and with increasing I_{stab} the Landau levels spread away from zero sample voltage V. At 7 T, the observed spin splitting of the lowest Landau level is increased by 13 % and the Landau level distance is increased by 18 %.

This effect can be attributed to the reduced in-plane conductivity at high magnetic fields. Part of the applied voltage drops across the 2DES and not across the tunneling gap between tip and sample. A higher tunneling current I increases this so-called spreading resistance of the electrons since an increasing amount of charge accumulates in the 2DES region below the tip, if the charge flow occurs through hopping conductance [28] as typical in quantum Hall samples. This hopping conductance is illustrated in Figure 4.32(a) in one dimension. Localized electrons in potential minima of the potential landscape have a finite probability to hop over a potential barrier in any direction. An applied voltage shifts the potential landscape and hopping in the charge flow direction is favored by a decreased barrier height. Because the hopping process is slow,

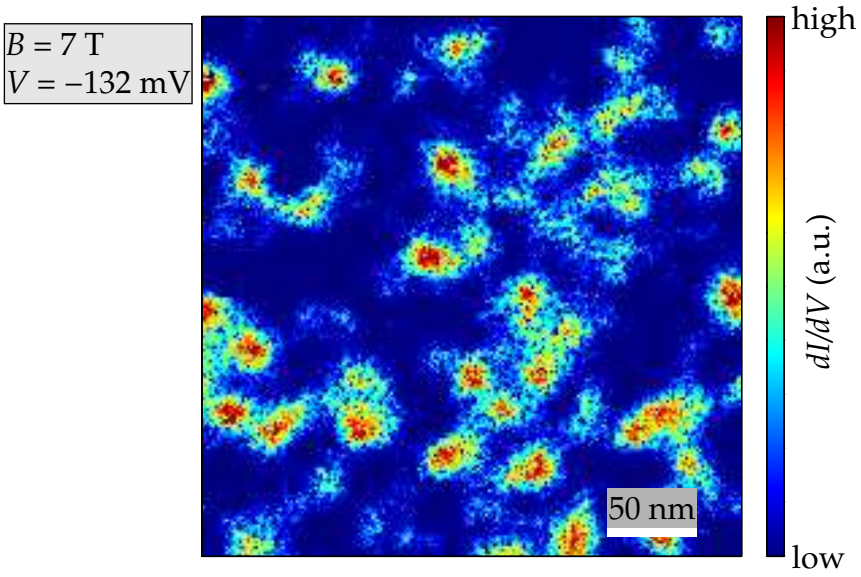

Figure 4.30.: $dI/dV(x,y)$ image at $V = -132$ mV and $B = 7$ T, $V_{\mathrm{stab}} = 300$ mV, $I_{\mathrm{stab}} = 200$ pA, $V_{\mathrm{mod}} = 1.6$ mV$_{\mathrm{rms}}$, 300 nm $\times$ 300 nm. High dI/dV intensity marks potential pits.

more charges accumulate with increasing current I. This increases the potential difference for a given current nonlinearily. The two-dimensional hopping model includes, that the current density $\vec{j}$ decreases with distance from the entry point, corresponding to the tip position in the experiment, as sketched in Figure 4.32(b).

The observed spreading in the experiment can be quantitatively reproduced using hopping barrier heights given by the potential disorder $\Delta_{\mathrm{dis}} \approx 12$ meV of Section 4.5.1, next-neighbor distances of valleys $d \approx 50$ nm as determined by spatially resolved measurements in Figure 4.30, and by assuming a reasonable attempt frequency of $\nu_0 = 10^{13}$ Hz. Figure 4.31(b) shows fit calculations, performed by Marcus Liebmann [86], of the first spin split Landau level positions at $B = 7$ T against the actual tunneling current I within the parameters of the spreading restance model in excellent agreement. This strongly supports the assumption that the current indeed flows along the 2DES exhibiting reduced conductivity with increasing B.

For the explanation by spreading resistance to be trusted without going too much into the model details, other possibilities should be excluded, namely a tip induced band bending (Stark effect) [87, 70]. The idea is that with a closer tip, the lever arm of the bias voltage increases. The lever arm L describes the amount of additional band bending $\Delta\Phi(V)$ due to the varying potential differ-

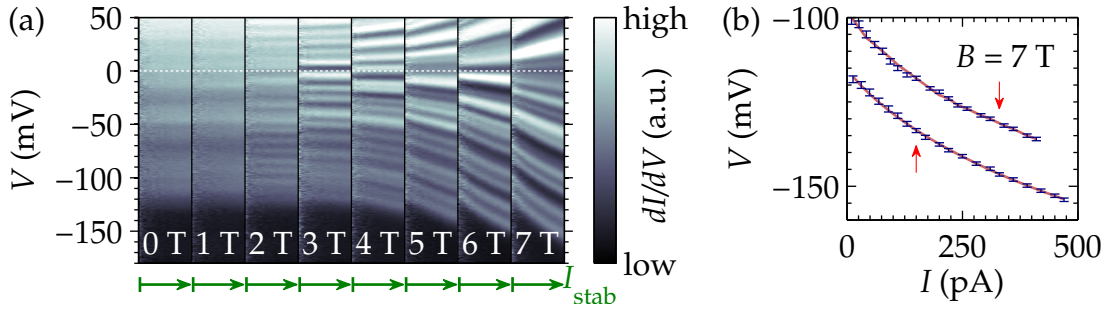

Figure 4.31.: (a) dI/dV spectra (colored intensity plot) recorded at the same lateral position at different B fields as indicated. I_{stab} is increased for each B from 100 pA to 2000 pA (left to right). $V_{\text{stab}} = 300$ mV, $V_{\text{mod}} = 1.6$ mV$_{\text{rms}}$. (b) Measured lowest Landau level positions (spin up ↑; spin down ↓) against the actual tunneling current I at $B = 7$ T (symbols) in comparison with calculated Landau level positions (line) [86].

ence between tip and surface (see e.g. [8]) related to the applied voltage V:

$$L := \frac{\Delta\Phi(V)}{eV}. \tag{4.46}$$

Without magnetic field the two-dimensional electrons are not localized and are efficient at screening the bias voltage. With increasing magnetic field the electrons localize and the screening becomes less effective, resulting in the observed stretching of the Landau levels in the dI/dV spectra. The band bending calculations described in Section 4.2.1 are therefore extended by a cesium layer, a vacuum barrier and a metallic STM tip.

The cesium layer is modeled at the surface $z = 0$ with the known adsorbate concentration $N_{\text{Cs}} = 3.7 \times 10^{16}$ m^{-2} and estimated charge concentration $N_{\text{s}} = 2.7 \times 10^{16}$ m^{-2}. As the potential at the surface changes, this layer is charged or uncharged to allow a pinning of the Fermi energy at the band bending energy. This charging stops when all atoms are charged or discharged.

To model the lever arm in the vacuum barrier $z < 0$ the absolute distance of the STM tip to the surface is needed at each stabilizing current. This can be estimated by fitting $I(z)$ measurements to an exponential tunneling decay and extrapolating the $z = 0$ offset to the quantum of conductance $G_0 = 2e^2/h$ with electron charge e and Planck's constant h [88]. From this the estimated tip distance is about 800 pm at $I_{\text{stab}} = 100$ pA and 600 pm at $I_{\text{stab}} = 2$ nA.

As input the model further requires the potential of the tip relative to that of the surface entry point. The experiment shows that the Landau level energies spread out symmetrically from zero sample bias. For an explanation of

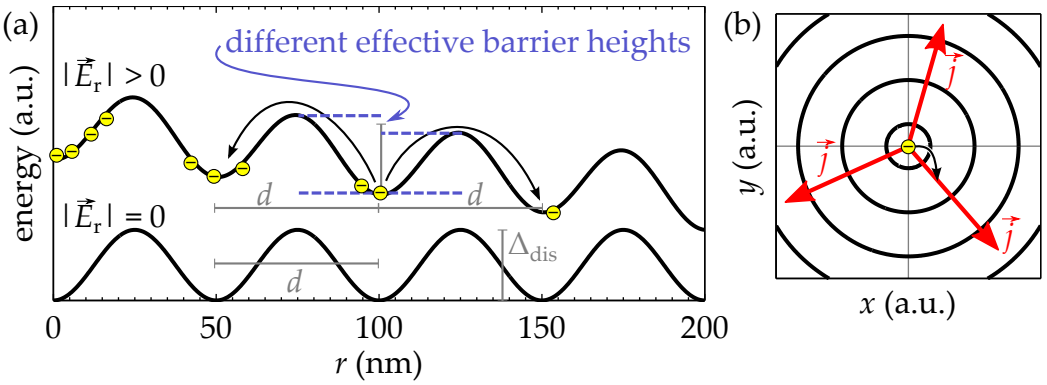

Figure 4.32.: (a) Sketch of one-dimensional hopping conductance. The lower curve shows a regular effective electron potential without an electric field, with potential differences of Δ_{Dis} and distance of the potential minima d. The upper curve shows the modified potential with an additional electric field $\vec{E}_r$, which increases with current I due to additional accumulating charges. (b) Sketch of the spreading of the hopping conductance in 2D. The current density $\vec{j}$ becomes smaller with distance r from the center, representing the position of the STM tip.

the spreading by tip induced band bending this implies that the work function mismatch of tip and surface is negligible. This by itself is improbable but possible. The potential of the tip is therefore set to that at the surface of the sample without a tip.

At zero magnetic field there is no spreading observable within the noise of the measurement. At $B = 7$ T the lowest spin Landau level is measured at about $V = -117$ mV with $I_{stab} = 100$ pA and at $V_{sample} = -154$ mV with $I_{stab} = 2$ nA. Reduced screening therefore needs to account for a difference in observed Landau level or subband onset position of 37 meV.

Using the model without any reduced screening, the subband energy, being at $E_0 - E_F = -118$ meV without the presence of a tip, should match the applied bias voltage at -186 meV and -178 meV for the different extreme tip positions at 600 pm and 800 pm respectively. These energies are lower than observed in Figure 4.31(a) at $B = 0$ T. Thus, this one-dimensional calculation already overestimates the lever arm of the tip, but the difference of 8 meV is still well below the observed value at $B = 7$ T.

The reduced screening by localization of the electrons is simulated by partially freezing the inversion layer electron distribution i.e. letting only part of the electrons from the bulk density of states screen the change of potential. Then

the lever arm increases for both tip distances, increasing the lever arm difference as well.

The problem with this model is that the lever arm itself increases too fast for the relative lever arm to result in an energy shift of 37 meV. E.g. when freezing 90 % of the electrons in InSb, the observed subband onsets would be at -339 meV and -356 meV for the two extreme tip positions, showing a relative difference of only 17 meV. In contrast, the experiment does not show any significant increase of the onset energy of the 2DES at $I_{\text{stab}} = 100$ pA. The conclusion is that tip induced band bending cannot account for the observed spreading effect, giving additional evidence for the hopping model described above.

4.5.3. Landau fan and exchange enhancement

The 2DES of this sample fullfills all requirements to exhibit electron–electron interaction effects: The 2DES is occupied, the two-dimensional electrons are decoupled from the bulk electrons, exhibit an independent Fermi level, and the center of mass of the first subband is 8 nm below the surface, about 9 nm away from the metallic tip which is sufficient to prevent complete screening. One such electron–electron inferaction effect is the exchange enhancement of the spin splitting in a perpendicular magnetic field, which is rather short-ranged, since it requires overlap of electron states.

InSb has a large effective g-factor so the Landau levels of this system are split by Zeeman spin splitting. Therefore, unless the filling factor ν (Section 4.2.3) is even, the 2DES has a net spin. The effective repulsion between electrons is smaller for electrons with parallel than for antiparallel spins. Consequently, an electron state with $\uparrow$-spin has higher Coulomb energy than an electron with $\downarrow$-spin, if the majority of electrons exhibit $\downarrow$-spin. This leads to a higher spin splitting than only by Zeeman splitting, in all cases, except if the filling factor is even and, thus, the same amount of $\uparrow$ and $\downarrow$ electrons are present. The highest spin splitting is observed at odd filling factor, i.e. when the spin polarization of the electrons is largest. This results in an enhancement of the spin splitting that is oscillating with the filling factor [23, 24].

In order to measure the oscillating enhancement, the filling factor has to be varied. ν solely depends upon the subband electron density N_i and the magnetic field B (Equation (4.19)). Without adding a gate electrode to modify the confinement potential, which is likely to change mulitple properties of the band bending profile and the subband at the same time, B can be changed continously.

Single point dI/dV spectra, measured repeatedly at a fixed position while ramping the magnetic field, are shown in Figure 4.33(a). This plot is called a

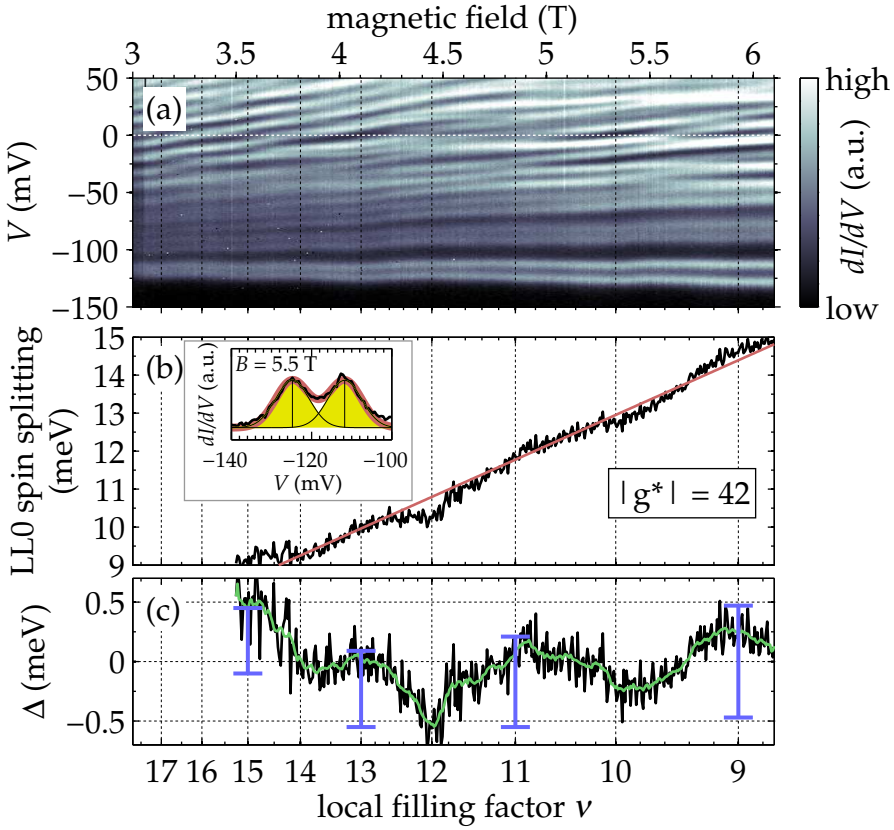

Figure 4.33.: (a) Landau fan showing dI/dV as intensity plot; B field is ramped downwards continuosly, $V_{\mathrm{stab}} = 300$ mV, $I_{\mathrm{stab}} = 400$ pA, $V_{\mathrm{mod}} = 1.6$ mV$_{\mathrm{rms}}$. (b) Spin splitting energy E_{ss} of lowest Landau level extracted by Gaussian fits as shown in the inset. Straight line marks $E_{\mathrm{ss}} = |g^*|\mu_{\mathrm{B}}B$. (c) Deviation Δ from the linear fit in (b). The inner bright line is smoothed. Vertical bars show the calculated values of exchange enhancement between neighboring odd and even filling factors. Local filling factors $\nu \propto 1/B$ are matched by counting spin levels below E_{F} (compare Figure 4.35(a)) and verifying their B dependence.

Landau fan, because it shows the (spin split) Landau levels fanning out with the magnetic field as can be expected by the linear expression in B of Equation (4.17). While less than 10 % of the fanning is caused by spreading resistance, additional effects besides exchange enhancement are responsible for the deviation of the plot from straight lines. Most noticable is the parallel, wavy motion of the Landau levels in the lower part of the plot, corresponding to the Landau levels of the first subband only. Responsible for this is the shift of the Fermi level E_F with the magnetic field while the level degeneracy increases. With increasing degeneracy, E_F, corresponding to zero sample voltage, moves contiously through each Landau level while at the same time the level splitting increases. Once E_F favors a transition from a higher Landau level to the next lower one, all Landau levels move upward with respect to E_F. As long as E_F stays within a certain Landau level, all levels below E_F, move downwards with respect to E_F due to the increasing Landau level separation. At the same time, all levels above E_F move continously upwards. The whole measured spectrum below E_F, thus, oscillates in with B. At energies above -50 meV, this motion is present but less visible, because here the measurement is a superposition of multiple subbands. The first subband still gives the highest contrast.

Less noticable is an oscillation of the spin splitting energies E_{ss} due to exchange enhancement. While in theory Landau levels closer to E_F show the largest exchange enhancement, in this measurement E_{ss} can better be extracted from the lowest subband around -120 mV, due to the missing overlap with other Landau levels from other subbands. Moreover, the lowest Level gives the best signal at this local position.

For all 386 spectra between 3.5 and 6.1 T two Gaussians with equal width and height are fitted to the lowest Landau level using a nonlinear least squares method and a trust-region algorithm as implemented in Matlab[2]. The fits are generally good as can be seen in the inset of Figure 4.33(b) and by the confidence value of $R^2 = 0.94$ (0.97 above 5 T). The error bar for the resulting E_{ss} is about 0.2 meV.

$E_{ss}(B)$ is shown in Figure 4.33(b). The straight line represents ordinary Zeeman splitting of $|g^*|\mu_B B$ with $|g^*| = 42$. Here an oscillatory behavior is already visible. To highlight this, the deviation $\Delta(B)$ from the straight line in (b) is shown in (c). The inner line of the experimental data represents a simple smooth for better visibility. $\Delta(B)$ oscillates around 0 meV with local maxima and minima around odd and even filling factors as expected for exchange enhancement. The filling factor is deduced by counting the number of peaks below the Fermi level within an individual spectrum. Thus, it is the local filling factor, which determines the exchange enhancement as expected from the short-range character

[2]MathWorks Curve Fitting Toolbox V2.1 User's Guide

of the exchange interaction.

The curves in Figures 4.33(b) and (c) are influenced by additional effects changing the apparent spin splitting with B. The nonparabolicity of InSb leads to a smooth decrease of g^* with increasing B, while the beforementioned spreading resistance streches the levels, increasing the observed splitting. The spreading resistance may even oscillate with the filling factor, as the density of states changes at the Fermi level, but this effect would lead to the largest spreading at even filling factors, where energy gaps are largest. This is just opposite to the exchange enhancement and the observed oscillation. This effect might explain, why $\Delta(B)$ in (c) shows positive and negative deviations of the spin splitting given by $|g^*|\mu_B B$, while exchange enhancement would only explain positive ones. Of course, the deviations change if g^* is modified, but no fit through all local minima at even filling factors can be made in (b), that would show pure exchange enhancement.

To substantiate the results, theoretical estimates of the exchange enhancement in this sample system for the lowest Landau level were obtained in a parameter-free calculation, performed by C. Karrasch and V. Meden using the well-justified random phase approximation (RPA) [24, 89, 90].[3] The length of the vertical bars in Figure 4.33(c) represent the resulting values at odd fillings. The measured oscillation amplitude of about 0.7 meV is in excellent agreement with the calculated enhancement between 0.55 meV and 0.94 meV. In combination with the correct filling factor dependence, exchange enhancement is, to our knowledge, the sole convincing explanation for the shown oscillations. This shows, that a short-ranged electron–electron interaction effect can be probed by STS within the quantum Hall regime.

4.5.4. Coulomb gap in the DOS

Systems where electrons are localized, as in this 2DES in the quantum Hall regime, are expected to show a so-called *Coulomb gap* at the Fermi level in the density of states [91, 27, 92]. It describes a vanishing DOS value at E_F and a characteristic shape of a suppression close to E_F. The theoretical argument for a Coulomb gap can be made by assuming a system with a finite DOS value at E_F. This means an electron of the system can be excited by an arbitrarily small energy portion δE into an unoccupied state. In a localized electron system this excitation generates an electron–hole pair, separated in space by a distance r. Without screening by nearby metallic gate electrodes, it has a Coulomb energy E_C proportional to $1/r$, and E_C can only be smaller than δE. Now if δE becomes infinitesimally small, so does E_C, and r must become infinitely large, which is

[3] For details see supplementary information of Reference [90]

just not possible. Thus, obviously, the suppression of the DOS at E_F is caused by the long-ranged Coulomb interaction.

The exact shape of the suppression region is quite complex to investigate and results are controversial [92, 93]. A first and probably most simple estimate gives a linear, V-shaped Coulomb gap for an unscreened 2DES at $T = 0$ K [27, 92]:

$$D_0(E) = \frac{2}{\pi}\frac{(4\pi\varepsilon_0\varepsilon_r)^2}{e^4}|E - E_F|, \quad |E - E_F| \leq E_{CG}. \tag{4.47}$$

In this model, the width of the gap region $2E_{CG}$ is defined by the value of the DOS at E_F without a Coulomb gap, the unperturbed DOS. Previous tunneling and transport experiments without lateral resolution are compatible with a linear Coulomb gap [94, 95, 96, 97].

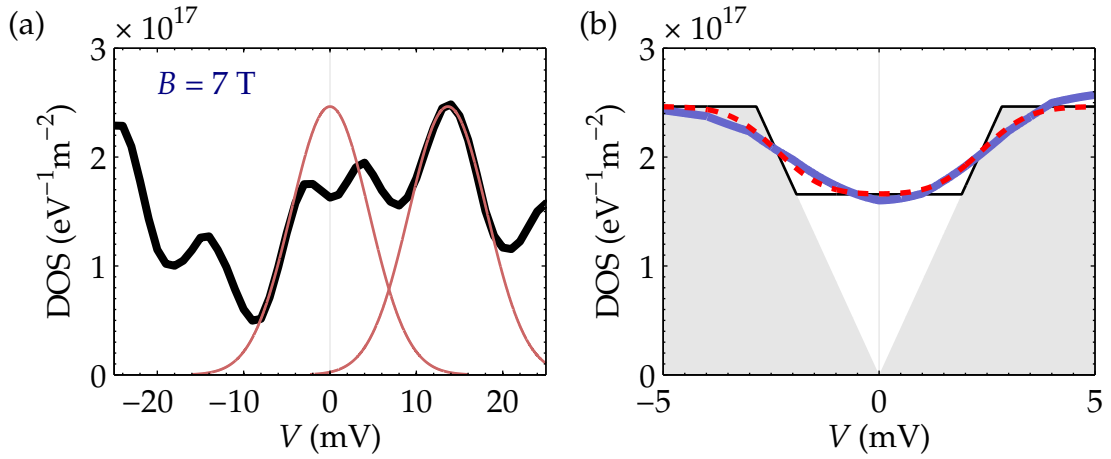

Figure 4.34.: (a) Zoom of Figure 4.26(b)(III) (thick line). Two Gaussian fits for the Landau level at E_F (thin lines) are added. The absolute scale of the DOS is deduced by fitting the lowest spin split Landau level to a two-peak Gaussian (see Figure 4.29) and matching the integral of one Gaussian to the known level degeneracy $eB/(2\pi\hbar)$. (b) The shaded area shows the expected bare Coulomb gap of Equation (4.47) (V-shaped gap) with the maximum DOS value 2.46 $eV^{-1}m^{-2}$ of the fitted Gaussians. The Coulomb gap taking finite temperature and screening into account is shown as thin black line, and the red dashed line shows this gap including the energy resolution. The thick blue line shows the difference between measured curve and the two Gaussians in (a), shifted by the maximum DOS value of the expected gap.

The experimental DOS of my experiment near the Fermi level at $B = 7$ T

is shown in Figure 4.34(a) as a thick line. The absolute DOS scale has been estimated as previously explained for Figure 4.29 in Section 4.5.1. The measured DOS does not show a vanishing intensity at E_F, but a small dip. Without a Coulomb gap there should be a peak at E_F corresponding to a half integer filling factor $\nu = 8.5$ of the 2DES, as can be easily deduced from the whole spectrum in Figure 4.26(b)(III). The double peak is then compared with a Gaussian fit similar to the fits in Figure 4.29. Thus, the peak width and height are taken from the next peak above E_F by a Gaussian fit. Superimposing it onto the DOS centered at $V = 0$ mV (thin red line) fits the tail region of the assumed Landau level very well. The Gaussian serves as the DOS not perturbed by electron–electron interaction. By taking the difference of experimental and unperturbed DOS, the Landau level characteristics caused by single-particle effects are removed, leading to the blue line in Figure 4.34(b), plotted with an offset corresponding to the maximum DOS value of the fitted Gaussian of 2.46 $\mathrm{eV}^{-1}\mathrm{m}^{-2}$. This exhibits the actual suppression of the DOS. A V-shaped Coulomb gap estimated with Equation (4.47) is shown as shaded area in the plot.

An observation of a Coulomb gap is, of course, broadened by the energy resolution and finite temperature of the experiment. Moreover, the metallic STM tip does have screening properties. Screening limits the expected minimum DOS value, which has been estimated to [92]:

$$D_{\mathrm{mod}}(E_F) \approx 0.085\frac{4\pi\varepsilon_0\varepsilon_r}{e^2 d} + 0.86\frac{(4\pi\varepsilon_0\varepsilon_r)^2 k_B T}{e^4} \tag{4.48}$$

with d being the distance of a metallic gate to the center of the 2DES. Here, d is estimated as the distance of the STM tip to the mean depth of the first subband. With 7.9 nm as mean depth of the 2DES to the surface from Figure 4.27 and an additional 700 pm at $I_{\mathrm{stab}} = 400$ pA by $I(z)$ measurements as described in Section 4.5.2, d is taken as 8.6 nm. With $T = 5$ K and $\varepsilon_r = 16.8$ [98] this gives

$$D_{\mathrm{mod}}(E_F) = 1.66 \times 10^{17}\ \mathrm{eV}^{-1}\mathrm{m}^{-2}. \tag{4.49}$$

As an approximation, the V-shaped Coulomb gap of Equation (4.47) is simply cut at this value:

$$D(E) = \max\left[D_0(E), D_{\mathrm{mod}}(E_F)\right]. \tag{4.50}$$

This gap shape is shown in Figure 4.34(b) as thin black line. Finally the shape is broadened by the energy resolution during this measurement $\Delta E = 1.6$ meV according to Equation (2.9) ($V_{\mathrm{mod}} = 0.4\ \mathrm{mV_{rms}}$) by folding $D(E)$ with a Gaussian numerically. The result, plotted in Figure 4.34(b) as red dashed curve, is in excellent agreement with the measured dip.

The assumption of a Coulomb gap reproduces the experimental observation very well. It is consistent with numerical studies, that the Coulomb gap can

be observed even around the critical (extended) state, i.e., close to half integer filling of a spin-polarized Landau level as in this measurement [99]. Inelastic excitations may produce similar symmetric suppressions of the DOS at the Fermi level, but all commonly known effects would have much larger gap widths: 22 meV for optical phonons (transversal: 22 meV, longitudinal: 24 meV), 60 meV for plasmons and 18 meV for spin excitations at $B = 7$ T. Additionally the suppression is not observed without localization at $B = 0$ T (see Figure 4.26(b), curve II). These facts all strongly suggest that the observed dip is indeed caused by the Coulomb gap. Notice that a slight suppression of DOS intensity at E_F is also observed for the sample with higher doping in Figure 4.20, which becomes most evident by comparison with the Rashba type calculations.

4.5.5. Coulomb gap in the LDOS at varied B

The theoretical descriptions of the Coulomb gap necessarily describe the spatially averaged DOS. Surprisingly, the Coulomb gap can also be observed in the local DOS (LDOS). As the single particle Landau levels in a 2DES have discrete energies, broadened in the experiment by disorder [100] and energy resolution, there is no shape prediction of a local spectrum for a system with a Coulomb gap.

A way to observe the influence of the Coulomb gap on local spectra is shown by the analysis of a measurement at fixed tip position and varied magnetic field B, which shifts individual states through E_F. Figure 4.35(a) shows single dI/dV curves at increasing magnetic field as indicated. The corresponding filling factors ν are between 10 and 9 as is easily verified by a counting of the peaks. Following the tenth spin level, marked by the upper (red) arrows, one can see that the peak is clearly visible at $\nu = 10$ and $\nu = 9$ while it is being suppressed as it crosses the Fermi level. At $\nu = 9.5$ ($B = 5.62$ T), where the state should be directly at the Fermi level, the peak is not distinguishable from the surrounding spectrum at all. A similar suppression of intensity with minimum at $V = 0$ mV is also observed for a minimum between Landau levels, marked by the lower (green) arrows. The dI/dV values and voltage positions of the marked state and minimum extracted from all spectra of Figure 4.33(a) taken in the selected B range are shown in Figure 4.35(b), making the suppression by the Coulomb gap visible. The dashed line marks the zero offset of the 2DES in the measurement. At this particular position, the observed suppression of the peak is even greater (48 %) than the averaged Coulomb suppression in the DOS (33 %). More suprisingly, individual states seem to be suppressed at E_F, in contrast to the state counting argument typically used to explain the Coulomb gap [99, 92, 93].

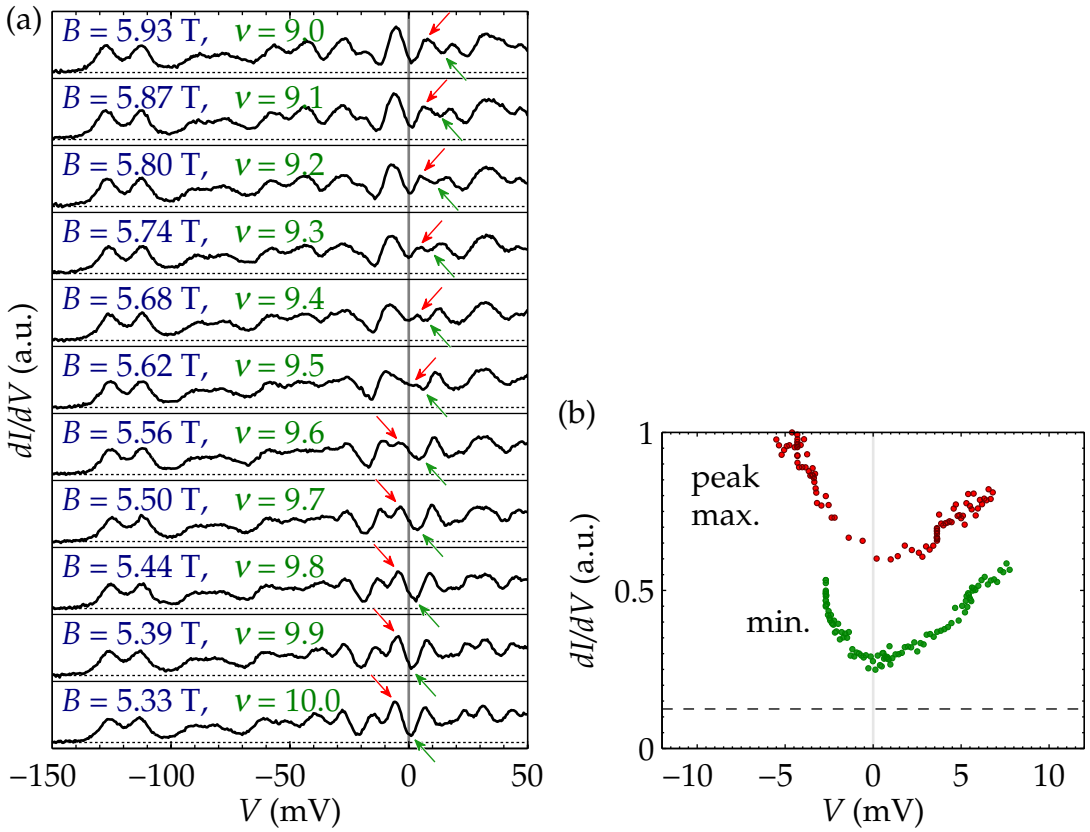

Figure 4.35.: (a) dI/dV spectra taken at the same position at the indicated B fields. Arrows of same color follow the same peak or minimum across E_F. (b) dI/dV value of the marked peak and minimum in (a) as a function of voltage.

4.5.6. Coulomb gap in the LDOS within the potential landscape

The shift of a state across the Fermi level has been realized by increasing the level separation with the magnetic field. Different local filling factors and positions of filled levels with respect to E_F can also be observed by changing the position within the potential landscape.

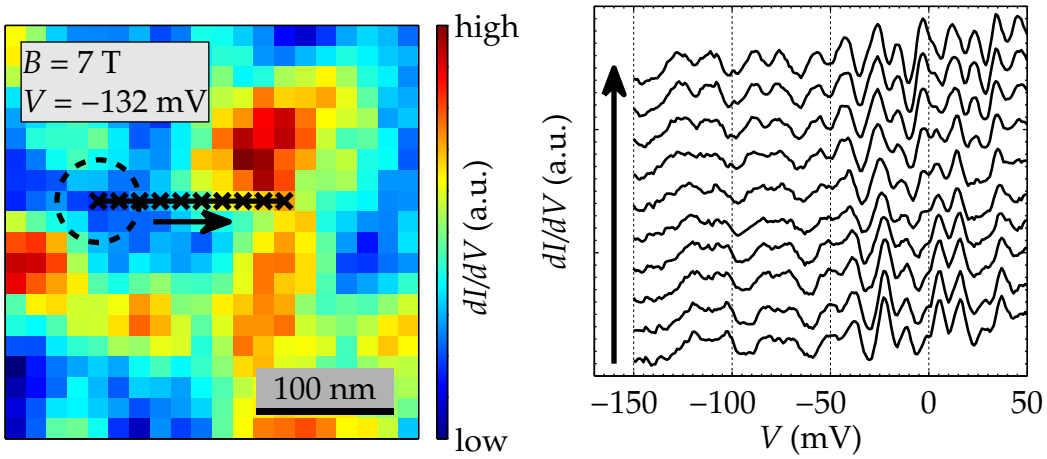

Figure 4.36.: (a) Local measurements of the Coulomb gap. $dI/dV(x,y)$ image at $V = -132$ mV and $B = 7$ T; the data belong to the spatially averaged dI/dV curve in Fig. 1(b)(III) of the main article; $V_{stab} = 300$ mV, $I_{stab} = 200$ pA, $V_{mod} = 0.4$ mV_{rms}, 300 nm $\times$ 300 nm, 20×20 spectra. High dI/dV intensity marks potential pits as in Figure 4.30. The crosses and the arrow mark the positions and the sequence of the spectra shown in (b). 12 next neighboring spectra have been averaged for each spectrum in order to reduce noise. This leads to a spatial resolution of 60 nm as indicated by the circle. (b) dI/dV spectra recorded at different positions as marked in (a). The spectra are offset vertically. The Coulomb gap is visible as a dip or kink pinned at $V = 0$ mV (E_F). Note that all other features except the Coulomb gap feature shift continuously due to the varying potential.

Figure 4.36 shows the spatially resolved measurement corresponding to the spatially averaged DOS analyzed in Figure 4.34(a). Figure 4.36(a) shows the dI/dV image at $V = -132$ mV, corresponding to the onset of the first Landau level of the sample. It therefore represents the potential landscape as already shown in Figure 4.30 with higher spatial resolution at a different position. In Figure 4.36(a), the lateral resolution has been smoothed by averaging 12 next

neighboring spectra, leaving a resolution of 60 nm as indicated by the circle in (a). (b) shows the full spectra corresponding to the marked positions in (a), shifted vertically along the direction of the arrow.

Moving down in the potential landscape as indicated by the arrow, the lowest four Landau levels of the first subband shift to lower energies more or less in parallel as expected. The changes of the remaining spectrum are more complex as the dominating contrast of the first subband is disturbed by higher subbands. Most importantly though, the peak close to E_F shifts through E_F continously while showing distinct suppression of intensity exactly at E_F. The suppression is visible as a small dip if the state is directly at E_F or as kinks in the tails of peak in the remaining spectra. Notice, that this state crosses E_F around the middle of the line drawn in Figure 4.36(a), corresponding to about the mean of the potential disorder. This gives additional evidence, that the global filling factor in this measurement is indeed at half filling. Consequently, the suppression of intensity in the spatially averaged spectrum of Figure 4.34(a) is indeed of a single peak at E_F, that should be observed in the single particle DOS.

The plot in Figure 4.36(b) illustrates again the local observation of a Coulomb gap feature, not predicted by simple qualitative arguments. The physical reason for this observation is not clear, but it might be that current induced dynamics of the electron occupation around the tunneling tip mimics a spatial averaging or disorder averaging. This would explain the surprisingly large peak widths in local spectra ($\Delta E_{\mathrm{meas}} \approx 11\,\mathrm{meV} \gg \Delta E \approx \sqrt{3k_BT + 2.5V_{\mathrm{mod}}} \simeq 2\,\mathrm{meV}$) as well as the observation of a local Coulomb gap.

5. Summary

In this work the design of a UHV-STM system for measurements at 300 mK and 14 T has been presented. Care has been taken to allow stable measurements by several stages of vibrational insulation of the STM: a placement of the system inside of an anechoic room, an optimized rigid support frame, two air damping stages, and a compact STM body design. Several standard sample and STM tip preparation methods are available within the UHV chamber system, including sample heaters, an ion sputter gun, a LEED/Auger system, a mass spectrometer, and several positions for material evaporators.

Using a UHV-STM system operating at 5 K, two different inversion layer 2DESs have been prepared on the *p*-InSb(110) surface by Cs adsorption. The band bending and subband energies of both systems agree well with theoretical estimates. The highly doped sample exhibits a steep band bending with one occupied subband only. STS images show the evolution of standing waves in the 2DES, being dominated by wave numbers explained by a nonparabolic dispersion relation, but exhibiting strong wave function mixing and large corrugation due to disorder. In a magnetic field, Landau and spin levels are observed locally, but washed out in the DOS due to the disorder with amplitudes of about 20 meV. Percolating drift states are observed within the potential landscape. The DOS shows an irregular Landau level pattern dominated by beating which is attributed to Rashba spin splitting caused by the asymmetry of the confining potential. The deduced Rashba parameter of $\alpha = 7 \times 10^{-11}$ eV m is relatively large and very close to the value of $\alpha = 9$–11×10^{-11} eV m estimated by $\mathbf{k} \cdot \mathbf{p}$ theory. This shows that Rashba parameters can also be determined by a local probe, which provides spatial resolution down to the atomic scale. Local data of the spin splitting of the first Landau level indicates a strong fluctuation of the Rashba parameter due to the disorder potential, which should be an interesting topic worth studying in future high-resolution measurements.

The band bending of the low doped *p*-type InSb crystal is significantly more flat, leading to more than one occupied two-dimensional subband on the one hand, but on the other these subbands are fully decoupled from the bulk electron system more than 600 nm apart. This blocks the tunneling current through the band gap to the back electrode of the crystal and requires an additional side electrode, forcing the current through the two-dimensional layer. At high

tunneling currents within the quantum Hall regime this leads to a peculiar spreading resistance effect, increasing the Landau level splitting up to about 15 %. The spreading is qualitatively reproduced by a next-nearest neighbor hopping model, but not by tip induced band bending. The magnitude of the disorder potential with amplitudes of 12 meV is considerably smaller than in the highly doped system and the spin splitting can be resolved in the DOS. In magnetic field dependent local measurements, an exchange enhancement of the spin splitting of about 0.7 meV at $B = 6$ T is found in quantitative agreement with parameter-free calculations within a well justified theory [90]. At the Fermi level a suppression by 30 % of the DOS is observed at fixed magnetic field (7 T), that can be attributed to the Coulomb gap, originating from the long-range part of the Coulomb repulsion. The width of the gap of about 6 meV is very well reproduced by estimates based on qualitative arguments including thermal broadening and remaining screening of the metallic STM tip. In local STS measurements, the Coulomb gap is also revealed by a suppression of Landau states, crossing the Fermi level due to the ramped external magnetic field. The Coulomb gap can additionally be identified at fixed magnetic field in local curves, where a state is, by chance, located at E_F. For the LDOS, no well-developed theory predicting a Coulomb gap exists so far. Future measurements, especially containing more spatially resolved data recorded at higher energy resolution as in experiments at 300 mK, should be able to resolve this puzzle. It is nevertheless shown that low temperature STS is able to detect electron–electron interaction in quantum Hall samples down to a resolution below all relevant length scales.

A. List of used symbols

Symbol	Description
$\mathrm{Ai}(x)$	Airy function of the first kind
B	magnetic field
$D(E)$	energy dependent two-dimensional density of states
e	elementary charge
$\vec{E}(z)$	electric field below the surface
$\lvert\vec{E}_i\rvert$	strength of the average electric field for subband i
$E(k)$	energy dispersion
$E^{\sigma}(k)$	Rashba spin split energy dispersion
E_{F}	Fermi level
E_{g}	Band gap energy
E_i	subband energy
E_{ss}	spin splitting energy
$E^{n}_{i,\sigma}$	Landau level energy
$E_i^{n',\sigma'}$	Landau level energy including Rashba spin splitting
g^*	effective Landé g-factor
g_0^*	effective Landé g-factor at the conduction band edge
$\hbar$	reduced Planck constant
i	subband level ($\in \mathbb{N}_0$)
I	tunneling current
I_{stab}	stabilizing tunneling current prior to dI/dV measurements
k	wave number
k_{F}	length of the Fermi wave vector
k_+, k_-	length of the Fermi wave vector of different Rashba spin branches
l_{B}	magnetic length
l_n	Landau level lateral extension
m_0	free electron mass
m^*	effective electron mass
m_0^*	effective electron mass at the conduction band edge
n	Landau level

n'	Landau level with Rashba spin splitting (alternate counting)
N_A	acceptor density
N_Cs	cesium adsorbate density
N_D	donator density
N_i	subband density
N_s	total inversion layer density
T	temperature
V	sample voltage
V_bb	maximum band bending energy due to surface doping
V_mod	modulation voltage during dI/dV measurements
V_stab	stabilizing sample voltage prior to dI/dV measurements
$V(z)$	confinement potential energy
z_depl	depletion depth
α	spin-orbit coupling parameter
Δ	valence band spin-orbit splitting energy
ε_0	electric constant
ε_r	dielectric constant
μ_B	Bohr magneton
ν	filling factor
$\rho(z)$	electron charge density distribution
σ	spin level
σ'	spin level with Rashba spin splitting (alternate counting)
$\phi(z)$	electric potential
$\psi_i(z)$	normalized subband probability density function
ω_c	cyclotron frequency

Table A.1.: List of symbols used throughout the document

B. Properties of InSb

Description	Symbol	Value
Band gap ($T = 0$ K) [58]	E_g	235 meV
effective electron mass at the conduction band edge ($T = 0$ K) [58]	m_0^*	$0.0135 \times m_0$
dielectric constant [98]	ε_r	16.8
effective Landé g-factor ($T \approx 1$ K) [59]	g_0^*	-51
valence band spin-orbit splitting energy ($T = 4$ K) [59]	Δ	0.8 eV

Table B.1.: Properties of InSb and corresponding symbols used

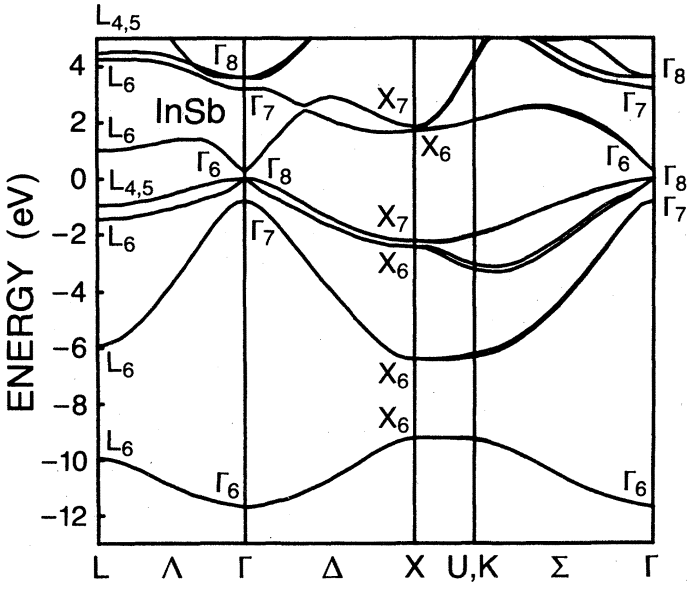

Figure B.1.: Band structure of InSb (from [101]).

Bibliography

[1] G. Binnig, H. Rohrer, Ch. Gerber, and E. Weibel. Surface Studies by Scanning Tunneling Microscopy. *Phys. Rev. Lett.*, 49(1):57–61, 1982. doi: 10.1103/PhysRevLett.49.57.

[2] Roland Wiesendanger. *Scanning Probe Microscopy and Spectroscopy: Methods and Applications*. Cambridge University Press, 1994. ISBN 0521428475.

[3] M. F. Crommie, C. P. Lutz, and D. M. Eigler. Imaging standing waves in a two-dimensional electron gas. *Nature*, 363:524, 1993. doi: 10.1038/363524a0.

[4] Ali Yazdani, B. A. Jones, C. P. Lutz, M. F. Crommie, and D. M. Eigler. Probing the Local Effects of Magnetic Impurities on Superconductivity. *Science*, 275:1767, 1997. doi: 10.1126/science.275.5307.1767.

[5] V. Madhavan, W. Chen, T. Jamneala, M. F. Crommie, and N. S. Wingreen. Tunneling into a Single Magnetic Atom: Spectroscopic Evidence of the Kondo Resonance. *Science*, 280:567, 1998. doi: 10.1126/science.280.5363.567.

[6] M. Morgenstern, J. Klijn, Chr. Meyer, and R. Wiesendanger. Real-space observation of drift states in a two-dimensional electron system at high magnetic fields. *Phys. Rev. Lett.*, 90:056804, 2003. doi: 10.1103/PhysRevLett.90.056804.

[7] Roland Wiesendanger. Spin mapping at the nanoscale and atomic scale. *Rev. Mod. Phys.*, 81:1495, 2009. doi: 10.1103/RevModPhys.81.1495.

[8] K. Hashimoto, C. Sohrmann, J. Wiebe, T. Inaoka, F. Meier, Y. Hirayama, R. A. Römer, R. Wiesendanger, and M. Morgenstern. Quantum Hall Transition in Real Space: From Localized to Extended States. *Phys. Rev. Lett.*, 101(25):256802, 2008. doi: 10.1103/PhysRevLett.101.256802.

[9] Tsuneya Ando, Alan B. Fowler, and Frank Stern. Electronic properties of two-dimensional systems. *Rev. Mod. Phys.*, 54(2):437, 1982. doi: 10.1103/RevModPhys.54.437.

[10] E. I. Rashba. Properties of semiconductors with an extremum loop. 1. Cyclotron and combinational resonance in a magnetic field perpendicular to the plane of the loop. *Sov. Phys. Solid State*, 2:1109, 1960.

[11] Yu. A. Bychkov and E. I. Rashba. Oscillatory effects and the magnetic susceptibility of carriers in inversion layers. *J. Phys. C*, 17(33):6039, 1984. doi: 10.1088/0022-3719/17/33/015.

[12] C. R. Ast, G. Wittich, P. Wahl, R. Vogelgesang, D. Pacile, M. C. Falub, L. Moreschini, M. Papagno, M. Grioni, and K. Kern. Local detection of spin-orbit splitting by scanning tunneling spectroscopy. *Phys. Rev. B*, 75: 201401(R), 2007. doi: 10.1103/PhysRevB.75.201401.

[13] J. I. Pascual, G. Bihlmayer, Y. M. Koroteev, H. P. Rust, G. Ceballos, M. Hansmann, K. Horn, E. V. Chulkov, S. Blügel, P. M. Echenique, and P. Hofmann. Role of spin in quasiparticle interference. *Phys. Rev. Lett.*, 93: 196802, 2004. doi: 10.1103/PhysRevLett.93.196802.

[14] S. LaShell, B. A.a McDougall, and E. Jensen. Spin splitting of an Au(111) surface state band observed with angle resolved photoelectron spectroscopy. *Phys. Rev. Lett.*, 77:3419, 1996. doi: 10.1103/PhysRevLett.77.3419.

[15] M. Hoesch, M. Muntwiler, V. N. Petrov, M. Hengsberger, L. Patthey, M. Shi, M. Falub, T. Greber, and J. Osterwalder. Spin structure of the Shockley surface state on Au(111). *Phys. Rev. B*, 69(24):241401(R), 2004. doi: 10.1103/PhysRevB.69.241401.

[16] C. R. Ast, J. Henk, A. Ernst, L. Moreschini, M. C. Falub, D. Pacile, P. Bruno, K. Kern, and M. Grioni. Giant spin splitting through surface alloying. *Phys. Rev. Lett.*, 98:186807, 2007. doi: 10.1103/PhysRevLett.98.186807.

[17] Y. S. Dedkov, M. Fonin, U. Rüdiger, and C. Laubschat. Rashba effect in the graphene/Ni(111) system. *Phys. Rev. Lett.*, 100:107602, 2008. doi: 10.1103/PhysRevLett.100.107602.

[18] J. Nitta, T. Akazaki, H. Takayanagi, and T. Enoki. Gate control of spin-orbit interaction in an inverted In(0.53)Ga(0.47)AS/In(0.52)Al(0.48)AS heterostructure. *Phys. Rev. Lett.*, 78:1335, 1997. doi: 10.1103/PhysRevLett.78.1335.

[19] G. Engels, J. Lange, Th. Schäpers, and H. Lüth. Experimental and theoretical approach to spin splitting in modulation-doped $In_xGa_{1-x}As/InP$

quantum wells for B→0. *Phys. Rev. B*, 55(4):1958(R), 1997. doi: 10.1103/PhysRevB.55.R1958.

[20] D. Grundler. Large Rashba splitting in InAs quantum wells due to electron wave function penetration into the barrier layers. *Phys. Rev. Lett.*, 84: 6074, 2000. doi: 10.1103/PhysRevLett.84.6074.

[21] J. B. Miller, D. M. Zumbuhl, C. M. Marcus, Y. B. Lyanda-Geller, D.A. Goldhaber-Gordon, K. Campman, and A. C. Gossard. Gate-Controlled Spin-Orbit Quantum Interference Effects in Lateral Transport. *Phys. Rev. Lett.*, 90:076807, 2003. doi: 10.1103/PhysRevLett.90.076807.

[22] T. Koga, J. Nitta, T. Akazaki, and H. Takayanagi. Rashba spin-orbit coupling probed by the weak antilocalization analysis in InAlAs/InGaAs/InAlAs quantum wells as a function of quantum well asymmetry. *Phys. Rev. Lett.*, 89:046801, 2002. doi: 10.1103/PhysRevLett.89.046801.

[23] J. F. Janak. *g* Factor of the Two-Dimensional Interacting Electron Gas. *Phys. Rev.*, 178(3):1416–1418, 1969. doi: 10.1103/PhysRev.178.1416.

[24] Tsuneya Ando and Yasutada Uemura. Theory of Oscillatory *g* Factor in an MOS Inversion Layer under Strong Magnetic Fields. *J. Phys. Soc. Jpn.*, 37(4):1044–1052, 1974. doi: 10.1143/JPSJ.37.1044.

[25] O. E. Dial, R. C. Ashoori, L. N. Pfeiffer, and K. W. West. High-resolution spectroscopy of two-dimensional electron systems. *Nature*, 448:176, 2007. doi: 10.1038/nature05982.

[26] Young Jae Song, Alexander F. Otte, Young Kuk, Yike Hu, David B. Torrance, Phillip N. First, Walt A. de Heer, Hongki Min, Shaffique Adam, Mark D. Stiles, Allan H. MacDonald, and Joseph A. Stroscio. High-resolution tunnelling spectroscopy of a graphene quartet. *Nature*, 467: 185, 2010. doi: 10.1038/nature09330.

[27] A. L. Efros and B. I. Shklovskii. Coulomb gap and low temperature conductivity of disordered systems. *J. Phys. C*, 8(4):L49, 1975. doi: 10.1088/0022-3719/8/4/003.

[28] Boris. I. Shklovskii and Alex. L. Efros. *Electronic Properties of Doped Semiconductors*. Springer-Verlag, 1984. available from `http://www.tpi.umn.edu/shklovskii/`.

[29] Daniel Haude. *Rastertunnelspektroskopie auf der InAs(110)-Oberfläche: Untersuchungen an drei-, zwei- und nulldimensionalen Elektronsystemen im Magnetfeld*. PhD thesis, Universität Hamburg, 2001.

[30] J. Wiebe, Chr. Meyer, J. Klijn, M. Morgenstern, and R. Wiesendanger. From quantized states to percolation: Scanning tunneling spectroscopy of a strongly disordered two-dimensional electron system. *Phys. Rev. B*, 68(4):041402(R), 2003. doi: 10.1103/PhysRevB.68.041402.

[31] Andre Wachowiak. *Aufbau einer 300 mK-Ultrahochvakuum-Rastertunnelmikroskopie-Anlage mit 14 Tesla Magnet und spinpolarisierte Rastertunnelspektroskopie an ferromagnetischen Fe-Inseln*. PhD thesis, Universität Hamburg, 2003.

[32] J. Tersoff and D. R. Hamann. Theory and Application for the Scanning Tunneling Microscope. *Phys. Rev. Lett.*, 50(25):1998–2001, 1983. doi: 10.1103/PhysRevLett.50.1998.

[33] J. Tersoff and D. R. Hamann. Theory of the scanning tunneling microscope. *Phys. Rev. B*, 31(2):805–813, 1985. doi: 10.1103/PhysRevB.31.805.

[34] J. Bardeen. Tunnelling from a Many-Particle Point of View. *Phys. Rev. Lett.*, 6(2):57–59, 1961. doi: 10.1103/PhysRevLett.6.57.

[35] M. Morgenstern, D. Haude, V. Gudmundsson, Chr. Wittneven, R. Dombrowski, Chr. Steinebach, and R. Wiesendanger. Low temperature scanning tunneling spectroscopy on InAs(110). *J. Electr. Spectr. and Rel. Phen.*, 109(1-2):127 – 145, 2000. ISSN 0368-2048. doi: 10.1016/S0368-2048(00)00112-2.

[36] C. Julian Chen. Origin of atomic resolution on metal surfaces in scanning tunneling microscopy. *Phys. Rev. Lett.*, 65(4):448–451, 1990. doi: 10.1103/PhysRevLett.65.448.

[37] C. Julian Chen. Theory of scanning tunneling spectroscopy. *J. Vac. Sci. Technol. A*, 6(2):319–322, 1988. doi: 10.1116/1.575444.

[38] C. Julian Chen. Tunneling matrix elements in three-dimensional space: The derivative rule and the sum rule. *Phys. Rev. B*, 42(14):8841–8857, 1990. doi: 10.1103/PhysRevB.42.8841.

[39] M. Kugler, Ch. Renner, Ø . Fischer, V. Mikheev, and G. Batey. A [sup 3]He refrigerated scanning tunneling microscope in high magnetic fields and ultrahigh vacuum. *Rev. Sci. Instr.*, 71(3):1475, 2000. doi: 10.1063/1.1150483.

[40] Keisuke Sagisaka, Masayo Kitahara, Daisuke Fujita, Giyuu Kido, and Nobuyuki Koguchi. Scanning tunnelling microscopy in extreme fields: very low temperature, high magnetic field, and extreme high vacuum. *Nanotechnology*, 15(6):S371, 2004. doi: 10.1088/0957-4484/15/6/010.

[41] J. Wiebe, A. Wachowiak, F. Meier, D. Haude, T. Foster, M. Morgenstern, and R. Wiesendanger. A 300 mK ultra-high vacuum scanning tunneling microscope for spin-resolved spectroscopy at high energy resolution. *Rev. Sci. Instrum.*, 75:4871, 2004. doi: 10.1063/1.1794431.

[42] A. J. Heinrich, C. P. Lutz, J. A. Gupta, and D. M. Eigler. Molecule Cascades. *Science*, 298(5597):1381, 2002. doi: 10.1126/science.1076768.

[43] Lei Zhang and Wulf Wulfhekel. A sub-Kelvin scanning tunneling microscope with high energy resolution and high stability. In *DPG Frühjahrstagung der Sektion Kondensierte Materie*, Regensburg, Germany, 2010. (O 34.3).

[44] H. Kambara, T. Matsui, Y. Niimi, and Hiroshi Fukuyama. Construction of a versatile ultralow temperature scanning tunneling microscope. *Rev. Sci. Instr.*, 78(7):073703, 2007. doi: 10.1063/1.2751095.

[45] Young Jae Song, Alexander F. Otte, Vladimir Shvarts, Zuyu Zhao, Young Kuk, Steven R. Blankenship, Alan Band, Frank M. Hess, and Joseph A. Stroscio. A 10 mK scanning probe microscopy facility. *Rev. Sci. Instr.*, 81 (12):121101, 2010. doi: 10.1063/1.3520482.

[46] Henri Hansen, Alex Redinger, Sebastian Messlinger, Georgiana Stoian, Joachim Krug, and Thomas Michely. Rapid Coarsening of Ion Beam Ripple Patterns by Defect Annihilation. *Phys. Rev. Lett.*, 102(14):146103, 2009. doi: 10.1103/PhysRevLett.102.146103.

[47] A. Redinger, Y. Rosandi, H. M. Urbassek, and T. Michely. Grazing incidence ion erosion in the presence of adsorbates. *New J. Phys.*, 11(6):063011, 2009. doi: 10.1088/1367-2630/11/6/063011.

[48] Jan Raphael Bindel. Aufbau eines kombinierten Rasterkraft-/Rastertunnelmikroskops für Messungen unter Transportbedingungen. Diplomarbeit, RWTH Aachen University, 2009.

[49] Torge Mashoff. *Design of a low-temperature scanning tunnelling microscope system used to examine graphene nanomembranes*. PhD thesis, RWTH Aachen University, 2010.

[50] S. H. Pan, E. W. Hudson, and J. C. Davis. ^{3}He refrigerator based very low temperature scanning tunneling microscope. *Review of Scientific Instruments*, 70(2):1459–1463, 1999. doi: 10.1063/1.1149605.

[51] Viktor Geringer. Aufbau und Charakterisierung eines Rastertunnelmikroskops mit Verschiebetisch für den Einsatz im Ultrahochvakuum, bei tiefen Temperaturen und im Magnetfeld. Diplomarbeit, RWTH Aachen University, 2006.

[52] O. Pietzsch, A. Kubetzka, D. Haude, M. Bode, and R. Wiesendanger. A low-temperature ultrahigh vacuum scanning tunneling microscope with a split-coil magnet and a rotary motion stepper motor for high spatial resolution studies of surface magnetism. *Review of Scientific Instruments*, 71(2):424–430, 2000. doi: 10.1063/1.1150218.

[53] Torge Mashoff. Aufbau eines UHV-Rastertunnelmikroskops mit X-Y-Verschiebetisch für den Einsatz bei tiefen Temperaturen und im Magnetfeld. Diplomarbeit, University of Hamburg, 2004.

[54] V. Geringer, M. Liebmann, T. Echtermeyer, S. Runte, M. Schmidt, R. Rückamp, M. C. Lemme, and M. Morgenstern. Intrinsic and extrinsic corrugation of monolayer graphene deposited on SiO_2. *Phys. Rev. Lett.*, 102(7): 076102, 2009. doi: 10.1103/PhysRevLett.102.076102.

[55] M. Morgenstern, J. Klijn, Chr. Meyer, M. Getzlaff, R. Adelung, R. A. Römer, K. Rossnagel, L. Kipp, M. Skibowski, and R. Wiesendanger. Direct Comparison between Potential Landscape and Local Density of States in a Disordered Two-Dimensional Electron System. *Phys. Rev. Lett.*, 89(13): 136806, 2002. doi: 10.1103/PhysRevLett.89.136806.

[56] Maria Grazia Betti, V. Corradini, G. Bertoni, P. Casarini, Carlo Mariani, and A. Abramo. Density of states of a two-dimensional electron gas at semiconductor surfaces. *Phys. Rev. B*, 63(15):155315, 2001. doi: 10.1103/PhysRevB.63.155315.

[57] Frank Stern. Self-Consistent Results for *n*-Type Si Inversion Layers. *Phys. Rev. B*, 5(12):4891, 1972. doi: 10.1103/PhysRevB.5.4891.

[58] I. Vurgaftman, J. R. Meyer, and L. R. Ram-Mohan. Band parameters for III-V compound semiconductors and their alloys. *J. Appl. Phys.*, 89:5815, 2001. doi: 10.1063/1.1368156.

[59] O. Madelung, U. Rössler, and M. Schulz. *Landolt-Börnstein - Group III Condensed Matter*. Springer Verlag, 2002. doi: 10.1007/b80447.

[60] Evan O. Kane. Band Structure of Indium Antimonide. *J. Phys. Chem. Solids*, 1(4):249, 1957. doi: 10.1016/0022-3697(57)90013-6.

[61] W. Zawadzki. Electron transport phenomena in small-gap semiconductors. *Adv. Phys.*, 23(3):435, 1974. doi: 10.1080/00018737400101371.

[62] R. Winkler and U. Rössler. General approach to the envelope-function approximation based on a quadrature method. *Phys. Rev. B*, 48(12):8918, 1993. doi: 10.1103/PhysRevB.48.8918.

[63] U. Merkt and S. Oelting. Simple description of nonparabolic two-dimensional subbands. *Phys. Rev. B*, 35(5):2460, 1987. doi: 10.1103/PhysRevB.35.2460.

[64] L. M. Kanskaya, S. I. Kokhanovskii, K. P. Seysyan, and Al. L. Efros. Direct Determination of Indium Antimonide Energy Band Parameters from Diamagnetic Exciton Spectra. *Phys. Status Solidi B*, 118(1):447, 1983. doi: 10.1002/pssb.2221180153.

[65] R. E. Prange and S. M. Girvin. *Quantum Hall Effect*. Springer, Berlin, 1986.

[66] T. Ando. Electron Localization in a Two-Dimensional System in Strong Magnetic Fields. II. Long-Range Scatterers and Response Functions. *J. Phys. Soc. Jpn.*, 53:3101, 1984. doi: 10.1143/JPSJ.53.3101.

[67] E. A. de Andrada e Silva, G. C. La Rocca, and F. Bassani. Spin-split subbands and magneto-oscillations in III-V asymmetric heterostructures. *Phys. Rev. B*, 50(12):8523, 1994. doi: 10.1103/PhysRevB.50.8523.

[68] T. Mashoff, M. Pratzer, and M. Morgenstern. A low-temperature high resolution scanning tunneling microscope with a three-dimensional magnetic vector field operating in ultrahigh vacuum. *Rev. Sci. Instrum.*, 80(5): 053702, 2009. doi: 10.1063/1.3127589.

[69] L. J. Whitman, Joseph A. Stroscio, R. A. Dragoset, and R. J. Celotta. A scanning tunneling microscopy study of clean and Cs-covered InSb(110). *J. Vac. Sci. Technol. B*, 9(2):770, 1991. doi: 10.1116/1.585508.

[70] R. Dombrowski, Chr. Steinebach, C. Wittneven, M. Morgenstern, and R. Wiesendanger. Tip-induced band bending by scanning tunneling spectroscopy of the states of the tip-induced quantum dot on InAs(110). *Phys. Rev. B*, 59:8043, 1999. doi: 10.1103/PhysRevB.59.8043.

[71] C. Metzner, M. Hofmann, and G. H. Döhler. Intersubband transitions of a quasi-two-dimensional electron gas in the strong disorder regime. *Phys. Rev. B*, 58(11):7188, 1998. doi: 10.1103/PhysRevB.58.7188.

[72] K. Kanisawa, M. J. Butcher, H. Yamaguchi, and Y. Hirayama. Imaging of friedel oscillation patterns of two-dimensionally accumulated electrons at epitaxially grown InAs(111)A surfaces. *Phys. Rev. Lett.*, 86:3384, 2001. doi: 10.1103/PhysRevLett.86.3384.

[73] E. Abrahams, P. W. Anderson, D. C. Licciardello, and T. V. Ramakrishnan. Scaling Theory of Localization: Absence of Quantum Diffusion in Two Dimensions. *Phys. Rev. Lett.*, 42(10):673, 1979. doi: 10.1103/PhysRevLett.42.673.

[74] M. Morgenstern, D. Haude, J. Klijn, Chr. Meyer, L. Sacharow, S. Heinze, S. Blügel, and R. Wiesendanger. Comparing the local density of states of three- and two-dimensional electron systems by low-temperature scanning tunneling spectroscopy. *Physica E*, 16(1):121, 2003. doi: 10.1016/S1386-9477(02)00585-4.

[75] Y. Niimi, H. Kambara, and H. Fukuyama. Localized Distributions of Quasi-Two-Dimensional Electronic States near Defects Artificially Created at Graphite Surfaces in Magnetic Fields. *Phys. Rev. Lett.*, 102:026803, 2009. doi: 10.1103/PhysRevLett.102.026803.

[76] David L. Miller, Kevin D. Kubista, Gregory M. Rutter, Ming Ruan, Walt A. de Heer, Markus Kindermann, Phillip N. First, and Joseph A. Stroscio. Real-space mapping of magnetically quantized graphene states. *Nat. Phys.*, 6:811, 2010. doi: 10.1038/nphys1736.

[77] Adina Luican, Guohong Li, and Eva Y. Andrei. Quantized Landau level spectrum and its density dependence in graphene. *Phys. Rev. B*, 83(4): 041405(R), 2011. doi: 10.1103/PhysRevB.83.041405.

[78] M. Getzlaff, M. Morgenstern, C. Meyer, R. Brochier, R. L. Johnson, and R. Wiesendanger. Nb-induced two-dimensional electron gas on n-InAs(110): Anomalous coverage dependence. *Phys. Rev. B*, 63:205305, 2001. doi: 10.1103/PhysRevB.63.205305.

[79] Harald Ibach and Hans Lüth. *Festkörperphysik: Einführung in die Grundlagen*. Springer, 2002. ISBN 3540427384.

[80] T. Matsuyama, R. Kürsten, C. Meißner, and U. Merkt. Rashba spin splitting in inversion layers on p-type bulk InAs. *Phys. Rev. B*, 61(23):15588, 2000. doi: 10.1103/PhysRevB.61.15588.

[81] L. Petersen and P. Hedegard. A simple tight-binding model of spin-orbit splitting of sp-derived surface states. *Surf. Sci.*, 459:49, 2000. doi: 10.1016/S0039-6028(00)00441-6.

[82] J. E. D. Walls and E. J. Heller. Spin-orbit coupling induced interference in quantum corrals. *Nano Lett.*, 7:3377, 2007. doi: 10.1021/nl071711z.

[83] M. M. Glazov and E. Ya. Sherman. Nonexponential spin relaxation in magnetic fields in quantum wells with random spin-orbit coupling. *Phys. Rev. B*, 71(24):241312(R), 2005. doi: 10.1103/PhysRevB.71.241312.

[84] M.M. Glazov, E.Ya. Sherman, and V.K. Dugaev. Two-dimensional electron gas with spin-orbit coupling disorder. *Physica E*, 42(9):2157 – 2177, 2010. ISSN 1386-9477. doi: 10.1016/j.physe.2010.04.021.

[85] R. Masutomi, M. Hio, T. Mochizuki, and T. Okamoto. Quantum Hall effect at cleaved InSb surfaces and low-temperature annealing effect. *Appl. Phys. Lett.*, 90:202104, 2007. doi: 10.1063/1.2740579.

[86] Marcus Liebmann. Hopping model calculations for a decoupled two-dimensional electron system in *p*-InSb as measured by scanning tunneling spectroscopy (unpublished). private communication.

[87] R. M. Feenstra and Joseph A. Stroscio. Tunneling spectroscopy of the GaAs(110) surface. *J. Vac. Sci. Technol. B*, 5(4):923, 1987. doi: 10.1116/1.583691.

[88] J. Kröger, H. Jensen, and R. Berndt. Conductance of tip–surface and tip–atom junctions on Au(111) explored by a scanning tunnelling microscope. *New J. Phys.*, 9(5):153, 2007. doi: 10.1088/1367-2630/9/5/153.

[89] A. P. Smith, A. H. MacDonald, and G. Gumbs. Quasiparticle effective mass and enhanced g factor for a two-dimensional electron gas at intermediate magnetic fields. *Phys. Rev. B*, 45(15):8829(R), 1992. doi: 10.1103/PhysRevB.45.8829.

[90] S. Becker, C. Karrasch, T. Mashoff, M. Pratzer, M. Liebmann, V. Meden, and M. Morgenstern. Probing Electron-Electron Interaction in Quantum Hall Systems with Scanning Tunneling Spectroscopy. *Phys. Rev. Lett.*, 106 (15):156805, 2011. doi: 10.1103/PhysRevLett.106.156805.

[91] M. Pollak. Effect of carrier-carrier interactions on some transport properties in disordered semiconductors. *Discuss. Faraday Soc.*, 50:13, 1970. doi: 10.1039/DF9705000013.

[92] F. G. Pikus and A. L. Efros. Coulomb gap in a two-dimensional electron gas with a close metallic electrode. *Phys. Rev. B*, 51(23):16871, 1995. doi: 10.1103/PhysRevB.51.16871.

[93] Andreas Glatz, Valerii M. Vinokur, Joakim Bergli, Martin Kirkengen, and Yuri M. Galperin. The Coulomb gap and low energy statistics for Coulomb glasses. *J. Stat. Mech.: Theory Exp.*, 2008(06):P06006, 2008. doi: 10.1088/1742-5468/2008/06/P06006.

[94] V. Yu. Butko, J. F. DiTusa, and P. W. Adams. Coulomb Gap: How a Metal Film Becomes an Insulator. *Phys. Rev. Lett.*, 84(7):1543–1546, 2000. doi: 10.1103/PhysRevLett.84.1543.

[95] R. C. Ashoori, J. A. Lebens, N. P. Bigelow, and R. H. Silsbee. Energy gaps of the two-dimensional electron gas explored with equilibrium tunneling spectroscopy. *Phys. Rev. B*, 48(7):4616, 1993. doi: 10.1103/PhysRevB.48.4616.

[96] H. B. Chan, P. I. Glicofridis, R. C. Ashoori, and M. R. Melloch. Universal Linear Density of States for Tunneling into the Two-Dimensional Electron Gas in a Magnetic Field. *Phys. Rev. Lett.*, 79(15):2867, 1997. doi: 10.1103/PhysRevLett.79.2867.

[97] E. V. Deviatov, A. A. Shashkin, V. T. Dolgopolov, W. Hansen, and M. Holland. Tunneling measurements of the Coulomb pseudogap in a two-dimensional electron system in a quantizing magnetic field. *Phys. Rev. B*, 61(4):2939, 2000. doi: 10.1103/PhysRevB.61.2939.

[98] J. R. Dixon and J. K. Furdyna. Measurement of the static dielectric constant of the InSb lattice via gyrotropic sphere resonances. *Solid State Commun.*, 35:195, 1980. doi: 10.1016/0038-1098(80)90244-6.

[99] S.-R. Eric Yang and A. H. MacDonald. Coulomb gaps in a strong magnetic field. *Phys. Rev. Lett.*, 70(26):4110–4113, 1993. doi: 10.1103/PhysRevLett.70.4110.

[100] T. Champel and S. Florens. Local density of states in disordered two-dimensional electron gases at high magnetic field. *Phys. Rev. B*, 80(16): 161311(R), 2009. doi: 10.1103/PhysRevB.80.161311.

[101] James R. Chelikowsky and Marvin L. Cohen. Erratum: Nonlocal pseudopotential calculations for the electronic structure of eleven diamond and zinc-blende semiconductors. *Phys. Rev. B*, 30(8):4828, 1984. doi: 10.1103/PhysRevB.30.4828.

Publications

1. S. Becker, C. Karrasch, T. Mashoff, M. Pratzer, M. Liebmann, V. Meden, and M. Morgenstern. Probing Electron-Electron Interaction in Quantum Hall Systems with Scanning Tunneling Spectroscopy. *Phys. Rev. Lett.*, 106 (15):156805, 2011. doi: 10.1103/PhysRevLett.106.156805.

2. S. Becker, M. Liebmann, T. Mashoff, M. Pratzer, and M. Morgenstern. Scanning tunneling spectroscopy of a dilute two-dimensional electron system exhibiting Rashba spin splitting. *Phys. Rev. B*, 81(15):155308, 2010. doi: 10.1103/PhysRevB.81.155308.

Presentations

1. S. Becker, M. Liebmann, T. Mashoff, M. Pratzer, and M. Morgenstern. Scanning tunneling spectroscopy of a dilute two-dimensional electron system exhibiting Rashba spin splitting. In *JARA-FIT nanoelectronics days*, Aachen, Germany, 2010. (Poster)

2. S. Becker, M. Liebmann, and M. Morgenstern. Scanning tunneling spectroscopy of a dilute two-dimensional electron system exhibiting Rashba spin splitting. In *DPG Frühjahrstagung der Sektion Kondensierte Materie*, Regensburg, Germany, 2010. (Talk)

3. S. Becker, M. Liebmann, and M. Morgenstern. Rashba spin splitting observed on *p*-type InSb(110) by scanning tunneling spectroscopy. In *449th WE-Heraeus Seminar*, Bad Honnef, Germany, 2010. (Poster Award)

4. S. Becker, M. Liebmann, and M. Morgenstern. A UHV-STM system for measurements at 300 mK and 14 T. In *72. Jahrestagung der DPG und DPG Frühjahrstagung des Arbeitskreises Festkörperphysik*, Berlin, Germany, 2008. (Poster)

Acknowledgments

All parts of this thesis relied on the support of many people, be it the introduction into the topic of LT-UHV-STMs, help in developing the design criteria of the components, production and assembly, infrastructure, measurement assistance, mathematical support by theoreticians, and the many many discussions. But first of all I have to thank *Prof. Dr. Markus Morgenstern* for offering me these PhD topics and his great leadership throughout the years, which was friendly, guiding, and educational at all times. Your great enthusiasm for your research is addictive and the research group as well as the supporting staff you have gathered create an enjoyable and productive working environment that will be hard to find again.

Second in command, office mate, and my direct supervisor *Dr. Marcus Liebmann* helped me a great deal with his experience in LT-UHV scanning probe systems and is surely in part responsible for the final STM and chamber design. Some of his greatest qualities are that he thinks before he talks, and if he does not know something, he will get back to you.

For the component designs I could rely on the experience and prior designs of other colleagues, showing me the advantages of some mechanisms and hinting the flaws of other aspects. This helped me not to repeat the mistakes of others, but to make only my own. In this respect I have to thank *Dr. Torge Mashoff* for the head start of the design and production of his LT-UHV-STM system, with which I had the opportunity to perform the measurements presented in this work. The same goes for *Dr. Marco Pratzer*, whose practical knowledge of UHV instruments was a most valuable asset. For the experimential expertise about STM measurements of Cs on InSb I want to thank *Dr. Katsushi Hashimoto* and I wish him and his family all the best during the current crisis in Japan.

Many thanks go out to the mechanical workshop under the supervision of *Peter Kordt* and *Wolfgang Retetzki*, which fabricated almost all parts of the non-commercial components of the system with high precision and quality. Special thanks goes to *Frank Neubauer*, who fabricated most of the finer parts and did also the CNC cutting for the UHV chambers, and to *Frank Salz*, who welded, I believe all on his own, all chambers and the whole support frame. But, according to the weight of the folder with technical drawings on my desk, I doubt that anyone of the workshop members has not contributed to my system.

I have to thank *Dr. Viktor Geringer* for the assembly of the STM and his feedback on some of my prototype designs. I thank the PhD students *Mike Pezzotta* and *Raphael Bindel*, who are working on finishing the system and especially the cryostat. I trust that their final helium-3 stage design will perform flawlessly and I am very keen to see their progress.

For the interesting discussions about random Rashba fields I want to thank *Dr. Eugene Sherman*. For fruitful discussions, their calculations regarding electron–electron interaction in my measurements, and the cooperation in the corresponding publication, I want to thank *Prof. Dr. Volker Meden* and *Dr. Christoph Karrasch* for their efforts. I thank *Prof. Dr. Thomas Schäpers* for agreeing to co-evaluate my thesis.

Many other people contributed with larger an smaller assists during my PhD work, and I am grateful for the very nice working environment at the II. Physikalischen Insitut. Responsible for this are the administrative staff *Regina Weinkauf*, *Sixta Vurgun*, *Nina Grydzhuk*, and *Julia Schütte*, *Jörg Schirra* and *Sascha Mohr* in gas liquefaction, and the remaining technical staff. In place of all the remaining PhD and diploma students, who were always available for assistance in the laboratory as well as for various discussions elsewhere, I want to thank *Dinesh Subramaniam* for being a great colleague.

I want to thank my wife *Marita Hennes* and my parents-in-law *Hildegard and Dr. Clemens Hennes* for their constant support. I much appreciate the free office space provided by *Carola and Markus Maier*, allowing me to write this text in solitude. Finally I thank my parents *Marianne and Theodor Becker*, who always supported me in any way they could.